

**Structural Analysis and Electrical Properties of
Synthetic Murataite Series**

Ryosuke Maki
Doctoral program in Materials Science

**Submitted to the Graduate School of
Pure and Applied Sciences
in Partial Fulfillment of the Requirements
for the Degree of Doctor of Philosophy in
Engineering**

**at the
University of Tsukuba**

Preface

Structural Analysis and Electrical Properties of Synthetic Murataite Series

Ryosuke Maki

2017/02/027

The studies presented here were carried out under the guidance of Associate Professor Yoshikazu Suzuki in the Development of Materials Science at the Graduate School of Pure and Applied Sciences, University of Tsukuba.

In this work, I focused on murataite ceramics with a 3D polysomatic structure constructed from fluorite-type superstructure. The crystal structures and electrical properties of murataite series were investigated.

Various compounds with fluorite-related structures, such as cubic zirconia, are considered to be potential important applications, *e.g.* oxygen gas sensors and catalysts. The material system of fluorite-type oxide exhibits for a wide range of constituent elements and have been investigated as promising functional materials such as electrolyte of solid oxide fuel cells (SOFCs). Several ceramics with fluorite-type superstructure also have been synthesized, and the relationship between the crystal structure and their physical properties are recently focused on for electrolyte of intermediate temperature SOFCs; *e.g.* $Y_{10-x}La_xW_2O_{21}$ is an excellent oxygen ionic conductor at intermediate temperatures and exhibits good conductivity with enhancement of symmetry of superlattice ($3\times 2\times 2 \rightarrow 2\times 2\times 2$). In addition to this, these fluorite-related structures have been investigated for SYNROC material. Actinide elements, such as Pu and U, which are in high-level waste (HLW) from nuclear reactors, can occupy specific sites in the crystal structure of SYNROC material as major constituent elements, which results in the immobilization of radioactive wastes under thermally and chemically stable state for hundreds of millions of years. Also, several fluorite-related structures with superlattice are well-known, *e.g.* pyrochlore (Py) and zirconolite with $2\times 2\times 2$ fluorite-type superstructure. The pyrochlore ceramics can be considered for the use of an electrolyte for SOFCs, and its electrical conductivity is higher than conventional cubic zirconia at intermediate temperature. Therefore, I focused on murataite ceramics recognized as an anion-deficient $3\times 3\times 3$ fluorite-type superstructure (M3) with ordered arrangement of cations.

In addition, other murataite series, $5\times 5\times 5$, $7\times 7\times 7$ and $8\times 8\times 8$ fluorite-type superstructures referred to as M5, M7 and M8, also have been confirmed by transmission electron microscopy (TEM). The detailed crystal structures of these M3, M5 and M8 were recently presented by using X-ray diffraction data from synthetic murataite series synthesized by melting method. These crystal structures are considered to be polysomatic series built up from the isometric combination of M3 and Py; results in M3: Py = 1:1 (M5), 1:2 (M7), 2:1 (M8), respectively. This is a very rare case of a 3D polysomatic structure constructed from two parent frameworks. An investigation for the correlation of electrical properties with the crystal structure is very important since the electrical characteristics of ceramics material markedly change depending on an intrinsic complicated crystal structure (constituent elements, defects, etc.). The main research of synthetic murataite at present, however, is directed to the SYNROC as mentioned above, and natural murataite mineral consists of actinide as a constituent elements. Even in synthetic murataite which has been reported in recent years, actinide and rare earth elements are generally used to form the murataite sample.

In this study, I have tried to synthesize the murataite series with conventional solid state reaction method

without actinide nor rare earth elements, but many unclear points still remain regarding the crystal structure of these murataite series. The synthetic murataites can contain transition and rare earth elements, and cation substitution typically occur at each cation site. This complexity makes the structural analyses of murataite series quite challenging. In M8 in particular, coupled with the enormous size and complexity of its crystal structure, there are still many undetermined points at present. Furthermore, no evaluation has been done on physical, mechanical and chemical properties of murataite series known to date. Therefore, I have tried to elucidate the crystal structure of murataite ceramics, by preparing M3 which is particularly important among these murataite series and M8 which has the most complicated crystal structure in murataite polysomatic series. In addition to this, electrical properties of the murataite ceramics were characterized based on their unique crystal structure with fluorite-type superlattice. This is the first finding of the dependence of electrical conductivity on temperature and oxygen partial pressure for synthetic murataite series.

Table of contents

Chapter 1: Introduction	2
1.1 Introduction of murataite series	2
1.2 Fluorite-related structure	4
1.2.1 Structural features	4
1.2.2 Applications of fluorite-type ceramics	5
1.3 History and features of murataite	7
1.3.1 Natural murataite	7
1.3.2 Synthetic murataite (M3, M5, M7, M8)	8
1.4 Chemical formula of synthetic murataite	9
1.5 Crystal structures of murataite polysomatic series	10
1.6 Structural size and complexity	15
1.7 Objectives	16
References	17
Chapter 2: Synthesis and Characterization of the 3×3×3 and 8×8×8 Fluorite-type Superstructure with Solid-State Reaction	24
2.1 Introduction	24
2.2 Outline of synthesis technique	25
2.2.1 Method for powder preparation (Planetary ball-milling)	25
2.2.2 Sample compaction (Cold isostatic pressing)	25
2.2.3 Method for sintered sample fabrication	25
2.3 Experimental procedure	26
2.3.1 Sample preparation	26
2.3.2 Sample characterizations	26
2.4 Results	28
2.4.1 Dependence of the phase formation on synthesis conditions	28
2.4.2 Preparation of high purity murataite series	32
2.4.3 Microstructural observation	35
2.4.4 Element mapping for M3-type murataite	37
2.4.5 PXRD characterization of the large-volume unit cell of the M8 murataite polytype	39
2.4.6 Confirmation for space group using synchrotron X-ray diffraction	48
2.5 Discussion	50
2.5.1 Comparison between microstructure of murataite series synthesized by solid-state and melting	50
2.5.2 Important approach for quick/speedy monitoring of families of very complex polytypes	51
2.5.3 The deference of SG from that already proposed in previous works	51
2.6 Conclusions	51
References	53
Chapter 3: Synthesis and Characterization of a Simpler Mn-free, Fe-rich M3-type Murataite	56

3.1 Introduction	56
3.2 Experimental procedure.....	57
3.2.1 Sample preparation	57
3.2.2 Sample characterizations	59
3.3 Results	59
3.3.1 Phase identification of the M3-type murataite.....	59
3.3.2 Microstructural observation of Mn-free and regular M3	66
3.4 Discussion	67
3.4.1 Comparison of XRD patterns between the natural and synthetic murataite.....	67
3.4.2 Comparison of chemical compositions between the conventional and Mn-free murataite	67
3.5 Conclusions.....	67
References	68
Chapter 4: Structural Analysis and Visual Characterization for M3-type Murataite.....	72
4.1 Introduction.....	72
4.2 Experimental procedure.....	73
4.2.1 Sample preparation	73
4.2.2 Microstructural observation	73
4.2.3 Chemical analysis	73
4.2.4 Sample characterizations	74
4.3 Results and discussion.....	74
4.3.1 Cation distribution in Mn-free M3 observed by HAADF-STEM and EELS analysis	74
4.3.2 Dependence of the microstructure of murataite series on synthesis conditions	75
4.3.3 Site preference of Zr ion in the M3-type murataite	77
4.3.4 Chemical analysis for transition elements, Fe and Mn ions	79
4.4 Conclusions.....	80
References	81
Chapter 5: Electrical Properties of Murataite Modules with Complex and Large-Volume Fluorite-type Superstructures.....	84
5.1 Introduction.....	84
5.2 Experimental procedure.....	85
5.2.1 Sample preparation	85
5.2.2 Sample characterizations	86
5.2.3 Methods for measuring the electrical conductivity.....	86
5.2.4. Measurement of electromotive force for evaluation of ionic transport number.....	87
5.3 Results	87
5.3.1 Phase identification by XRD and TEM-SAED	87
5.3.2 Electrical conductivities of M3- and M8-type murataite	90
5.3.3 Dependence of electrical conductivity on oxygen partial pressure	92

5.3.4 Measurement of electromotive force	93
5.4 Discussion	93
5.4.1 Potential application of murataite as functional ceramics	93
5.5 Conclusions	94
References	95
Chapter 6: Summary and Conclusions	98
Appendix 1: Complete Synchrotron X-ray Diffraction Pattern of the M8 Murataite Polytype	102
Achievements	110
Acknowledgements	115

Chapter 1

Introduction

Chapter 1: Introduction

1.1 Introduction of murataite series

Natural murataite is a very rare mixed oxide mineral found in debris from a small pegmatite in the St. Peters Dome area in 1974 [1,2] being somewhat like pyrochlore but having a three-fold fluorite-related sub-cell instead of pyrochlore's two-fold one [3] (Fig. 1-1). The closely related synthetic versions, however, containing very different elements, have a similar anion-deficient three-fold fluorite-type FCC superstructure, denoted M3; they are very promising as future crystalline radioactive waste host materials [4-6]. The synthetic murataite M3, e.g. as formally $^{[8]}Ca1_6^{[8]}Ca2_4^{[6]}Ti1_{12}^{[5]}Ti2_4^{[4]}AlO_{42}$, where $Ca = Ca, Mn, REE$; $Ti = Ti, Zr, Al$; $Al = Al, Fe$, is presently believed to contain five symmetrically independent cation positions, while natural murataite contains only four cation positions (space group: $F\bar{4}3m$) [7]. $Ca2$ is the additional site coordinated by eight oxygen ions, and cation substitution can typically occur at each cation site. This complexity makes the structural analyses of murataites quite challenging.

Several other synthetic varieties of the murataite-pyrochlore polysomatic series with $5 \times 5 \times 5$, M5, $7 \times 7 \times 7$, M7 and $8 \times 8 \times 8$, M8 fluorite-type superstructures, have been discovered by very careful electron diffraction [8-12]. These modular nature of the polysomatic varieties were mainly achieved by melt methods which produces crystals with complicating zoning of mixed types. Laverov *et al.* found that five volume percent of the total synthetic murataite accumulate about 40% of the total amount of uranium present in the sample [13]. This finding led to the follow-up detailed study for chemistry and properties of these materials. Details of crystal structure and their fascinating features are described following sections.

Modular material

Some families of inorganic compounds form an array of more or less closely related, very complex structures with a number of independent atomic positions and unit cells of large dimensions. These structures can be built up into a number of fragments (modules) that have relatively simple substructures but are joined into a more complex whole. Some modules occur in many members of these families, often in variably expanded/contracted forms as well as combined with elements of other kinds. From the point of view of the bond strength distribution, these modules/elements may form independent units, weakly bonded on the outside, or they are only geometrical (configurational) entities that otherwise merge into the bonding pattern of the structure [14]. This structural approach to oxide structure led to a concept of polysomatic series devised for silicate examples by Thompson in 1970 [15]. The coordination polyhedral on the surface and in the interfaces of the blocks (in Thompson's case, layers) are treated as one type of (layer) module whereas the incrementally accretes polyhedral layers in the layer (block) interior as another type of layer modules. Thus, all accreting homologues are treated as ordered intergrowths of two structure types which occur in different proportions in different homologues [16-17].

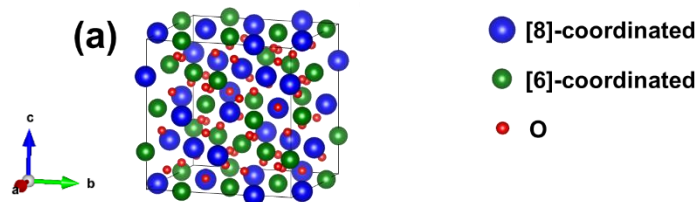
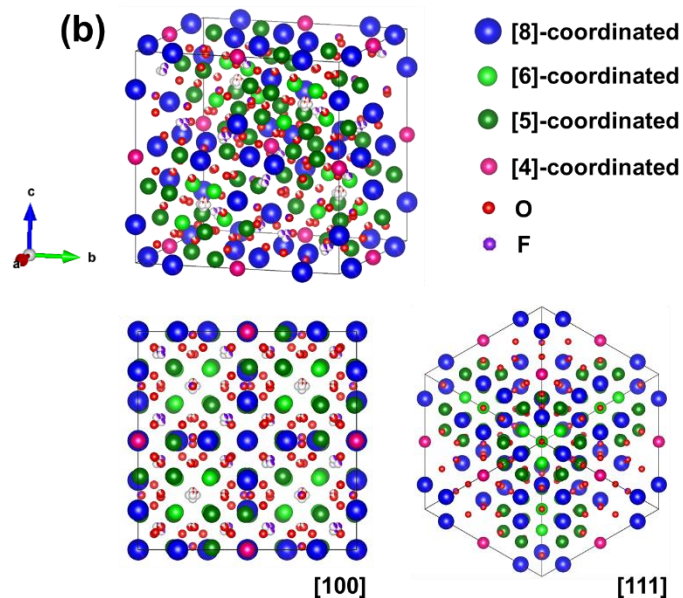
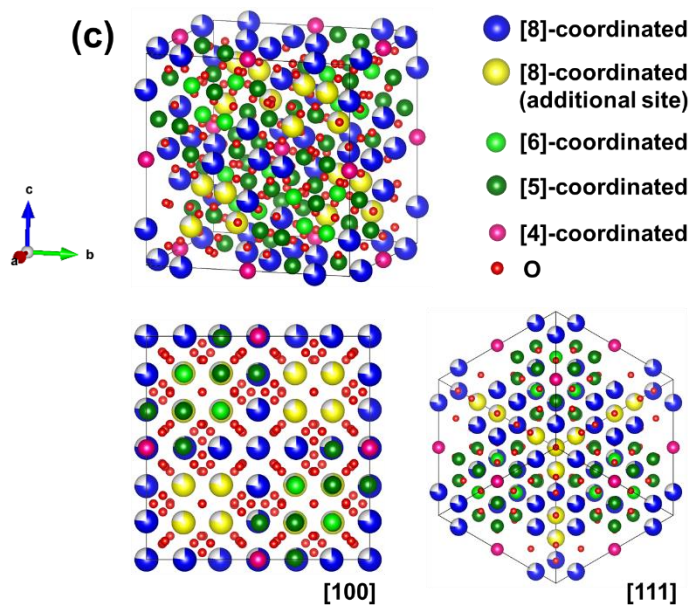
PyrochloreNatural murataiteSynthetic murataite

Fig. 1-1 Crystal structure of fluorite-type superstructures: (a) pyrochlore [3], (b) natural murataite mineral [2] and (c) synthetic murataite, M3 [7]. Synthetic M3 contains additional site, $^{18}\text{Ca}2$, which disappears in natural murataite (these figures are illustrated by VESTA [18]).

1.2 Fluorite-related structure

1.2.1 Structural features

In the fluorite-type structure, the cation (metal ion) constitutes a face-centered cubic in the unit cell, and the oxide ion occupies a tetracoordinated site (Fig. 1-2 (a)) [19]. Substituting a cation with lower valence than Zr^{4+} leads to the anion vacancy in the crystal structure, which results in an oxygen ion conductivity through a relatively loosely packed (anion deficient) crystal structure. ZrO_2 ceramics is the most famous material as fluorite-type ceramics, but monoclinic crystal is stable at room temperature. By increasing the temperature, the crystal structure shows a phase transition with Monoclinic \rightarrow Tetragonal \rightarrow Cubic. A dopant, such as Y_2O_3 , CaO and MgO , can stabilize the cubic structure of ZrO_2 at room temperature.

CeO_2 , HfO_2 and ThO_2 are well-known as fluorite-type oxides exhibiting oxygen ion conductivity. In addition to these, several oxide materials with a fluorite-type superstructure have also been reported recently. $A_2B_2O_7$ (A : REE, $B = Zr, Ti$) with a pyrochlore structure has much attention as a solid electrolyte of an intermediate temperature solid oxide fuel cells (IT-SOFCs). In $Y_2Zr_2O_7$ which is a typical composition of pyrochlore ceramics, its crystal structure can be regarded as a fluorite-type structure in which oxygen defects are orderly arranged, and considered as $2 \times 2 \times 2$ fluorite-type superstructure. (Fig. 1-2 (b)) [3]. As for $Gd_2(Zr_xTi_{1-x})_2O_7$, its anion deficient crystal structure and mixed conductivity can be controlled by adjusting the chemical composition [20,21]. Various fluorite-related structures, such as zirconolite ($CaZrTi_2O_7$) and $M_{10}W_2O_{21}$ ($M = Er, Y$), have been reported, which indicate C-centered monoclinic $2 \times 2 \times 2$ fluorite-type superstructure and orthorhombic $3 \times 2 \times 2$ fluorite-type superstructure, respectively (Fig. 1-2 (c, d)) [22,23]. Zirconolite has attracted much interest, as it has been proposed as a constituent phase of an artificial rock (SYNROC) which may immobilize the actinide elements occurring in high-level nuclear reactor wastes [22]. $M_{10}W_2O_{21}$ ($M = Er, Y$) has been eagerly investigated for the solid electrolyte of IT-SOFCs [23].

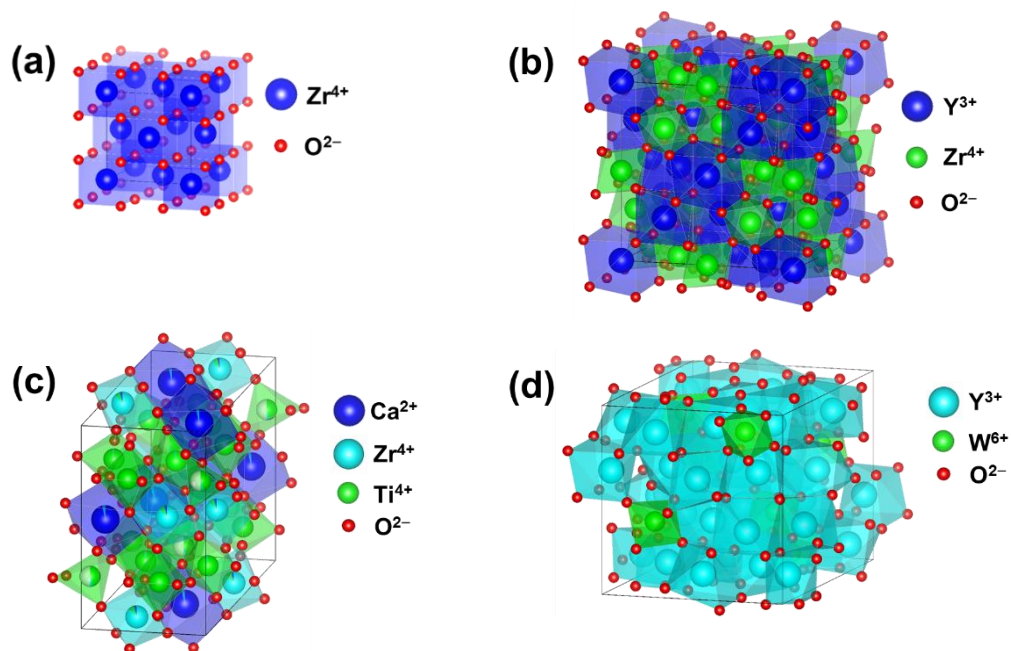


Fig. 1-2 Crystal structures of fluorite-related structure: (a) cubic zirconia (ZrO_2) [19], (b) pyrochlore ($Y_2Zr_2O_7$) [3], (c) Zirconolite ($CaZrTi_2O_7$) [22], and (d) $Y_{10}W_2O_{21}$ [23]. The 8-, 7- and 6-coordinated polyhedrons are colored to blue, light blue and light green, respectively.

1.2.2 Applications of fluorite-type ceramics

Electrolyte for SOFCs

SOFCs can produce an efficient and clean energy conversion with superior tolerance to impurities in the fuel, which allows less costly and more widely available for their operation at high temperature compared with polymer electrolyte membrane fuel cells (PEMFCs) [24-27]. Due to the higher operating temperature, however, undesired reactions and thermal stresses during thermal cycling occur. Therefore there are materials challenges in all fuel cell components such as materials for use as the solid electrolyte. A synthesis of new ceramics with good ionic conductivity ($>0.1 \text{ Scm}^{-1}$ [28]) and little or no electronic conductivity to minimize leakage currents is the key parameters for the solid electrolyte. Thus, various approaches for controlling the concentration and mobility of ionic and electronic charge carriers through structural properties of the electrolyte material have been recently investigated [29]. A major approaches for the development of SOFCs is reduction of the operation temperature to 500-800°C for IT-SOFCs [30].

ZrO₂, CeO₂, HfO₂ and ThO₂ are well-known as fluorite-type oxides exhibiting good oxygen ionic conductivity, especially yttria-stabilized zirconia (YSZ): the most common solid electrolyte material used in SOFCs [30]. Yttria is used for stabilizing the cubic fluorite phase, as well as increasing the concentration of oxygen vacancies. YSZ indicates good chemical and physical stability in a wide operating range of temperature and oxygen partial pressure, P_{O_2} . In addition to this, scandia-stabilized zirconia (ScSZ) has higher conductivity than that of YSZ, which is attributed to the smaller mismatch in size between Zr⁴⁺ and Sc³⁺ compared with that between Zr⁴⁺ and Y³⁺ [31,32].

In addition to above, the materials with fluorite-type superstructure have been investigated for electrolyte of SOFCs [33]. A Pyrochlore ceramics have similar crystal structure with the cubic fluorite structure, in which oxygen defects are orderly arranged; *i.e.* essentially the same crystal structure with one oxygen missing per unit-cell. Yamamura *et al.* reported that Ln₂Zr₂O₇ (Ln = Yb, Y, Gd, Eu, Sm, Nd, La) system changes from fluorite-type to pyrochlore phases due to the ionic radius ratios, $r(\text{Ln}^{3+})/r(\text{Zr}^{4+})$. The oxygen ion conductivity shows maximum value at the vicinity of the phase boundary between the fluorite and pyrochlore phases [34].

M₁₀W₂O₂₁ (M = Er, Y, La) ceramics also have much attention for the use as electrolyte of IT-SOFCs. This system has fluorite-type superstructure: Ln₁₀(Mo/W)₂O₂₁ is believed as a pyrochlore-related structure with cubic, except for Er and Y [23] which present an orthorhombic fluorite superstructure. Y_{10-x}La_xW₂O₂₁ system indicates the distortion from orthorhombic structure (3×2×2 fluorite-type superstructure) of Y₁₀W₂O₂₁ towards a face-centered pseudo-cubic structure (2×2×2 fluorite-type superstructure) of Y₅La₅W₂O₂₁ with increase in the electrical conductivity. The ionic conductivity of YLa₉W₂O₂₁ is comparable to the un-optimized yttria stabilized zirconia at 1000°C [35]. Recently, the crystal structure of La₁₀W₂O₂₁ was reformulated (La_{5.667}W_{0.333})LaWO₁₄□₂ with 2×2×2 anion-deficient fluorite-related superstructure by several powerful techniques [36]. Its transmission electron microscopy selected area electron diffraction (TEM-SAED) patterns clearly perform the strong and weak reflections corresponding to fluorite sub-cell and superlattice in a cubic lattice with cell parameter $a \approx 11.2 \text{ \AA}$, respectively (Fig. 1-3). This compound exhibits good oxygen ionic conducting properties, comparable with YSZ and LAMOX [37] at low temperature. As mentioned above, various electrolytes with the fluorite-type structure have been investigated for use in SOFCs [38,39].

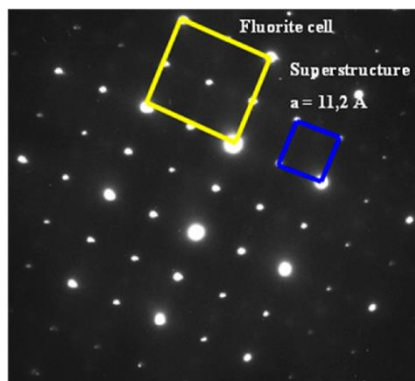


Fig. 1-3 Electron diffraction pattern of $\text{La}_{10}\text{W}_2\text{O}_{21}$ ($2 \times 2 \times 2$ anion-deficient fluorite-related superstructure) in the (1 0 0) plane of the reciprocal lattice [36]. Among weak superlattice reflections, the strong reflections from fluorite-type sub-cell are systematically observed.

SYNROC

There are high-level waste (HLW) including radioactive materials generated from nuclear reactor facilities, nuclear fuel cycle facilities and etc., which requires treatment for heat generation from HLW in the disposal of waste. HLW is a liquid waste containing fission products and actinide elements, which are mainly generated by reprocessing of spent nuclear fuel. To treat these radioactive wastes, SYNROC such as zirconolite can be used to solidify radioactive waste in a thermally and chemically stable state by distributing the radionuclide contained in HLW as a main/accessory component in a specific site in the crystal structure of the SYNROC. These solidified wastes are disposed at depths of 300 m or more, and they are superior in long-term stability and leaching resistance compared with other solidification methods such as glass [40,41].

High strength structural ceramics

A partially stabilized zirconia ceramics, containing cubic and tetragonal phases, can be prepared by adjusting the amount of dopant. Since the tetragonal phase transforms into monoclinic phase around the crack with the associated volume expansion, this phase transformation can then put the crack into compression, retard its growth and enhance the fracture toughness (called as transformation toughening). Thus, the mechanical strength of the partially stabilized zirconia is superior to fully stabilized zirconia [42,43].

Oxygen gas sensor and catalyst

Anion-deficient fluorite-related structures, such as YSZ and pyrochlore, are known as potential important applications, *e.g.* oxygen gas sensors and catalysts [44,45]. The zirconia sensors can detect a small amount of CO in air, and its sensing mechanism of the sensor has been investigated. In addition to this, catalytic data on the oxide pyrochlore system $\text{Pb}_2\text{PbRu}_{2-x}\text{O}_{6+d}$ containing dispersed platinum on the surface have been reported.

1.3 History and features of murataite

1.3.1 Natural murataite

Murataite, a complex oxide with the general formula $(\text{Na, Y, Er})_4(\text{Zn, Fe})_3(\text{Ti, Nb})_6\text{O}_{18}(\text{F, OH})_4$, was found in a pegmatite in the St. Peters Dome area, Colorado in 1974 and named by Adams *et al.* in honor of Kiguma Jack Murata, geochemist of the U.S. Geological Survey, in recognition of his pioneer work in the spectrochemical analysis and geochemistry of rare-earth elements in minerals [1]. The fragments of a black, submetallic mineral was characterized by a powder X-ray diffraction (XRD) technique and identified as a new species. A photo of natural mineral murataite was shown in Fig. 1-4 [46]. The mineral was cubic, and considered to be space group $F432$, $Fm3m$, or $Fm3$; $a = 14.863(5) \text{ \AA}$; $Z = 8$. Its physical and optical properties were also characterized: *e.g.* the reflectance is 13.6 ± 0.14 percent (air) at 545 nm wavelength; Microhardness $\text{HV}_{100} = 827$; Density (meas.) = 4.69 g/cm^3 ; (calc.) = 4.64 g/cm^3 .

In 1995, Ercit and Hawthorne have solved the crystal structure of murataite, space group $F\bar{4}3m$, $a = 14.886(2) \text{ \AA}$, by Patterson methods [2]. The ideal formula is $(\text{Y, Na})_6(\text{Zn, Fe})_5\text{Ti}_{12}\text{O}_{29}(\text{O, F})_{10}\text{F}_4$ with $Z = 4$, but its simple appearance conceals extensive cation disorder within the structure. This crystal structure contains four symmetrically independent cation positions (Fig. 1-5). Three octahedral share edges to form a compact $M_3\text{O}_{13}$ group, and four of these groups link by sharing corners to form a tetrahedral cage with the center of T site, resulting Keggin-structured $^{[4]}T^{[6]}M_{12}\text{O}_{40}$ ($T = \text{Zn, Al}$; $M = \text{Ti}$) considered to be the fundamental building block of murataite structure (Fig. 1-5 (a)).



Fig. 1-4 An image of natural mineral murataite found in St. Peters Dome area, Cheyenne District, El Paso Country, Colorado, USA presented by Mindat.org [46].

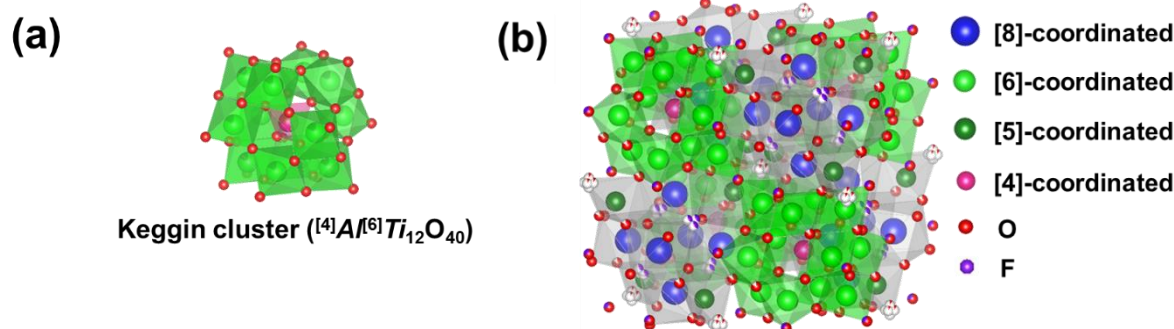


Fig. 1-5 Crystal structure of (a) Keggin cluster and (b) natural mineral murataite [2].

1.3.2 Synthetic murataite (M3, M5, M7, M8)

A synthetic murataite was firstly discovered by Peter E. D. Morgan in 1982 [47]. An apparently new cubic crystal compound in a complex Radwaste ceramics consisting of 10 crystalline phases was found and characterized by XRD, indicating the main strong lines and weak lines. Indexing of the new phase resulted in the face-centered unit cell and similarities with a fluorite structure [48]. Many weak lines was considered to be from superlattice based upon the strong peaks from sub-cell. The microprobe analysis and XRD characterization for product synthesized by solid-state reaction revealed the cubic cell parameter $a \approx 14.576 \text{ \AA}$ and chemical formula of $\text{Zr}(\text{Ca}, \text{Mn})_2(\text{Fe}, \text{Al})_4\text{Ti}_3\text{O}_{16}$, which indicates a wide variety of solid solution in murataite crystal phase. It is noticeable that the XRD pattern has the very strong lines corresponding to a sub-cell with $a/3$. Its crystal structure was recognized as a $3 \times 3 \times 3$ fluorite supercell through additional works [49,50].

Several researchers synthesized the synthetic murataite [51-54]. The detailed crystal structure of M3 was published much later by Pakhomova *et al.* in 2013 [7]. The synthetic murataite M3 was formulated $^{[8]}\text{Ca}1_6^{[8]}\text{Ca}2_4^{[6]}\text{Ti}1_{12}^{[5]}\text{Ti}2_4^{[4]}\text{AlO}_{42}$, where $\text{Ca} = \text{Ca}, \text{Mn}, \text{REE}$; $\text{Ti} = \text{Ti}, \text{Zr}, \text{Al}$; $\text{Al} = \text{Al}, \text{Fe}$ (space group: $F\bar{4}3m$), with five symmetrically independent cation positions, while natural murataite contains only four cation positions. This Russian group has been eagerly investigated the murataite ceramics for use as SYNROC material, and discovered other murataite series, $5 \times 5 \times 5$, $7 \times 7 \times 7$ and $8 \times 8 \times 8$ fluorite-type superstructures referred to as M5, M7 and M8, by very careful transmission electron microscopy (TEM) [8]. They are considered to be the polysomatic series built up from the isometric combination of M3 and pyrochlore (Py); results in M3: Py = 1:1 (M5), 1:2 (M7), 2:1 (M8), respectively [55]. This is a very rare case of a 3D polysomatic structure constructed from two parent frameworks. Recently, the crystal structures of M3, M5 and M8 analyzed by X-ray diffraction data from synthetic murataite series synthesized by melting method were reported [7,11,12]. Details of crystal structure and their fascinating features are described following sections.

Laverov *et al.* found that five volume percent of the total synthetic murataite accumulate about 40% of the total amount of uranium present in the sample [13]. This finding led to the follow-up detailed study for chemistry and properties of these materials. These modular nature of the polysomatic varieties were mainly achieved by melt methods which produces crystals with complicating zoning of mixed types (Fig. 1-6) [10,56-59]. The crystallization of zoned grains compose of murataite polytypes $\text{M7} \rightarrow \text{M5} \rightarrow \text{M8} \rightarrow \text{M3}$ with consequently reduced actinide elements from core to rim in the grains, and this multi-burrier structure is responsibility for the leach resistance and chemical durability of murataite-based ceramics containing actinides [60-65]. The radiation resistance of murataite is comparable to titanate pyrochlore [66].

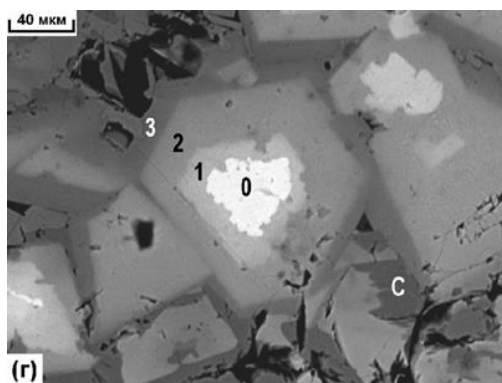


Fig. 1-6 A microstructure of murataite ceramics with 10 wt.% Tb oxide: 0, M7; 1, M5; 2, M8; 3, M3; and C, Crichtonite, respectively [10].

1.4 Chemical formula of synthetic murataite

Several chemical compositions of synthetic murataite were reported as shown in Table 1-1. In general, the study on SYNROC has been mainly carried out for the murataite series, therefore the reported chemical composition of synthetic murataite series contain actinide or rare earth elements (REE), as well as natural mineral murataite. Only Morgan's first research on synthetic murataite reports an actinide / REE -free murataite M3 ceramics. In addition to this, Mn is believed to be essential element for the formation of murataite [56].

Murataite series have been observed from bulk ceramics prepared by a method of solid-state reaction / melting oxide powder mixtures in alumina, platinum, or glass-carbon crucible. Recently, the study using the Inductive cold crucible melting (ICCM) method for SYNROC has also been developed, and the chemical composition changes due to the fabrication process.

Some elements contained in murataite ceramics may occur with different valence state depending on synthesis condition [6]. The valence state of iron and manganese are typical, and some REE such as Ce, U, Np and Pu have several degrees of oxidation state. As reported by Urusov *et al.* with Mössbauer spectroscopy [70] and Yuditsev *et al.* with photoelectron spectroscopy [71], Fe and Mn were found to be mainly Fe³⁺ and Mn²⁺. The occurrence of the trivalent state of iron has good agreement with Mössbauer spectroscopy data, while Mn²⁺ is predominant; Mn (III), Mn (IV) and Fe (II) state may be also present. XANES data exhibited 60-70% of total Mn in a divalent and 20-30% in a trivalent form [71, 72]. Ca, Zr, Ti and Al occur in murataite as their typical valence state.

M7 is very rare mineral and only a small amount has been confirmed in the bulk sample. No reports on its crystal structure have been reported, and even powder diffraction patterns are not presented in detail.

Table 1-1 Chemical compositions and superlattices of several murataite series determined by EDS

Chemical formula	Superlattice	Sintering condition	Ref.
Ca _{1.2} Mn _{0.8} ZrTi ₃ Al _{1.5} Fe _{2.5} O ₁₆		1300°C	[49]
Ca _{1.43} Mn _{1.3} Th _{0.16} Zr _{0.14} Ti _{5.88} Al _{1.32} Fe _{0.76} O _{20-x}	M3	1500°C, 6 h	[61]
Ca _{1.37} Mn _{1.37} U _{0.16} Zr _{0.20} Ti _{5.45} Al _{1.50} Fe _{0.95} O _{18.09}		ICCM	[62]
Ca _{1.83} Mn _{3.10} U _{0.64} Ti _{9.30} Fe _{0.13} O _{25.09}		1400°C, 5h + 1200°C, 5 h	[58]
Ca _{2.51} Mn _{1.51} Th _{0.60} Zr _{0.99} Ti _{8.26} Al _{0.66} Fe _{0.47} O _{27-x}		1500°C, 6 h	[61]
Ca _{2.54} Mn _{1.54} U _{0.56} Zr _{0.88} Ti _{7.80} Al _{0.87} Fe _{0.81} O _{25.34}		ICCM	[62]
Ca _{1.94} Mn _{1.18} U _{0.33} Zr _{0.56} Ti _{5.74} Al _{0.85} Fe _{0.5} O _{18.3}	M5	1400-1600°C	[67]
Ca _{1.5} Mn _{1.35} U _{0.17} Zr _{0.17} Ti _{5.5} Al _{1.52} Fe _{0.94} O _{18.5}		ICCM	[67]
Y _{2.81} Mn _{3.08} Ti _{9.11} O _{25.96}		1300°C, 4 h + Plasma flare	[68]
Ca _{2.70} Mn _{1.16} U _{0.51} Zr _{0.90} Ti _{6.69} Al _{0.51} Fe _{0.51} O _{21.59}		~1380-1450°C, 5 h	[69]
Ca _{3.86} Mn _{3.01} U _{1.55} Ti _{10.58} O _{31.84}	M7	1400°C, 5 h + 1200°C, 5 h	[58]
Y _{4.53} Mn _{3.11} Ti _{11.36} O _{32.95}		1300°C, 4 h + Plasma flare	[68]
Ca _{4.10} Th _{0.87} Mn _{2.75} Zr _{1.11} Ti _{14.46} Al _{1.77} Fe _{0.95} O _{47-x}		1500°C, 6 h	[61]
Ca _{4.33} Mn _{3.00} U _{0.86} Zr _{1.10} Ti _{13.51} Al _{1.78} Fe _{1.42} O _{42.07}		ICCM	[62]
Ca _{1.65} Mn _{1.46} U _{0.25} Zr _{0.19} Ti _{5.65} Al _{1.01} Fe _{0.79} O _{17.6}	M8	1400-1600°C	[67]
Ca _{2.02} Mn _{1.62} U _{0.26} Zr _{0.26} Ti _{6.70} Al _{1.30} Fe _{0.84} O _{21.29}		~1380-1450°C, 5 h	[69]

1.5 Crystal structures of murataite polysomatic series

3×3×3 fluorite-type superstructure (M3)

Detailed crystal structure of synthetic M3 was firstly reported by Pakhomova *et al.* in 2013 [7]. Single crystal obtained by melting in an electric furnace at 1500°C with subsequent cooling to room temperature was used for single crystal XRD analysis. The XRD was collected more than a hemisphere of data up to $\theta_{\max} = 35.92^\circ$ using monochromatic $\text{MoK}\alpha$ radiation on a Bruker APEX II diffractometer equipped with a charge-coupled device (CCD) area detector. The structure was solved by direct methods and refined to $R_1 = 0.063$ by using SHELXL program package for all structural calculations; $\text{Ca}_{3.00}\text{Mn}_{2.50}\text{Fe}_{0.29}\text{Ti}_{13.88}\text{Tb}_{2.24}\text{Al}_{0.79}\text{Zr}_{2.04}\text{O}_{42}$, $a = 14.676(15)$ Å, face-centered cubic, space group $F\bar{4}3m$ (216), $Z = 4$. The final crystal structure model described as anion-centered, (-110) section of the reciprocal diffraction space given by a STOE IPDS II diffractometer with an imaging-plate detector and structural parameters are shown in Fig. 1-7 and Table 1-2.

The chemical formula of synthetic M3 can be written as $^{[8]}CaI_6^{[8]}Ca2_4^{[6]}TiI_{12}^{[5]}Ti2_4^{[4]}AlIO_{42}$, where $Ca = Ca, Mn, \text{REE}$; $Ti = Ti, Zr, Al$; $Al = Al, Fe$, with five crystallographically independent cation positions. Three $TiIO_6$ octahedral share their O3-O2 edges to form TiI_3O_{13} trimers. Four trimers are linked by sharing the O1 atoms, resulting in the formation of the α -Keggin cluster $^{[4]}AlI^{[6]}Ti_{12}O_{40}$ with the center of Al site (Fig. 1-8 (a)), which is considered to be the fundamental building block of murataite structure as well as a natural mineral M3. Polymerization of Keggin cluster through the O5 atoms results in the formation of a 3D nanoporous octahedral framework (Fig. 1-8 (b)). The Keggin cluster framework interpenetrates with the metal-oxide substructure (anion-centered framework), containing $Ca1, Ca2, Ti2, O4, O6, O7$ and $O8$ sites, which can be considered as a derivative of the fluorite structure. Diffuse streaks and noninteger reflections in Fig. 1-7 (b) are due to the murataite grain containing the heterogeneity with small coherent intergrowth zones of other murataite varieties such as M5 and M8 incorporated into the major M3 phase (Fig. 7 (b)).

It is noted that the atomic displacement parameters for the O6, O7 and O8 sites are much larger than those for the other O sites. This large displacement is believed to be the fact that these atoms do not belong to the strongly bonded octahedral framework and form bonds to non-octahedral cations only, which are affected by disorder and formation of vacancies.

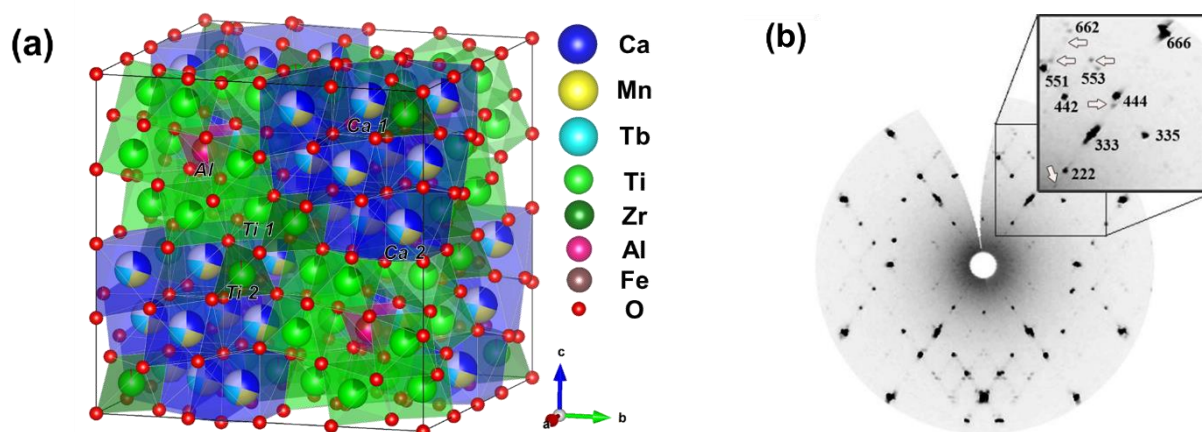


Fig. 1-7 (a) Crystal structure model of synthetic M3-type murataite and (b) (-110) section of the reciprocal diffraction space [7]. The 8-, 6-, 5- and 4-coordinated polyhedrons are colored to blue, light green, dark green and red, respectively. White arrows indicating diffuse streaks and non-integer reflections are shown inset.

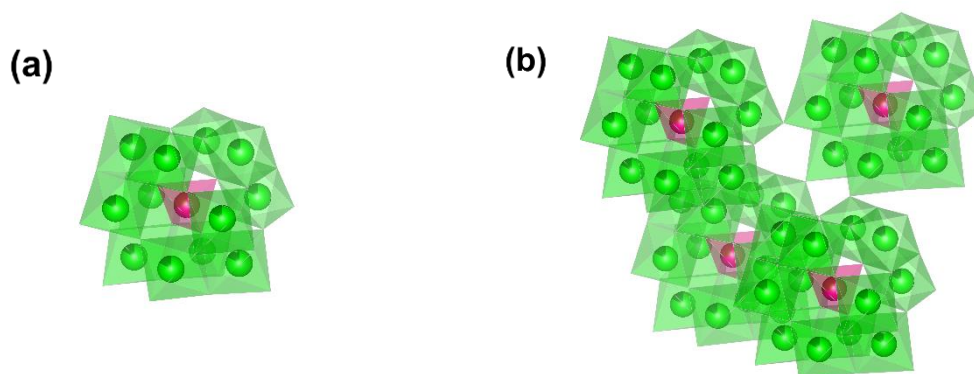


Fig. 1-8 (a) The formation of the α -Keggin cluster $^{[4]Al}^{[6]Ti}_{12}O_{40}$ with the center of Al site and (b) the formation of a 3D nanoporous octahedral framework by polymerization of Keggin cluster.

Table 1-2 Structural parameters for synthetic M3-type murataite. Atomic positions conform to the space group $F\bar{4}3m$ (216) in International Tables for Crystallography Vol. A [73].

Atom	x	y	z	U_{eq} (\AA^2)	Site occupancy
Ca1	0.57877(16)	0.25	0.25	0.0204(6)	$Ca_{0.30}Mn_{0.25}Tb_{0.22}\square_{0.23}$
Ca2	0.58417(13)	0.08417(13)	0.08417(13)	0.041(1)	$Ca_{0.30}Mn_{0.25}Tb_{0.23}\square_{0.22}$
Ti1	0.41494(8)	0.08506(8)	0.25639(11)	0.0155(5)	$Ti_{0.83}Zr_{0.17}$
Ti2	0.58144(11)	0.08144(11)	0.41856(11)	0.0158(8)	$Ti_{0.98}Al_{0.02}$
Al	0.25	0.25	0.25	0.021(2)	$Al_{0.71}Fe_{0.29}$
O1	0.46306(47)	0.17634(27)	0.17634(27)	0.022(1)	O
O2	0.64423(28)	0.14423(28)	0.50457(43)	0.023(1)	O
O3	0.17972(35)	0.17972(35)	0.17972(35)	0.019(2)	O
O4	0.50	0	0.50	0.028(5)	O
O5	0.50	0	0.21864(68)	0.029(2)	O
O6	0.50	0	0	0.07(1)	O
O7	0.66726(154)	0.16726(154)	0.16726(154)	0.18(2)	O
O8	0.66684(93)	0.33316(93)	0.16684(93)	0.06(1)	O

In the natural mineral [2], O and F ions which occupy at O4 and F site, respectively, indicate positional disorder (splitting of atoms). The O4 and O7 sites in synthetic murataite [7] correspond to the O4 and F site in the mineral, respectively. Therefore, the largest atomic displacement of O7 site in synthetic murataite has agreement with that of F site in mineral murataite.

The crystal structure of M3 is considered to contain the presence of vacancies in both cation and anion sites because of the difference of chemical formula between the ideal composition of $3 \times 3 \times 3$ fluorite supercell ($3^3 \times MO_2 = M_{27}O_{54}$, where M = cation) and present synthetic M3 ($M_{26.76}O_{42}$). The formula of natural murataite is reported as $M_{23}X_{43}$, where X = anion [2], thus the synthetic mineral has noticeably less vacancies in cation sites compared with the natural mineral.

5×5×5 fluorite-type superstructure (M5)

The crystal structure of M5 was presented by Krivovichev *et al.* in 2010 [74]. Then, the structural investigation of M5-type murataite module was developed in 2012 [11]. Single crystal XRD data was used for structural analysis. The sample of murataite M5 was obtained either by cold compaction combined with sintering at 1100-1300°C, by melting method in an electric furnace at 1500°C with subsequent cooling to room temperature or by IMCC at 1600°C. The X-ray diffraction data was collected up to $2\theta_{\max} = 56^\circ$. The structure was refined to $R_1 = 0.074$; $\text{Ca}_{24.47}\text{Mn}_{21.97}\text{U}_{7.71}\text{Al}_{2.46}\text{Ti}_{59.84}\text{Zr}_{8.56}\text{O}_{172}$, $a = 24.564(7) \text{ \AA}$, face-centered cubic, space group $F\bar{4}3m$ (216), $Z = 4$. The final crystal structure model and (110) section of the reciprocal diffraction space are shown in Fig. 1-9. The M5-type murataite can be generally formulated as $\text{Mn}_8\text{M}_{59}\text{O}_{39}[(\text{Ti}, \text{Zr})_{29}\text{O}_{86}]_2$, and contains totally 14 crystallographically independent cation positions and 23 anion sites, which demonstrates five octahedral (*Ti*), two trigonal bipyramidal (*Mn*), one 7-coordinated and six 8-coordinated *M* sites.

The structure of M5 can be described as a framework of octahedra consisting of cubic pyrochlore clusters with cavities occupied by non-octahedral cations and additional O atoms. The pyrochlore clusters are formed by TiIO_6 and Ti4O_6 octahedra and are linked together by Ti3O_6 octahedra (Fig. 1-10 (a)). The whole M5 framework is combination of linked pyrochlore clusters and murataite-like framework formed by Ti2O_6 and Ti5O_6 octahedra (Fig. 1-10 (b)) [M3: Py = 1:1 (M5)]. The murataite-like framework is geometrically identical to that observed in M3. However, it is noteworthy that, in contrast to M3, the structure of M5-type murataite contains no Keggin clusters.

In the diffraction pattern (Fig. 1-9 (b)), the streaks are considered to be either the evidence of a coherent intergrowth with other murataite phases, *e.g.* M3 and M8, or due to the modulations induced by complex pattern of cation substitutions. Among weak superlattice reflections, the reflections with $h, k, l = 5n \pm 2$ and $5n \pm 3$ for M5-type murataite are systematically enhanced.

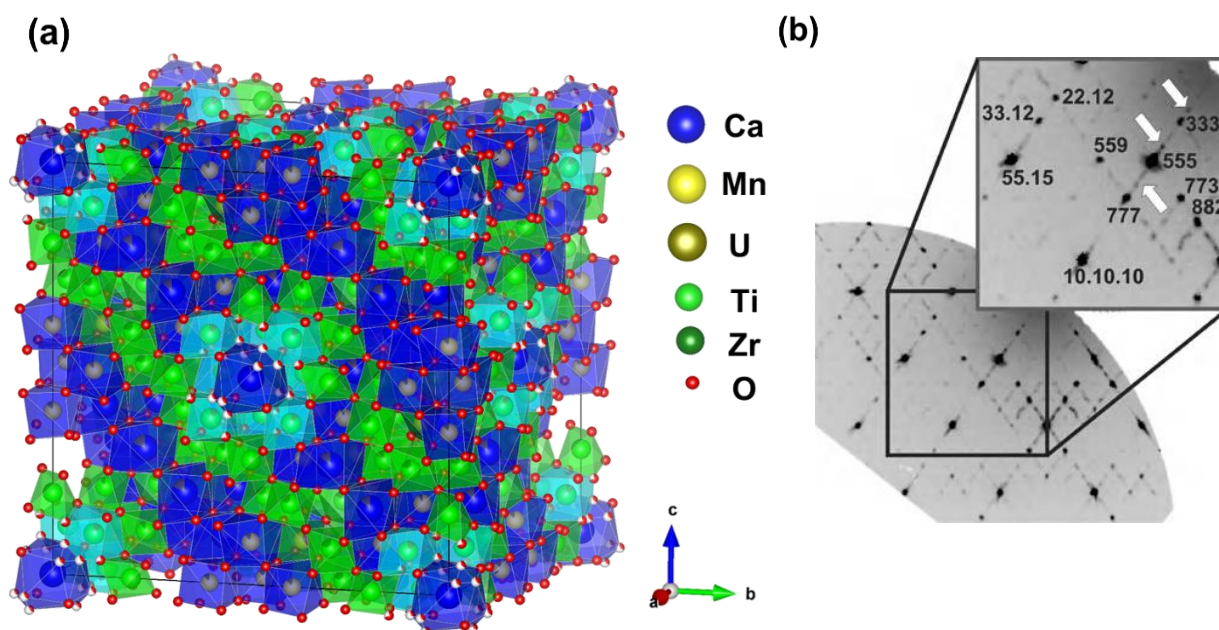


Fig. 1-9 (a) Crystal structure model of synthetic M5-type murataite and (b) (110) section of the reciprocal diffraction space [11]. The 8-, 7-, 6- and 5-coordinated polyhedrons are colored to blue, light blue, light green and dark green, respectively. White arrows indicating diffuse streaks are shown inset.

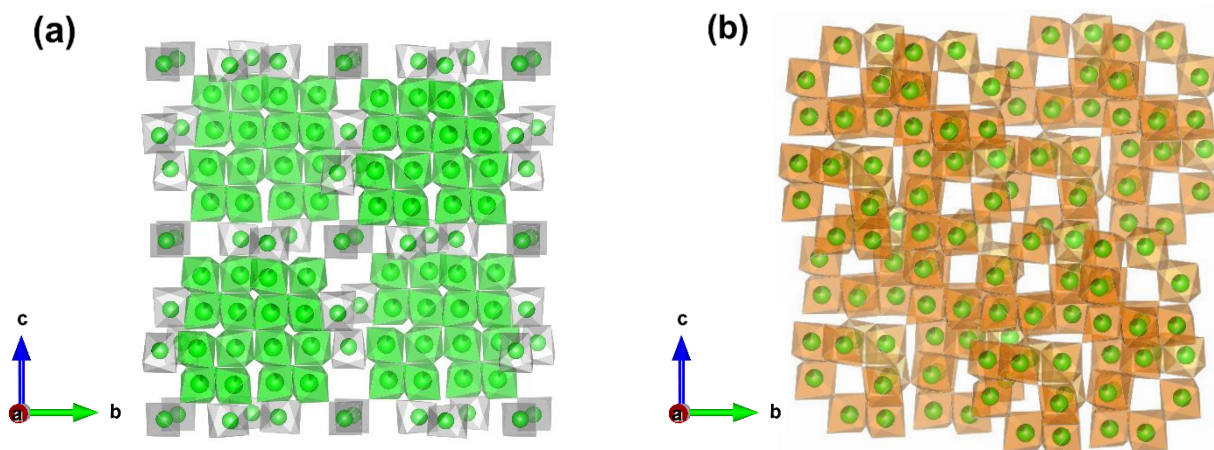


Fig. 1-10 (a) The pyrochlore clusters formed by $Ti1O_6$ and $Ti4O_6$ octahedra, linked together by $Ti3O_6$ octahedra and (b) murataite-like framework formed by $Ti2O_6$ and $Ti5O_6$ octahedra. The pyrochlore clusters and murataite-like framework are colored to light green and orange, respectively.

7×7×7 fluorite-type superstructure (M7)

The detailed crystal structure of M7 has not been reported yet while the powder diffraction data and TEM-SAED patterns were presented in several papers, *e.g.* [10,58,65,68]. Its crystal structure is also considered to be the polysomatic series built up from the isometric combination of M3 and Py; M3: Py = 1:2 (M7).

8×8×8 fluorite-type superstructure (M8)

The crystal structure of M8 was firstly reported by Laverov *et al.* in 2011 [55], and then presented in detail by Pakhomova *et al.* in 2016 [12]. A murataite grain extracted from the M8-type murataite zone, obtained by melting method in an electric furnace at 1500°C with subsequent cooling to room temperature, was used for single crystal XRD analysis. The single crystal X-ray diffraction data was collected more than a hemisphere of data up to $\theta_{\max} = 36.92^\circ$ using monochromatic $MoK\alpha$ radiation on a Bruker APEX II diffractometer equipped with a charge-coupled device (CCD) area detector. The structure was solved by direct methods and refined to $R_1 = 0.1556$ by using SHELXL program package for all structural calculations; $Al_{25.44}Ca_{55.96}Ti_{282.20}Mn_{53.72}Fe_{17.24}Zr_{15.00}Ho_{36.64}O_{823}$, $a = 39.105(12)$ Å, face-centered cubic, space group $F\bar{4}3m$ (216), $Z = 4$. The final crystal structure model and (110) section of the reciprocal diffraction space given by a STOE IPDS II diffractometer with an imaging-plate detector are shown in Fig. 1-11. The high complexity of the crystal structure and chemical composition of M8 makes the correct assignment of different chemical elements for the cation sites very challenging. In fact, the authors mentioned in the paper that the chosen procedure for structural analysis of M8 is far from being perfect, but they suggested a quite reasonable (considerably excellent) approach, taking into account the complexity of the material, its chemical heterogeneity and the imperfect quality of the experimental XRD data.

In the diffraction pattern (Fig. 1-11 (b)), among weak superlattice reflections, the reflections with $h, k, l = 8n \pm 3$ and $8n \pm 5$ for M8-type murataite are systematically enhanced. The clearly observed diffuse streaks and non-integer reflections are due to the crystal heterogeneity and possible modulations.

The crystal structure of M8-type murataite contains forty symmetrically independent cation sites; two tetrahedral, seven triangular bipyramids, fifteen octahedral, six 7-coordinated and ten 8-coordinated sites. The α -Keggin cluster in M8 has the $3m$ ($C3v$) symmetry, whereas the α -Keggin cluster in natural murataite and synthetic M8 murataite has the $\bar{4}3m$ (Td) symmetry. Four α -Keggin clusters, arranged tetrahedrally, are connected by the O6 vertices to form a zero-dimensional nanoscale cluster with its diameter equal to 25 Å which is identical to the unit cell of M3 (colored to blue in Fig. 1-12 (a)). Another zero-dimensional block in the crystal structure of M8 is a pyrochlore unit cell or a pyrochlore module, which is formed by the corner sharing of the Ti_2O_6 and Ti_7O_6 octahedra (colored to light green in Fig. 1-12 (a)). This module is about 15 Å in diameter. The murataite and pyrochlore modules, which have the structure of unit cells of the archetype materials, alternate in a three-dimensional chessboard fashion and constitute the basis of the crystal structure of M8. Each murataite module is surrounded by twelve pyrochlore units via common O51 vertices (colored to gray in Fig. 1-12 (a)), whereas each pyrochlore unit connects two murataite modules. The packing of the murataite modules and the pyrochlore-derived building blocks in the unit cell of M8 shown in Fig. 1-12 (a).

Another part of transitional substructure is formed by the octahedrally coordinated Ti_6 , Ti_9 , Ti_{10} , Ti_{12} , Ti_{13} and Ti_{15} sites; there are four of these complexes in the unit cell of M8 (Fig. 1-12 (b)). Thus, the crystal structure of M8 is based upon the heteropolyhedral framework of unusual complexity consisting of alternating murataite and pyrochlore modules immersed into the transitional substructure that combines elements of both M3 and pyrochlore. The cavities of the heteropolyhedral framework are occupied by the metal-oxide substructure formed by a complex mixture of Ca, Ho, Mn and Ti atoms, *i.e.* cations of different sizes and chemical identities (colored to white in Fig. 1-11 (a)). It is noteworthy that the crystal structure of M8-type murataite module is of an enormous complexity, which is higher than for any mineral phase ever observed.

The crystal structure of M8 is considered to contain the presence of anion vacancies because of the difference of chemical formula between the ideal composition of $8 \times 8 \times 8$ fluorite supercell ($8^3 \times MO_2 = M_{512}O_{1024}$, where M = cation) and present synthetic M8-type murataite ($M_{512}O_{823}$), not counting the vacancies which are assumed to occur at the Ca sites.

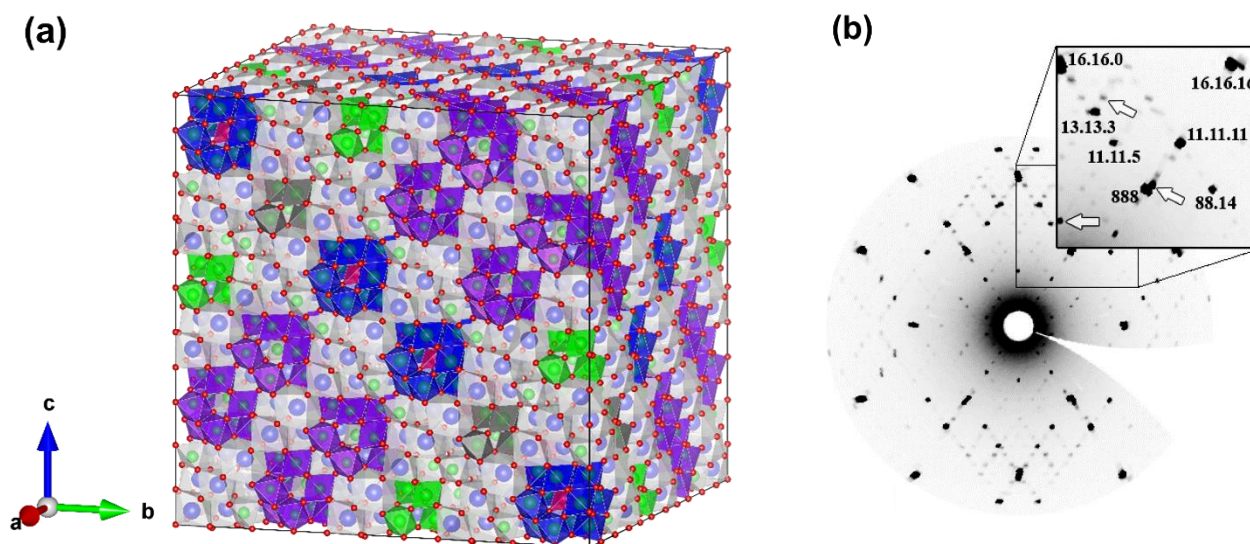


Fig. 1-11 (a) Crystal structure model of synthetic M8-type murataite and (b) (110) section of the reciprocal diffraction space [12]. The 8- and 7- coordinated, 6- and 5-coordinated and 4-coordinated sites (atoms) are colored to blue, light green and red, respectively. White arrows indicating diffuse streaks and non-integer reflections are shown inset.

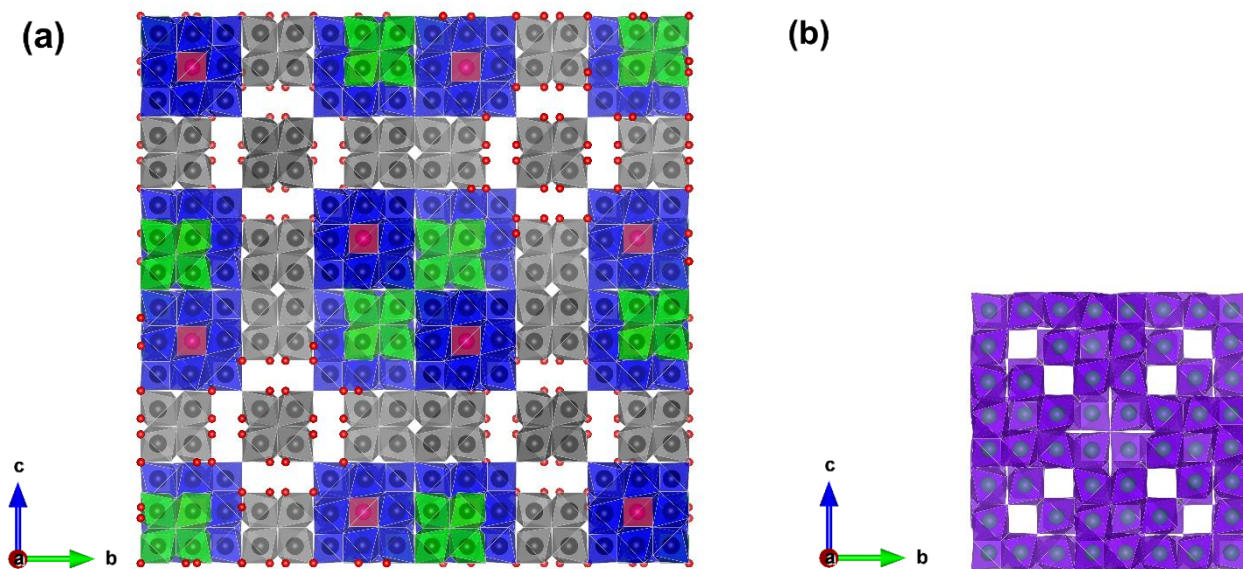


Fig. 1-12 (a) The packing of the murataite modules and the pyrochlore-derived building blocks in the structure of M8-type murataite; α -Keggin clusters (Keggin-based murataite modules), pyrochlore modules and pyrochlore units surrounding murataite modules via common O51 vertices are colored to blue, light green and gray, respectively. (b) Another part of transitional substructure formed by the octahedrally coordinated *Ti6*, *Ti9*, *Ti10*, *Ti12*, *Ti13* and *Ti15* sites, which is colored to purple.

1.6 Structural size and complexity

As shown to above sections, the murataite series have very complex and enormous fluorite-related structures (Fig. 1-13). Their modular structures are built up from two parents frameworks, and become more enormous and complex with increasing fluorite-type sub-cell.

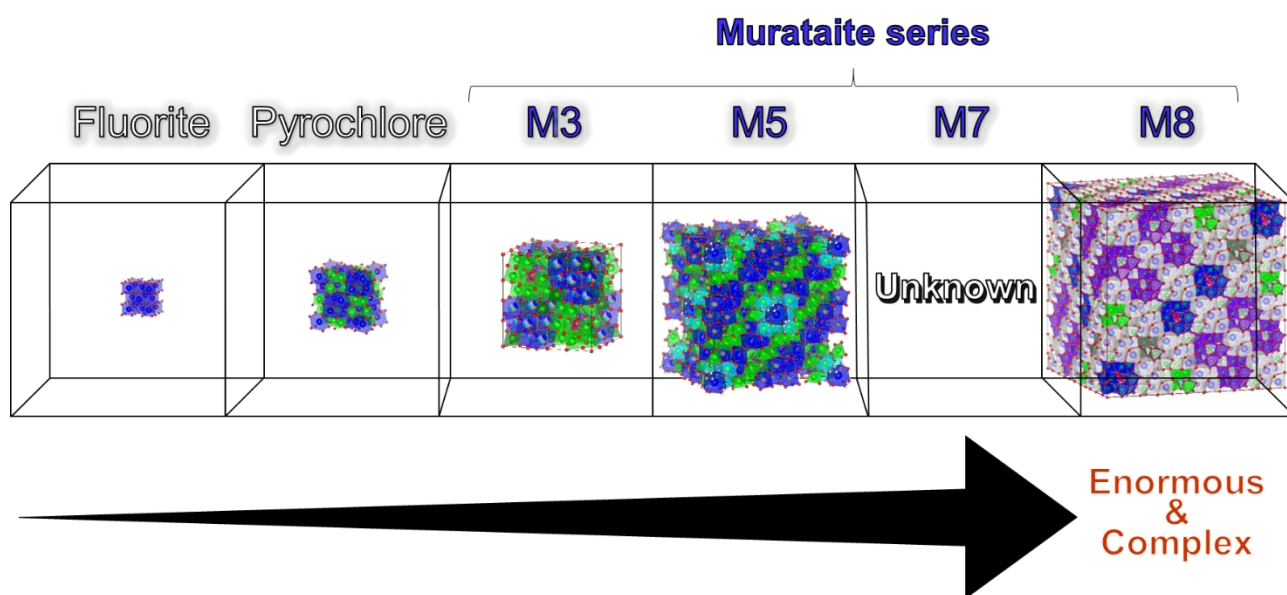


Fig. 1-13 Structural size and complexity of murataite series.

1.7 Objectives

As mentioned above, murataite series are considered to be fluorite-related ceramics of very rare case of a 3D polysomatic structure constructed from two parent frameworks, and cation substitution can typically occur at each cation site, possibly depending on the synthesis conditions. These complexities make the structural analyses of murataite series quite challenging. In this thesis, the author propose a synthetic murataites by solid-state reaction method without actinide/REE. The structural analysis of these murataite ceramics is carried out, and I suggest a new crystal structure of M3-type murataite and possible space groups of M8-type murataite. In addition to this, the author firstly evaluates the electrical properties of synthetic murataite series for widening the application of this unique structures.

This thesis consists of following chapters:

In Chapter 2, I have tried to synthesize the murataite series of M3 and M8 by solid-state reaction without REE and actinide. The microstructural observation was carried out with SEM-EDS, HAADF-STEM method and element mapping with EELS, and the differences in M3-type murataite between the samples prepared by solid-state synthesis and the earlier melting method are noted. Furthermore, I have used conventional powder X-ray diffraction to study one of the largest volume inorganic mixed oxide unit-supercell structures, M8, done so far.

In Chapter 3, I report here the first finding of a Mn-free, Fe-rich M3-type murataite. While formerly this family of polytypes were classified as titanates, now I have added high iron members, which now only have 5 cations, Ca, Ti, Zr, Al, and Fe; no Mn element believed to be essential element for fabrication of murataite series. This will necessarily simplify structural investigations of these complex synthetic versions of the murataite-pyrochlore polysomatic series.

In Chapter 4, the crystal structure of M3-type murataite was characterized with XRD using simpler M3 samples synthesized in above Chapter. I have tried to determine the site preference of Zr ion in M3-type structure by substituting Hf ion into Zr site, which indicate different diffraction intensities in XRD pattern depending on atomic scattering factor. Furthermore, an element distribution was visually characterized by element mapping with STEM-EELS to confirm the site preference of each cation, especially Zr ion.

In Chapter 5, I have investigated the electrical properties of M3 and M8. Based on four-probe D.C. method and two-probe A.C. impedance spectroscopy measurement, the electrical conductivity was measured as functions of temperature and oxygen partial pressure. Furthermore, I discuss the potential applications of murataite ceramics with taking account of their electrical properties, thermal stability and distinct lattice parameters.

In Chapter 6, the important results of the study for this thesis were summarized, and future works for murataite polysomatic series are discussed in the basis of clarified data known to date.

References

- [1] J. W. Adams, T. Botinelly, W. N. Sharp, and K. Robinson, "Murataite, a new complex oxide from El Paso County, Colorado," *Am. Mineral.*, **59** [1-2] 172-176 (1974).
- [2] T. S. Ercit and F. C. Hawthorne, "Murataite, a UB_{12} derivative structure with condensed Keggin molecules," *Can. Mineral.*, **33** [1] 1223-1229 (1995).
- [3] Buntushkin V. P., Romanovich I. V., and Timofeeva N. I., "High-temperature microhardness and certain properties of refractory oxides," *Inorg. Mater.*, **7** 1223-1229 (1971).
- [4] V. S. Urusov, N. I. Organova, O. V. Karimova, S. V. Yudintsev, and R. C. Ewing, "A modular model of the pyrochlore-murataite polysomatic series," *Crystallogr. Rep.*, **52** [1] 37-46 (2007).
- [5] K. I. Maslakov, A. Yu. Teterin, Yu. A. Teterin, K. E. Ivanov, S. V. Yudintsev, and S. V. Stefanovskii, "X-ray photoelectron study of murataite ceramics containing Th, U, Np, and Pu," *Radiochemistry*, **54** [2] 115-121 (2012).
- [6] S. V. Stefanovsky, S. V. Yudintsev, B. S. Nikonov, O. I. Stefanovsky, "Murataite ceramics doped with lanthanides and uranium," *Mater. Res. Soc. Symp. Proc.*, **893** 417-422 (2006).
- [7] A. S. Pakhomova, S. V. Krivovichev, S. V. Yudintsev, and S. V. Stefanovsky, "Synthetic murataite-3C, a complex form for long-term immobilization of nuclear waste: crystal structure and its comparison with natural analogues," *Z. Kristallogr.*, **228** [3] 151-156 (2013).
- [8] N. P. Laverov, A. I. Gorshkov, S. V. Yudintsev, A. V. Sivtsov, M. I. Lapina, "New structural species of the synthetic murataite," *Dokl. Earth Sci.*, **363** 1272-1274 (1998).
- [9] O. V. Karimova, N. I. Organova, and V. G. Balakirev, "Modulation in the murataite structure," *Crystallogr. Rep.*, **47** [6] 957-960 (2002).
- [10] N. P. Laverov, S. V. Yudintsev, S. V. Stefanovskii, B. I. Omel'yanenko, and B. S. Nikonov, "Murataite matrices for actinide wastes," *Radiochemistry*, **53** [3] 229-243 (2011).
- [11] S. V. Krivovichev, V. S. Urusov, S. V. Yudintsev, S. V. Stefanovsky, O. V. Karimova, and N. N. Organova, "Crystal structure of murataite Mu-5, a member of the murataite-pyrochlore polysomatic series," in: S. V. Krivovichev (Eds.), *Minerals as Advanced Materials II*, Berlin Heidelberg, 2012, pp. 293-304.
- [12] A. S. Pakhomova, S. V. Krivovichev, S. V. Yudintsev, and S. V. Stefanovsky, "Polysomatism and structural complexity: Structure model for murataite-8C, a complex crystalline matrix for the immobilization of high-level radioactive waste," *Eur. J. Mineral.*, **28** [1] 205-214 (2016).
- [13] N. P. Laverov, I. A. Sobolev, S. V. Stefanovskii, S. V. Yudintsev, B. I. Omel'yanenko, and B. S. Nikonov, "Synthetic murataite: a new mineral for actinide immobilization," *Dokl. Earth Sci.*, **363** [8] 1104-1106 (1998).
- [14] G. Ferraris, E. Makovicky, S. Merlino, "Crystallography of modular materials," International Union of Crystallography IUCr Monographs on Crystallography, Oxford University, USA, 2004.
- [15] J. B. Thompson Jr., "Geometrical possibilities for amphibole structures: Model biopyriboles," *Am. Mineral.*, **55** [1-2] 292-293 (1970).
- [16] J. B. Thompson Jr., "Biopyriboles and polysomatic series," *Am. Mineral.*, **63** [3-4] 239-249 (1978).
- [17] D. R. Veblen, "Polysomatism and polysomatic series: A review and applications," *Am. Mineral.*, **76** [5-6] 801-826 (1991).
- [18] F. Izumi and K. Momma, "Three-Dimensional Visualization in Powder Diffraction," *Solid State Phenom.* **130** 15-20 (2007).
- [19] D. -J. Kim, S. -H. Hyun, S. -G. Kim, and M. Yashima, "Effective ionic radius of Y^{3+} determined from

- lattice parameters of fluorite-type HfO_2 and ZrO_2 solid solutions,” *J. Am. Ceram. Soc.*, **77** [2] 597-599 (1994).
- [20] P. K. Moon and H. L. Tuller, “Intrinsic fast oxygen ionic conductivity in the $\text{Gd}_2(\text{Zr}_x\text{Ti}_{1-x})_2\text{O}_7$, and $\text{Y}_2(\text{Zr}_x\text{Ti}_{1-x})_2\text{O}_7$, pyrochlore systems,” in: G. Nazri, R. A. Huggins, and D. F. Shriver (Eds.), *Solid State Ionics, MRS Symp. Proc.* **135**, Pittsburgh PA, 1989, pp. 149-163.
- [21] S. A. Kramer and H. L. Tuller, “A novel titanate-based oxygen ion conductor: $\text{Gd}_2\text{Ti}_2\text{O}_7$,” *Solid State Ionics*, **82** [1-2] 15-23 (1995).
- [22] H. J. Rossell, “Solid solution of metal oxides in the zirconolite phase $\text{CaZrTi}_2\text{O}_7$. II: The ternary phase $\text{CaZr}_x\text{Ti}_{3-x}\text{O}_7$,” *J. Solid State Chem.*, **99** [1] 52-57 (1992).
- [23] D. J. M. Bevan, J. Drennan, H. J. Rossell, “Structure determination of the fluorite-related superstructure phases $\text{Er}_{10}\text{W}_2\text{O}_{21}$ and $\text{Y}_{10}\text{W}_2\text{O}_{21}$,” *Acta Crystall. B-struc.*, **38** [12] 2991-2997 (1982).
- [24] M. C. Williams, “Status and promise of fuel cell technology,” *Fuel Cells*, **1** [2] 87–91 (2001).
- [25] P. Singh and N.Q. Minh, “Solid oxide fuel cells: Technology status,” *Int. J. Appl. Ceram. Technol.*, **1** [1] 5–15 (2004).
- [26] M. A. J. Cropper, S. Geiger, D. M. Jollie, “Fuel cells: A survey of current developments,” *J. Power Sources*, **131** [1-2] 57–61 (2004).
- [27] P. Lamp, J. Tachtler, O. Finkenwirth, S. Mukerjee, S. Shaffer, “Development of an auxiliary power unit with solid oxide fuel cells for automotive applications,” *Fuel Cells*, **3** [3] 146–152 (2003).
- [28] B. Zhu, I. Albinsson, C. Andersson, K. Borsand, M. Nilsson, B. -E. Mellander, “Electrolysis studies based on ceria-based composites,” *Electrochem. Commun.*, **8** [3] 495–498 (2006).
- [29] S. R. Hui, J. Roller, S. Yick, X. Zhang, C. Decès-Petit, Y. Xie, R. Maric, D. Ghosh, “A brief review of the ionic conductivity enhancement for selected oxide electrolytes,” *J. Power Sources*, **172** [2] 493-502 (2007).
- [30] J. W. Fergus, “Electrolytes for solid oxide fuel cells,” *J. Power Sources*, **162** [1] 30-40 (2006).
- [31] X. Guo, E. Vasco, S. Mi, K. Szot, E. Wachsman, R. Waser, “Ionic conduction in zirconia films of nanometer thickness,” *Acta Mater.*, **53** [19] 5161–5166 (2005).
- [32] R. Pornprasertsuk, P. Ramanarayanan, C. B. Musgrave, F. B. Prinz, “Predicting ionic conductivity of solid oxide fuel cell electrolyte from first principles,” *J. Appl. Phys.*, **98** [10] 103513 (2005).
- [33] T. Hagiwara, H. Yamamura, K. Nomura, and M. Igawa, “Relationship between crystal structure and oxide-ion conduction in $\text{Ln}_2\text{Zr}_2\text{O}_7$ ($\text{Ln} = \text{Eu}, \text{Nd}$ and La) system deduced by neutron and X-ray diffraction,” *J. Ceram. Soc. jpn.*, **121** [1410] 205-210 (2013).
- [34] H. Yamamura, H. Nishino, K. Kakinuma, “Relationship between oxide-ion conductivity and dielectric relaxation in the $\text{Ln}_2\text{Zr}_2\text{O}_7$ system having pyrochlore-type compositions ($\text{Ln} = \text{Yb}, \text{Y}, \text{Gd}, \text{Eu}, \text{Sm}, \text{Nd}, \text{La}$),” *J. Phys. Chem. Solids*, **69** [7] 1711–1717 (2008).
- [35] A. Lashtabeg, J. Bradley, A. Dicks, G. Auchterlonie and J. Drennan, “Structural and conductivity studies of $\text{Y}_{10-x}\text{La}_x\text{W}_2\text{O}_{21}$,” *J. Solid State Chem.*, **183** 1095-1101 (2010).
- [36] M.-H. Chambrier, A. L. Bail, F. Giovannelli, A. Redjaimia, P. Florian, D. Massiot, E. Suard and F. Goutenoire, “ $\text{La}_{10}\text{W}_2\text{O}_{21}$: An anion-deficient fluorite-related superstructure with oxide ion conduction,” *Inorg. Chem.*, **53** 147-159 (2014).
- [37] P. Lacorre, F. Goutenoire, O. Bohnke, R. Retoux, Y. Laligant, “Designing fast oxide-ion conductors based on $\text{La}_2\text{Mo}_2\text{O}_9$,” *Nature*, **404** [6780] 856–858 (2000).
- [38] M. Kumar, I. A. Raj, R. Pattabiraman, “ $\text{La}_{0.65}\text{Sr}_{0.35}\text{CoO}_{3-\delta}$ (LSC 6535) as a cathode material - A study on chemical reactivity of LSC with $\text{Y}_2\text{Zr}_2\text{O}_7$ pyrochlore based electrolyte for ITSOFC,” *Ionics*, **10** [5-6] 429–

435 (2004).

- [39] J. -D. Wang, Y. -H. Xie, Z. -F. Zhang, R. -Q. Liu, Z. -J. Li, “, Protonic conduction in Ca²⁺-doped La₂M₂O₇ (M = Ce, Zr) with its application to ammonia synthesis electrochemically” *Mater. Res. Bull.*, **40** [8] 1294–1302 (2005).
- [40] A. E. Ringwood, S. E. Kesson, N. G. Ware, W. Hibberson, and A. Major, “Immobilization of high level nuclear reactor wastes in SYNROC,” *Nature*, **278** [15] 219-223 (1979).
- [41] I. W. Donald, B. L. Metcalfe, R. N. J. Taylor, “The immobilization of high level radioactive wastes using ceramics and glasses,” *J. Mater. Sci.*, **32** [22] 5851–5887 (1997).
- [42] K. Kobayashi, H. Kuwajima, T. Masaki, “Phase change and mechanical properties of ZrO₂-Y₂O₃ solid electrolyte after ageing,” *Solid State Ionics*, **3-4** 489-493 (1981).
- [43] R. H. J. Hannink, P. M. Kelly, B. C. Muddle, “Transformation toughening in zirconia-containing ceramics,” *J. Am. Ceram. Soc.*, **83** [3] 461–487 (2000).
- [44] Z. Y. Can, H. Narita, J. Mizusaki, and H. Tagawa, “Detection of carbon monoxide by using zirconia oxygen sensor,” *Solid State Ionics*, **79** 344-348 (1995).
- [45] J. B. Goodenough and R. N. Castellano, “Defect pyrochlores as catalyst supports,” *J. Solid State Chem.*, **44** [1] 108-112 (1982).
- [46] <http://www.mindat.org/min-2811.html>
- [47] P. E. D. Morgan and F. J. Ryerson, “A new “cubic” crystal compound,” *J. Mater. Sci. Lett.*, **1** [8] 351-352(1982).
- [48] A. B. Harker, P. E. D. Morgan, J. Flintoff, D. R. Clarke, Proceedings of the ANS Topical Meeting on the Treatment and Handling of Radioactive Wastes, Richland Washington, 1982, pp. 335.
- [49] P. E. D. Morgan, A. B. Harker, and J. F. Flintoff, “Developments in SRP "composite" defense ceramic radwaste forms,” in: G. G. Wicks, W. A. Ross (Eds.), Nuclear Waste Management, Am. Ceram. Soc., Columbus, OH, 1984, pp. 234-246.
- [50] O. V. Karimova, N. I. Organova, V. G. Balakirev, “Modulation in the murataite structure,” *Crystallogr. Rep.*, **47** [6] 957-960 (2002).
- [51] F. J. Ryerson, “Phase equilibria of nuclear waste ceramics: the effect of oxygen fugacity,” *J. am. Ceram. Soc.*, **67** [2] 75-82 (1984).
- [52] B. D. Begg, E. R. Vance, H. Li, T. McLeod, N. Scales, and M. Bhati, “Titanate ceramic matrices for alumina-rich wastes,” *Mat. Res. Soc. Symp. Proc.*, **807** 321-326 (2004).
- [53] J. Lian, L. M. Wang, R. C. Ewing, S. V. Yudintsev, and S. V. Stefanovsky, “Ion-beam-induced amorphization and order-disorder transition in the murataite structure,” *J. Appl. Phys.*, **97** [11] 113536 (2005).
- [54] N. P. Laverov, S. V. Yudintsev, S. V. Stefanovskii, B. I. Omel’yanenko, and B. S. Nikonov, “Murataite as a universal matrix for immobilization of actinides,” *Geol. Ore Deposits*, **48** [1] 335-356 (2006).
- [55] N. P. Laverov, V. S. Urusov, S. V. Krivovichev, A. S. Pakhomova, S. V. Stefanovsky, and S. V. Yudintsev, “Modular nature of the polysomatic pyrochlore-murataite series,” *Geol. Ore Deposits*, **53** [4] 273–294 (2011).
- [56] N. P. Laverov, S. V. Yudintsev, B. I. Omel’yanenko, B. S. Nikonov, and S. V. Stefanovskii, “Murataite ceramics for the immobilization of actinides,” *Geol. Ore Deposits*, **41** [2] 85-93 (1999).
- [57] S. V. Stefanovsky, S. V. Yudintsev, B. S. Nikonov, B. I. Omelianenko, A. I. Gorshkov, A. V. Sivtsov, M. I. Lapina, and R. C. Ewing, “Pyrochlore-type phases for actinides and rare earth elements immobilization,” *Mat. Res. Soc. Symp. Proc.*, **556** [4] 27-34 (1999).

- [58] S. V. Stefanovskii, O. A. Stefanovskaya, S. V. Yudintsev, and B. S. Nikonov, "Phase relationships in systems based on Y, Gd, Mn, Ti, and U oxides with addition of Ca, Al, and Fe oxides," *Radiochemistry*, **49** [4] 354-360 (2007).
- [59] S. V. Stefanovsky, A. G. Ptashkin, O. A. Knyazev, M. S. Zen'kovskaya, O. I. Stefanovsky, S. V. Yudintsev, B. S. Nikonov, and M. I. Lapina, "Melted murataite ceramics containing simulated actinide/rare earth fraction of high level waste," WM2008 Conference, Phoenix, Arizona, 2008, Abstract #8036.
- [60] S. A. Perevalov, S. V. Stefanovsky, S. V. Yudintsev, A. V. Mokhov, and A. G. Ptashkin, "Leaching of neptunium from garnet- and murataite-based ceramics," *Radiochim. Acta*, **94** [9-11] 509-514 (2006).
- [61] S. V. Stefanovsky, S. V. Yudintsev, B. S. Nikonov, A. V. Mokhov, S. A. Perevalov, O. I. Stefanovsky, and A. G. Ptashkin, "Phase compositions and leach resistance of actinide-bearing murataite ceramics," *Mater. Res. Soc. Symp. Proc.*, **893** 429-434 (2006).
- [62] S. V. Stefanovsky, A. G. Ptashkin, O. A. Knyazev, S. A. Dmitriev, S. V. Yudintsev, B. S. Nikonov, "Inductive cold crucible melting of actinide-bearing murataite-based ceramics," *J. Alloy. Compd.*, **444-445** 438-442 (2007).
- [63] S. V. Stefanovsky, S. V. Yudintsev, S. A. Perevalov, I. V. Startseva, and G. A. Varlakova, "Leach resistance of murataite-based ceramics containing actinides," *J. Alloy. Compd.*, **444-445** 618-620 (2007).
- [64] A. N. Lukinykh, S. V. Tomilin, A. A. Lizin, S. V. Yudintsev, and S. V. Stefanovskii, "Radiation and chemical stability of a polyphaser crystalline matrix based on synthetic murataite for incorporation of actinide wastes," *Radiochemistry*, **50** [5] 541-546 (2008).
- [65] S. V. Stefanovsky, G. A. Varlakova, I. V. Startseva, S. V. Yudintsev, B. S. Nikonov, and M. I. Lapina, "Leach rates of uranium and thorium from murataite ceramics," *Radiochim. Acta*, **97** [1] 17-21 (2009).
- [66] S. V. Stefanovsky, S. V. Yudintsev, and T. S. Livshits, "New cubic structure compounds as actinide host phases," *IOP Conf. Ser.: Mater. Sci. Eng.*, **9** [1] 012001 (2010).
- [67] J. Lian, L. M. Wang, R. C. Ewing, S. V. Yudintsev, and S. V. Stefanovsky, "Thermally induced phase decomposition and nanocrystal formation in murataite ceramics," *J. Mater. Chem.*, **15** [6] 709-714 (2005).
- [68] S. V. Stefanovskii, S. V. Yudintsev, B. S. Nikonov, and O. I. Stefanovskaya, "Phase composition of ceramics in systems with oxides of rare-earth elements, manganese, and titanium," *Radiochemistry*, **49** [4] 346-353 (2007).
- [69] S. V. Yudintsev, A. A. Lizin, T. S. Livshits, S. V. Stefanovsky, S. V. Tomilin, and R. C. Ewing, "Ion-beam irradiation and ^{244}Cm -doping investigations of the radiation response of actinide-bearing crystalline waste forms," *J. Mater. Res.*, **30** [9] 1516-1528 (2015).
- [70] V. S. Urusov, V. S. Rusakov, S. V. Yudintsev, and S. V. Stefanovsky, "Examination of synthetic murataite structure using data of Mössbauer spectroscopy," *Mat. Res. Soc. Symp. Proc.*, **807** 243-248 (2004).
- [71] S. V. Yudintsev, S. V. Stefanovsky, B. S. Nikonov, K. I. Maslakov, and A. G. Ptashkin, "Structural characterization of Pu-bearing murataite ceramic," *J. Alloys Compd.*, **444-445** (2007) 606-609.
- [72] S. V. Stefanovsky, S. V. Yudintsev, B. S. Nikonov, A. A. Shiryayev, "Valence State of manganese, iron and gadolinium in murataite ceramic for immobilization of REE and actinides," V-th Conf. Radiochemistry-2006, Abstracts, Dubna Russia, October 23-28 2006, pp. 212-213.
- [73] H. Arnold, M. I. Aroyo, E. F. Bertaut, Y. Billiet, M. J. Buerger, H. Burzlaff, J. D. H. Donnay, W. Fischer, D. S. Fokkema, B. Gruber, T. H. Hahn, H. Klapper, E. Koch, P. B. Konstantinov, G. A. Langlet, A. Looijenga-Vos, U. Müller, P. M. De Wolff, H. Wondratschek, H. Zimmermann, "International tables for crystallography Vol. A," in: T. Hahn (Ed.), Springer, Netherlands, 2005, pp. 658-660.
- [74] S. V. Krivovichev, S. V. Yudintsev, S. V. Stefanovsky, N. I. Organova, O. V. Karimova, and V. S. Urusov,

“Murataite-pyrochlore series: A family of complex oxides with nanoscale pyrochlore clusters,” *Angew. Chem. Int. Ed.*, **49** 9982-9984 (2010).

Chapter 2

Synthesis and Characterization of the $3\times 3\times 3$ and $8\times 8\times 8$ Fluorite-type Superstructure with Solid-State Reaction

Chapter 2: Synthesis and Characterization of the 3×3×3 and 8×8×8 Fluorite-type Superstructure with Solid-State Reaction

In this chapter, I have tried to synthesize the murataite series of 3×3×3, M3 and 8×8×8, M8 fluorite-type superstructures by solid-state reaction without rare-earth element (REE) and actinide. A murataite series of M8 with relatively high purity and high density was successfully synthesized. HAADF-STEM observation and element mapping with EELS demonstrated a layered defect having a periodicity much larger than the lattice constant and localization of Zr ion. Furthermore, the differences of Zr site in M3-type murataite between the samples prepared by solid-state synthesis and the earlier melting method are noted.

In addition to above, I have used conventional powder X-ray diffraction (PXRD) to study one of the largest volume inorganic mixed oxide unit-supercell structures done so far. This necessitated some small-angle X-ray scattering-like observations at low angles from $<2^\circ 2\theta$ to concord with electron diffraction, which had indicated an 8×8×8 huge volume supercell of a fluorite-type basic sub-cell. Emphasis is on the detection of, possibly very weak, fingerprint, low-angle/long lines/peaks which will indicate the (often unsuspected) presence of complex polytypic arrangements of simple very strong basic sub-cells and so facilitate future synthetic studies.

2.1 Introduction

The first member of the pyrochlore–murataite modular polysomatic family [1], now dubbed M3 (nearly) isotopic with the natural mineral, murataite [2], was discovered during research on radwaste disposal, in a mixture with many cations [PDF 00-036-0138 (ICDD, 1986)]. It was recognized as a 3×3×3 fluorite supercell (structurally very similar to the mineral murataite, M, but with a surprisingly very different elemental content) [3-4]. The detailed crystal structure was published much later [5].

The well-known 2×2×2 cousin is pyrochlore, Py, also frequently considered for radwaste disposal. Subsequently in a superior research effort in Russia, aimed specifically at radwaste disposal, it was discovered that there were a series of modular polytypes between Py and M, such as M5, M7, M8, in addition to M3 [6]; other packing variants are probably yet, likely soon, to be revealed. Moon tranquillityite found during the Apollo 11 mission [7], was initially amorphous, but now appears plausibly to be one of these. The regions connecting the fluorite-type sub-cells can vary in fine detail.

The new polytypes, identified by very careful electron diffraction, were first achieved by melt methods; these produced good-sized crystals but with zoning (a downside for single-crystal XRD but a plus for radwaste entombment). The poly-types are most routinely made by simple mixed oxide firings, whereupon, the PXRD method is the method of choice for simplicity and speediness in monitoring exactly how a day-to-day synthesis program may be proceeding, bearing in mind the many variables, of about six cation content ratios, the temperatures and times of syntheses and so forth.

In this chapter, I have individually synthesize the murataite series, M3 and M8, by the standard ceramic procedure of co-firing oxides. Unlike conventional procedure, synthesis of murataite samples were carried out without REE and actinide, resulting in a low cost and environmentally friendly processing. In addition, microstructural observation was carried out to determine the superstructure of murataite series and synthesize a phase-pure murataite sample.

Very large unit cells turn out to be much more difficult to analyze with advanced powder methods, such

as a Rietveld method; analysis on the largest oxide unit cell attempted so far (only three cations), was published as $\text{La}_3\text{Ti}_5\text{Al}_{15}\text{O}_{37}$ [8]. It was later corrected to the originally proposed $\text{LaTi}_2\text{Al}_9\text{O}_{19}$ [9] with the aid of the subsequent single-crystal determination of isomorphous $\text{SrTi}_3\text{Al}_8\text{O}_{19}$ [10] and checked (as always required today) with bond–valence sums [11]. The unit cell of M8 considered here, with six or more cations in a mixed oxide, is much larger by volume, in fact about three times larger, than an inorganic one previously referred to as “a giant unit cell” [12].

It is perhaps astonishing to have synthesized, by the standard ceramic procedure of co-firing oxides, an ~90% pure very complex oxide crystal type containing Al, Ca, Fe, Mn, Ti, and Zr, with an enormous face-centered cubic (FCC) unit cell with $a = 39.269 \text{ \AA}$ units. It is a member of the pyrochlore–murataite modular polysomatic family with an eightfold supercell of a fluorite-type basic sub-cell, viz. M8 (*i.e.* containing $8 \times 8 \times 8 = 512$ basic sub-cells, about 5250 atoms and 40 distinct symmetry cation positions [13-14]).

The natural mineral, an M3 [15] is known to contain many defects that include mixed polytypic layers and this probably applies to the “reconstituted-by-heating” tranquillityite [7]. In addition, the main diffraction peaks of the supercells, derived from the similar basic sub-cells, means, close overlaps occur for all the polytypes at all the strongest peaks [16]. Therefore, for quick analysis, we need accurate PXRD patterns especially emphasizing the lowest angle lines where these complex polytypes are most readily distinguishable.

2.2 Outline of synthesis technique

2.2.1 Method for powder preparation (Planetary ball-milling)

Powder preparation is roughly divided into two categories: mechanical and chemical methods. Mechanical methods are generally used to prepare fine-powders from naturally occurring raw materials while chemical methods are used with powders from synthetic or modified natural materials as starting material [17]. In this study, I selected a one of the mechanical method, planetary ball-milling process, to get a well-mixed powders with fine particles. Ball milling is one of the simplest and common mechanical technique for preparing the fine powder. The grain size depends on the milling speed, milling time, atmosphere of milling, the ball size and material of milling media such as ZrO_2 , SiO_2 and so on [18].

2.2.2 Sample compaction (Cold isostatic pressing)

In order to promote the reaction of mixed powder samples, green pellets are generally prepared by molding. A cold isostatic pressing (CIP) is a technique to prepare the green sample at high density by isotopically applying pressure in a liquid such as water or oil at room temperature. Generally, sample is covered with a rubber tube to prevent contact with water during the pressing.

2.2.3 Method for sintered sample fabrication

The sintering process is a thermal treatment of a powder or compact sample at a high temperature below the melting point of the main constituent phase for the purpose of increasing its strength by bonding together the

particles [19]. Densification and grain growth occur during this process. To produce a density- and phase-controlled materials from ceramics powders, I selected solid-state reaction method (reactive sintering method). The process of a densifying compact can be separated into an initial stage, intermediate stage and a final stage [20-21]. The different changes occur at each sintering stage: neck formation and growth along the grain boundary at an initial stage, increase in density through interconnected pores extending at an intermediate stage and porosity is isolated at a final stage. In general, the densification and phase formation depend on the sintering pressure, temperature, time and powder size [22].

2.3 Experimental procedure

2.3.1 Sample preparation

Commercial CaO (99.9% purity, Kojundo Chemical Laboratory Co. Ltd.), MnO₂ (99% purity, Kojundo Chemical Laboratory Co. Ltd.), TiO₂ anatase (99% purity, Kojundo Chemical Laboratory Co. Ltd.), ZrO₂ (98% purity, Kojundo Chemical Laboratory Co. Ltd.), α -Al₂O₃ (99.99% purity, Taimei Chemicals Co. Ltd., Saitama, Japan) and α -Fe₂O₃ (99.9% purity, Wako Pure Chemical Industries Ltd.) powders were used as starting materials. The starting powders were mixed by planetary ball-milling with ZrO₂ media for 30-120 min (acceleration: 4G). The powder mixtures were sieved through a 150-mesh screen. Dense green pellet (diameter of 15 mm) was prepared by the uniaxial CIP of the mixed oxides at 200 MPa for 10 min. The green sample was then sintered at 1100-1400°C for 2-24 h in air in an alumina crucible coated with Pt foil (Fig. 2-1).

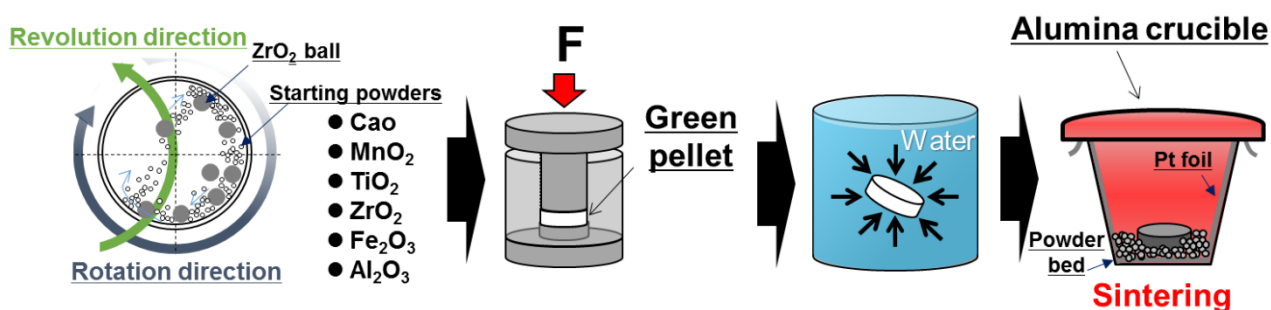


Fig. 2-1 Schematic image of sample preparation process.

2.3.2 Sample characterizations

Transmission electron microscope-selected area electron diffraction pattern (TEM-SAED) of the crushed sample was observed by aberration-corrected transmission electron microscopy (JEOL, JEM-2200FS, operated at 200 kV), in order to discover the superstructure of this particular murataite.

High Angle Annular Dark Field-Scanning Transmission Electron Microscopy (HAADF-STEM: JEOL, JEM-ARM200F, Japan) was used for microstructural observation. In the HAADF-STEM method, it is possible to obtain a z-contrast which depends on the atomic number. In addition to this, element mapping was performed by STEM- Electron energy loss spectroscopy (EELS) method.

The atomic composition on a polished section of the bulk sample was measured by scanning electron

microscopy (Hitachi TM3000, operated at 15 kV) equipped with energy dispersive X-ray spectrometry (SEM-EDS).

The phases in the pulverized sample were analyzed by PXRD (Rigaku Multiflex counter diffractometer with graphite-monochromatized Cu- $K_{\alpha 1,2}$ radiation ($\lambda_{Cu-K\alpha 1} = 1.54056 \text{ \AA}$, $\lambda_{Cu-K\alpha 2} = 1.54439 \text{ \AA}$), operated at 40 kV and 40 mA), using a reflection-free single-crystal silicon stage. The slit sizes of divergence slit (DS), scatter slit (SS) and receiving slit (RS) were 1° , 1° and 0.15 mm, respectively.

2.3.3 XRD characterization of the large-volume unit cell: M8

The first possible FCC line/peak of M8, the (111), would be expected at about $2\theta = 3^\circ$, so special steps must be taken to enable searching at unusually low 2θ angles by masking the background - mimicking a small-angle X-ray scattering (SAXS) technique (Fig. 2-2). Other modular types, with lower symmetry, could produce even lower angle lines. I present here the PXRD for M8, found to be FCC as predicted [14], exemplifying the ease of indexing and unit-supercell confirmation. Quote:- “From the crystal chemical point of view, the murataite series are the most complex mixed oxides known to date” [14].

Very slow step scans (step: 0.01°) were done with the scan time of 70 s/step in a range of $2\theta = 2\text{--}10^\circ$ with judicious masking of the incident beam and background forward scatter (Fig. 2-2). A normal scan (*viz.* without masking) was done with the scan time of 30 s/step in a range of $2\theta = 9\text{--}50^\circ$, and with the scan time of 20 s/step in a range of $2\theta = 50\text{--}150^\circ$ with the background removed. $K\alpha_2$ lines were removed by the Rachinger algorithm.

The peak search was carried out with peak search algorithm based on Savitzky-Golay method in powder pattern integrated analysis software (JADE7, RIGAKU, Japan). A fully automatic peak search software, however, has the possibility of failure in detecting the weak peaks; the murataite phase contains large numbers of weak peaks from the supercell (*i.e.* superlattice reflections); these supercell peaks were manually searched. All indices and the relative intensities were manually calculated without using any specific software.

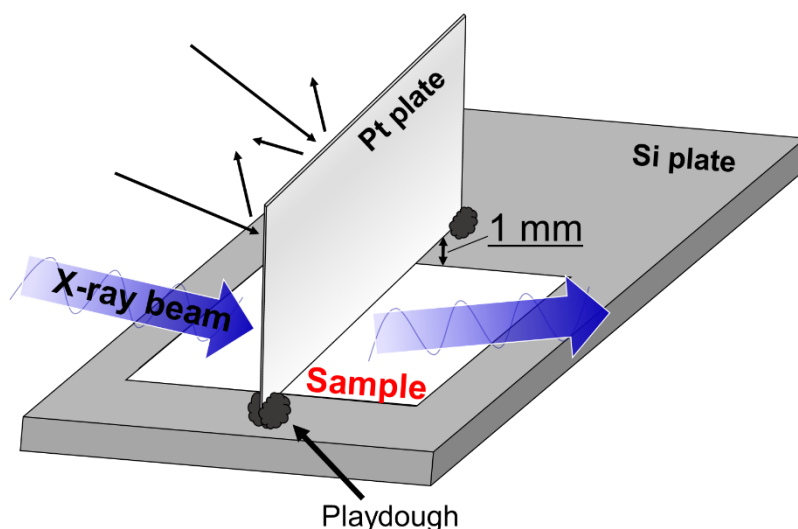


Fig. 2-2 Schematic image of very slow step scan at low 2θ angle by masking the background.

2.3.4 Synchrotron XRD for the large-volume unit cell: M8

The synchrotron radiation experiment was performed at the BL19B2 of SPring-8 in accord with Proposal No. 2016A1782 to the Japan Synchrotron Radiation Research Institute (JASRI). The pulverized sample was placed in a Lindemann capillary tube for X-ray diffraction analysis; of outside diameter 0.30 mm and wall thickness of 0.01 mm (Hilgenberg GmbH, TOHO, Japan). The X-ray wavelength was set to $\lambda = 1.0 \text{ \AA}$. The synchrotron (SPXRD) rotating transmission measurement was performed for 1h at room temperature. The optics use a standard double-crystal Si (111) monochromator, parallel-reflected beam with an imaging plate detector.



Fig. 2-3 A pulverized sample set into the Lindemann glass capillary tube taken by an optical microscope.

2.4 Results

2.4.1 Dependence of the phase formation on synthesis conditions

In order to clarify the dependence of the formation of murataite series on the synthesis conditions such as milling time, sintering temperature and sintering time, the synthesis of murataite series was systematically carried out shown in Table 2-1. Firstly, I have tried to prepare M3-type murataite series by solid-state reaction with reference to chemical composition in previous reports [4,23].

PXRD (Fig. 2-4) revealed that all of the samples synthesized under different conditions (Sample A1-5) had major murataite, minor P, pseudobrookite, and Z, zirconolite phases, but the sample was evaporated over 1400°C . The constitution phase of M3 was identified using Powder Diffraction Files (PDF) reported by Morgan (PDF 00-036-0138 (ICDD, 1982)). However, detailed diffraction data of M7 and M8 have not been clarified (at the time of 2014). In addition to this, the superstructure of murataite series changes due to a slight difference in the element ratios and synthesis conditions, and cation substitutions typically occur at each cation site, *e.g.* $\text{Ti}^{4+} = \text{Zr}^{4+}$, $\text{Al}^{3+} = \text{Fe}^{3+}$, $2\text{Ca}^{2+} = \text{Na}^{+} + \text{REE}^{3+}$ and $2\text{Ti}^{4+} = (\text{Al}, \text{Fe})^{3+} + \text{Nb}^{5+}$, thus some murataite series (superstructure), M3, M5, M7 and M8, are generally cooperated in the obtained sample. These complexities make the phase identification of murataite series difficult, especially very large unit cells such as M7 and M8, only from PXRD data. In Fig. 2-4, there were two major XRD lines from fluorite-type sub-cell of M3 and

different murataite series. The superstructure of this murataite series was determined as M8 by TEM/STEM observation later described in detail in section 2.4.3. M8 phase was generated with increasing sintering temperature or sintering time. M8 did not form at 1100°C and 1200°C, while a large amounts of P and Z phases remained. In the sintering condition of 1300°C for 2 h (Sample A5), M3 was the major phase with slight impurity of P and Z, since the content of M8 phase was very small.

SEM observation confirmed the multiphase of murataite series, P and Z in each sample (Fig. 2-5). The constitution phases of Sample A-3 (sintered at 1100°C, 24 h) was not observed due to its low density. As a result of PXRD and SEM, the control of sintering temperature demonstrated the formation of a single superstructure of murataite series, but on the other hand the density decreased. Therefore, the reducing the sintering time is effective for formation of single superstructure with high density by solid-state reaction.

Analysis of element ratios of constituent phases in each sample by SEM-EDS showed that the chemical compositions of M3 and M8 phases in each sample are relatively close. Comparison of M3 and M8 phases indicated that the sum of the content of Ca, Mn and Zr ions, which probably occupy 8 coordination sites, in M8 phase is larger than M3. Previous work [16] reported that large ions, such as actinides and Ca, is occupied into 8 coordination sites and contained larger amounts in the order of M7, M5, M8 and M3. In addition, the samples prepared by melting method produced the zoning of the murataite series in the grains; M7, M5, M8 and M3 in the arrangement from center to rim. This “multi barrier structure” demonstrates the good protection against leaching of actinides, and a similar microstructure was confirmed in murataite sample prepared by solid-state reaction. From these results, it seems that the sample prepared in this work is partially melted.

On the other hand, contents of Al and Fe ions were larger in M3 than in M8. M8 is built up from the isometric combination of M3 and Py (M3: Py = 2:1), and M3 has Keggin groups with an AlO_4 (possibly FeO_4) tetrahedron at its center; there are no Keggin group in pyrochlore. Therefore, M3 has more Keggin groups per volume, resulting in the higher Al (and Fe) contents in M3 than in M8.

Table 2-1 Synthesis conditions of prepared samples

Sample [†]	Planetary ball-milling time (min)	Sintering temperature (°C)	Sintering time (h)
A-1	120	1300	24
A-2		1200	
A-3		1100	
A-4	30	1300	6
A-5			2
B			6
C			

[†]Specified compositions (at.%) of each murataite ceramics samples are as follows:

Sample A: 14.0 CaO, 9.3 MnO₂, 41.9 TiO₂, 11.2 ZrO₂, 8.8 α -Al₂O₃, 14.9 α -Fe₂O₃ (III)

Sample B: 15.1 CaO, 9.0 MnO₂, 41.4 TiO₂, 13.2 ZrO₂, 8.7 α -Al₂O₃, 12.6 α -Fe₂O₃ (III)

Sample C: 16.0 CaO, 7.6 MnO₂, 43.9 TiO₂, 16.7 ZrO₂, 5.8 α -Al₂O₃, 10.0 α -Fe₂O₃ (III)

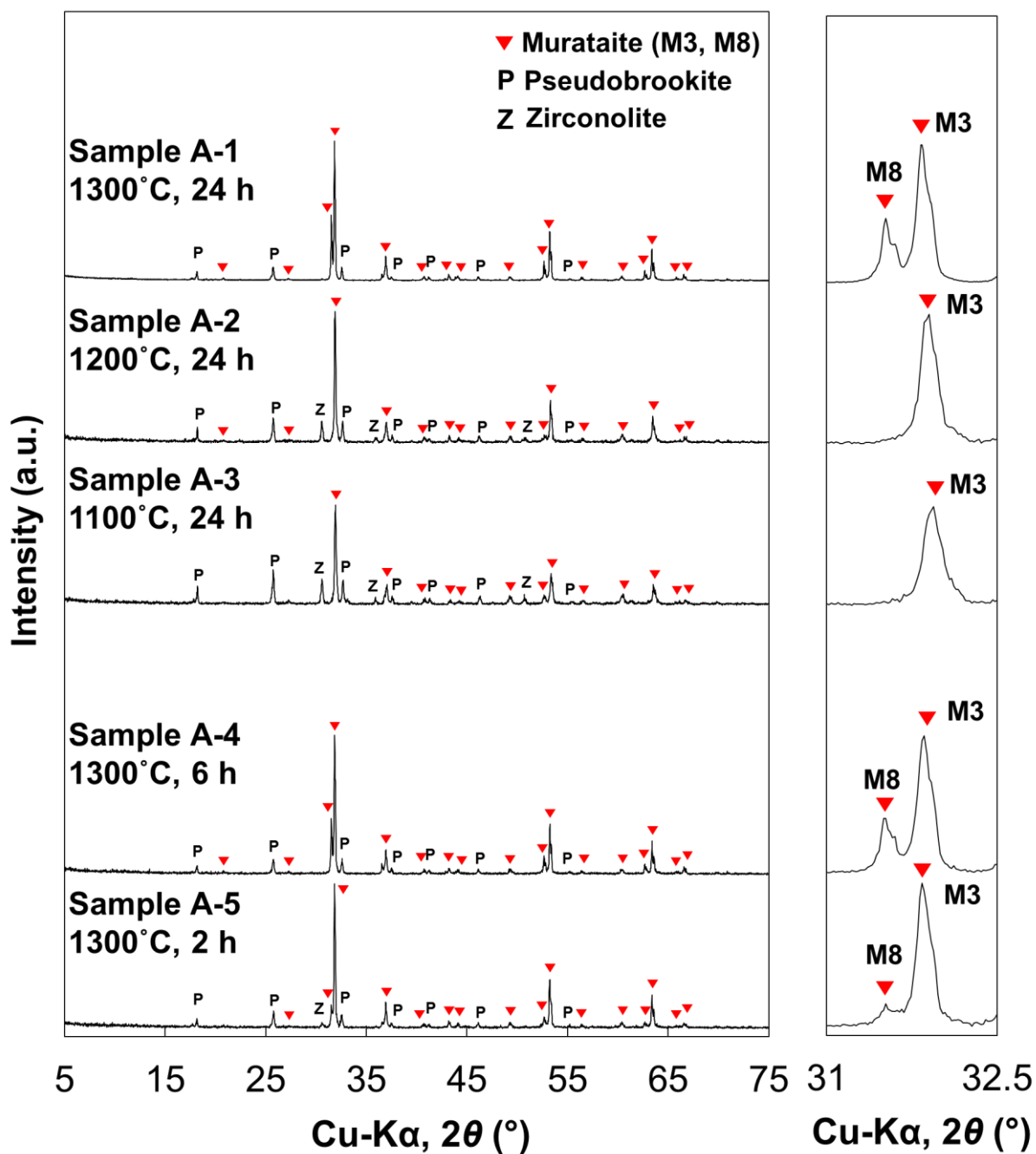


Fig. 2-4 X-ray diffraction patterns of pulverized samples synthesized with same compositions under different conditions. M3 is 3 \times 3 \times 3 fluorite-type superstructure; M8, 8 \times 8 \times 8 fluorite-type superstructure; P, Fe₂TiO₅-based pseudobrookite-type solid solution (ss); and Z, CaZrTi₂O₇-based zirconolite-2M (ss).

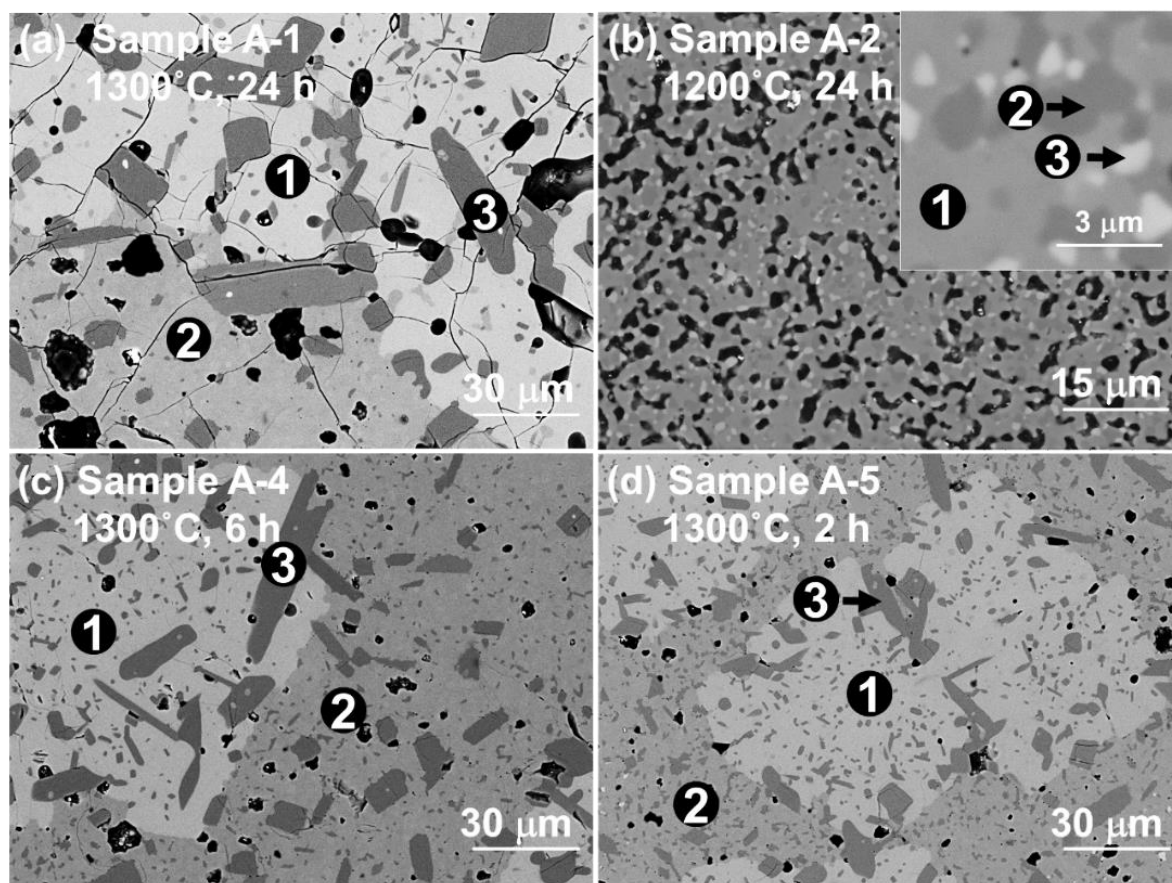


Fig. 2-5 SEM images of mirror-polished surface of the same compositions synthesized under different conditions. (a) Sample A-1: 1 is M8; 2, M3; and 3, Fe_2TiO_5 -based pseudobrookite-type (ss); (b) Sample A-2: 1 is M3; 2, pseudobrookite-type (ss); and 3, $\text{CaZrTi}_2\text{O}_7$ -based zirconolite-2M (ss); (c) Sample A-4: 1 is M8; 2, M3; and 3, pseudobrookite-type (ss); (d) Sample A-5: 1 is M8; 2, M3; and 3, pseudobrookite-type (ss). The constitution phases of Sample A-3 was not observed due to its low density.

Table 2-2 Chemical compositions of the coexisting phases in the samples synthesized under different conditions analyzed with EDS (at.%)

Element	Sample A-1		Sample A-2	Sample A-4		Sample A-5	
	M8	M3	M3	M8	M3	M8	M3
Ca	4.2	3.9	4.0	4.4	4.0	4.8	4.2
Mn	1.8	2.3	2.4	2.1	2.5	2.2	2.5
Ti	11.8	11.1	11.0	12.2	11.2	13.3	12.0
Zr	4.4	3.5	3.3	4.7	3.6	4.9	3.6
Al	3.2	4.8	4.8	3.1	4.6	3.2	4.6
Fe	5.6	6.8	6.6	5.5	6.9	6.2	7.2
O	69.1	67.5	68.0	68.0	67.2	65.4	65.7

2.4.2 Preparation of high purity murataite series

Based on the SEM-EDS analysis data of the sample sintered at 1300°C for 12 h (Fig. 2-6 and Table 2-3), I have tried to synthesize the phase-pure murataite series. SEM-EDS analysis revealed that sintered sample had minor P (i), major M8 (ii) and M3 (iii) phases. P's composition is similar to murataite series but with more iron and less calcium and zirconium. A surface observation of the sintered sample also clearly indicates anisotropic grain growth of P phase (Fig. 2-7). With reference to the element ratios obtained from M3 (iii) and M8 (ii) by EDS, I decided the chemical compositions of Sample B and C, respectively (Table 2-1).

PXRD (Fig. 2-8) shows the constituent phases of samples prepared with various chemical composition ratios. In contrast to Sample A, almost same amount of M3 and M8 phases existed in Sample B. Thus phase-pure murataite was not obtained from Sample B. On the other hand, in Sample C, although a phase of pseudobrookite and zirconolite was slightly present, a single superstructure of M8 was successfully fabricated. Incidentally, regrinding and refiring, did not improve the amount of the M8.

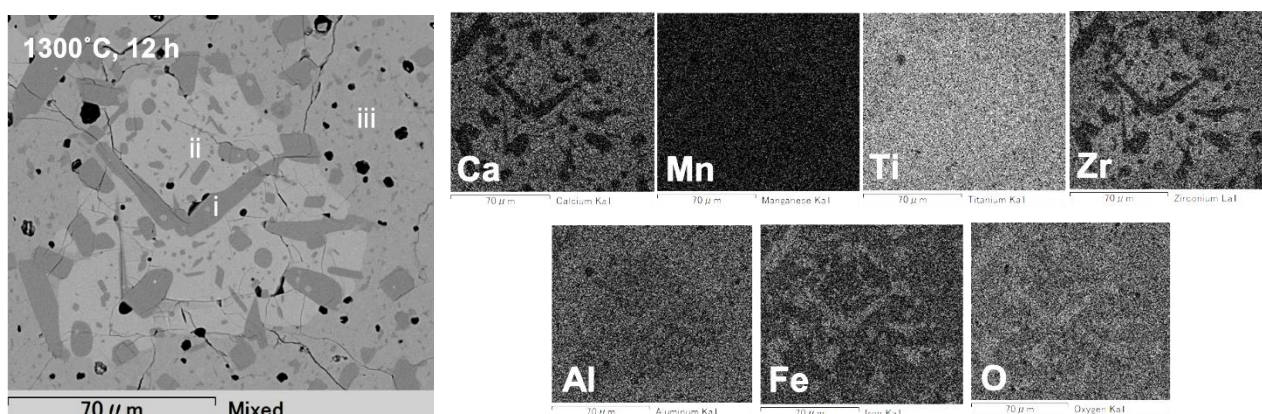


Fig. 2-6 SEM images with element mapping of mirror-polished surface sintered at 1300°C for 12 h.

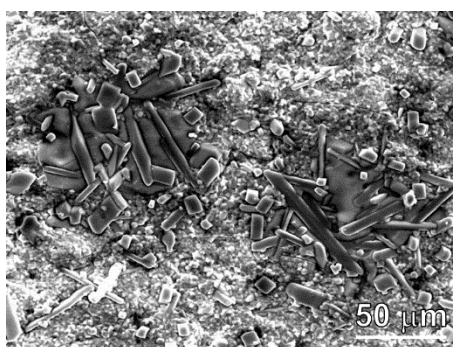


Fig. 2-7 SEM image on the surface of sintered sample.

Table 2-3 Chemical compositions of phases in samples sintered at 1300°C for 12 h (at.%)

Oxide	Ca	Mn	Ti	Zr	Al	Fe	O	Phase
i	0.828	1.890	11.958	1.191	4.577	11.291	68.265	P
ii	4.409	2.055	12.137	4.569	3.208	5.474	68.147	M8
iii	3.960	2.367	11.000	3.532	4.645	6.668	67.828	M3

SEM-EDS observation confirmed the multiphase of murataite series, P and Z in each sample (Fig. 2-9 and Table 2-4). With six elements, it is almost certain that, at 1300°C, a liquid formed from which, on cooling, Z and P crystallized and which facilitated the good crystallization of M8 as micrographic observations indicated (Fig. 2-9 (c)). By controlling the chemical composition ratio, I successfully synthesized a murataite series of M8 with relatively high purity and high density by solid-state reaction.

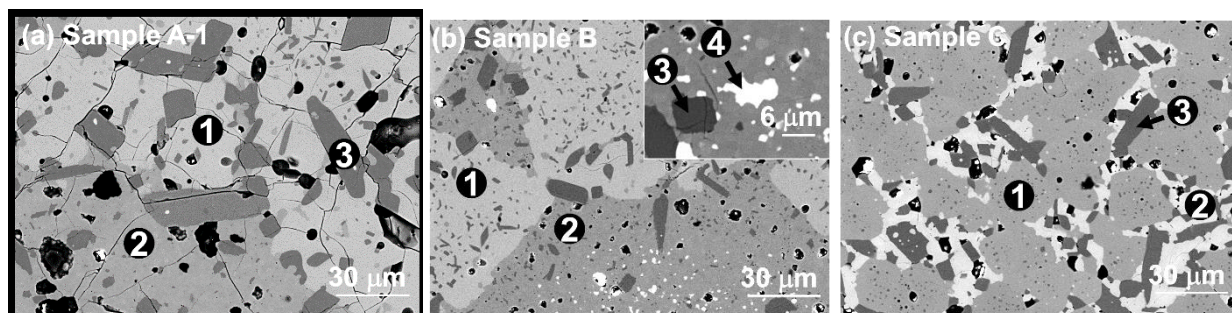


Fig. 2-9 SEM images of mirror surface of samples prepared with different powder mixtures. (a) Sample A-1: 1 is M8; 2, M3; and 3, Fe_2TiO_5 -based pseudobrookite-type (ss); (b) Sample B: 1 is M8; 2, M3; 3, pseudobrookite-type (ss); and 4, $\text{CaZrTi}_2\text{O}_7$ -based zirconolite-2M (ss); (c) Sample C: 1 is M8; 2, zirconolite-2M (ss); and 3, pseudobrookite-type (ss).

Table 2-4 Chemical compositions of the coexisting phases in the samples prepared with different powder mixtures analyzed with EDS (at.%)

Element	Sample A-1		Sample B		Sample C
	M8	M3	M8	M3	M8
Ca	4.2	3.9	4.2	3.9	4.3
Mn	1.8	2.3	1.9	2.2	1.9
Ti	11.8	11.1	11.6	10.5	12.1
Zr	4.4	3.5	4.6	3.7	5.4
Al	3.2	4.8	3.4	4.9	3.0
Fe	5.6	6.8	5.2	6.2	4.8
O	69.1	67.5	69.2	68.6	68.6

2.4.3 Microstructural observation

TEM-SAED (Fig. 2-10) revealed that the murataite phase in Sample A-1 and Sample B had M3 and M8, respectively. The hkl reflections with $h, k, l = 3n$ for M3; $h, k, l = 8n \pm 3$ and $8n \pm 5$ for M8 from FCC fluorite-type sub-cell, which size is close to that of the fluorite unit cell, are strongest in M3 and M8 murataite series, respectively. The weak reflections from the fluorite-type supercell determine the real parameters of the M3- and M8-type murataite unit cells, whereas these superlattice reflections are not observed in the conventional FCC fluorite-type structure.

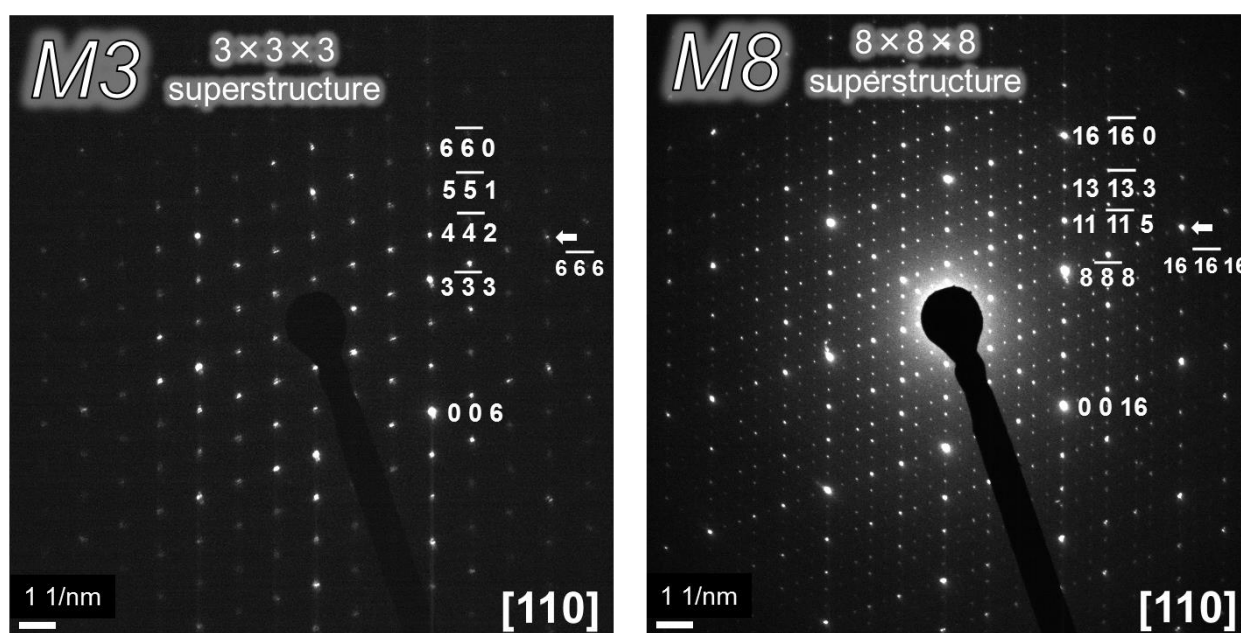


Fig. 2-10 TEM-SAED patterns of reactively sintered samples, corresponding to M3 and M8 in the (1 1 0) plane of the reciprocal lattice.

Z-contrast images were obtained by HAADF-STEM observation using crushed (a) Sample A-1 and (b) Sample B (Fig. 2-11). The technique of Z-contrast can provide the intensity of atom columns which directly reflects their mean square atomic number (Z), and the location of atom column positions is greatly simplified. The Fast Fourier Transform (FFT) clarified the superstructure of image (a) and (b) as M3 and M8, which indicated (110) and (210) plane of the reciprocal lattice, respectively. Surprisingly, in this study, a layered defect having a periodicity much larger than the lattice constant of M3 (about 15 Å) and M8 (about 40 Å) was confirmed in Z-contrast image of (a) M3 (it appears as diamond-like in the figure) and (b) M8. This finding was not reported in murataite ceramics prepared by melting method, and it was discovered for the first time in this study using solid-state reaction. In the observed images at high magnification (Fig. 2-12), the interatomic distances relatively consist with the crystal structure of M3 analyzed by XRD [5].

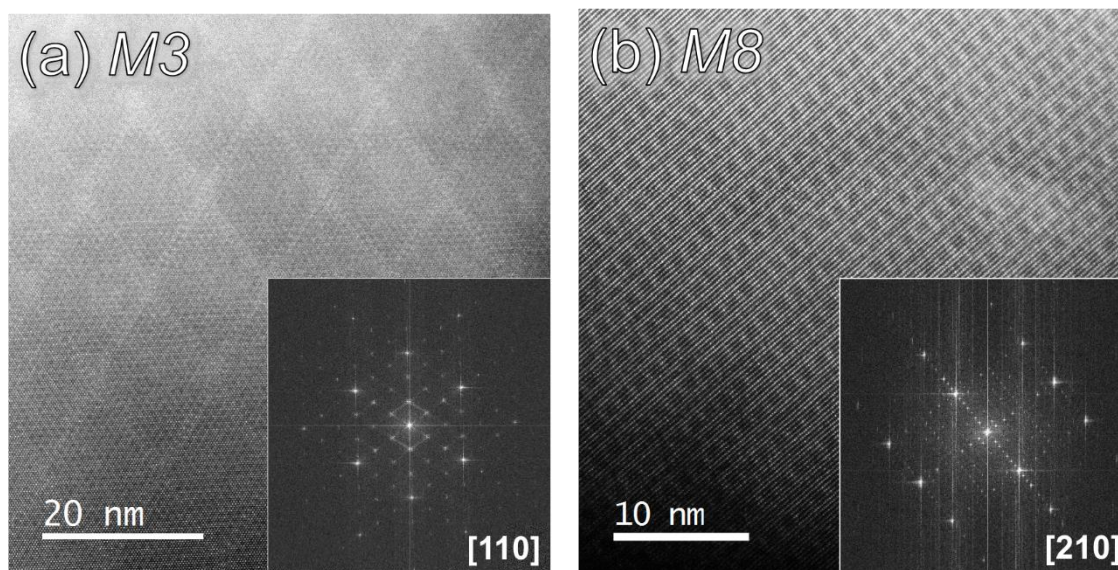


Fig. 2-11 HAADF-STEM images of reactively sintered samples, corresponding to (a) M3 and (b) M8. FFT images are shown insets, which indicate the (110) and (210) plane of the reciprocal lattice, respectively.

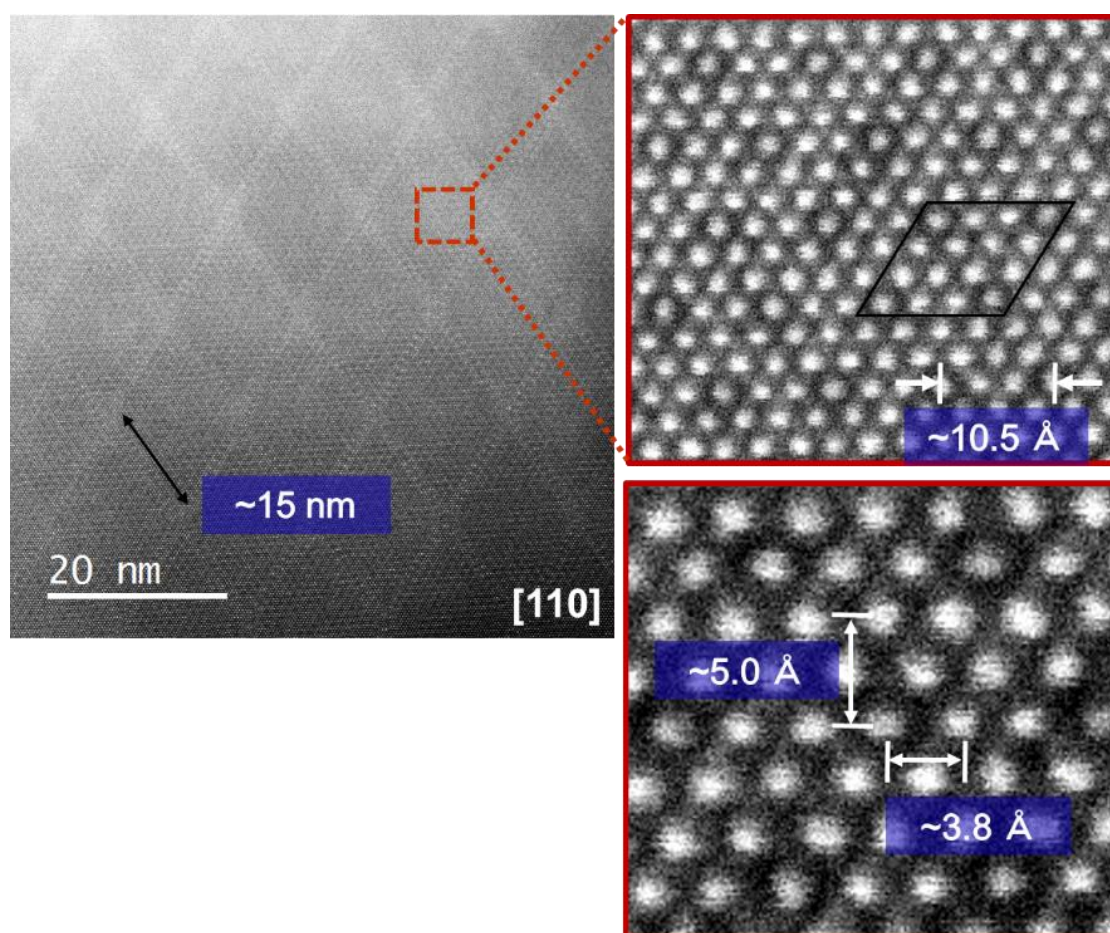


Fig. 2-12 HAADF-STEM image and expanded areas in the microstructure of M3 with a system of Ca-Mn-Zr-Ti-Al-Fe-O.

2.4.4 Element mapping for M3-type murataite

As a result of element mapping by EELS (Fig. 2-13 (upper row)), it was found that the white layered region in the HAADF-STEM image of M3 (Fig. 2-12 (a)) was a Zr-rich layer. Zr ion was unevenly distributed in diamond-like layered defect, while Al and Ti ions hardly existed. The observation results of the high magnification of the layered region (Fig. 2-13 (bottom row)) clearly exhibited the atom column of each cation. Thus, comparison of occupation positions of each cation are shown in Fig. 2-14. The element mapping at high magnification produced that Zr ions are likely to be present in the same column as Ca and Mn, on the other hand, Ti, Al and Fe ions seems to be present in the same column. It has been believed that Zr ion occupies 6 coordination of Ti sites so far ($^{[8]}Ca_6^{[8]}Ca_4^{[6]}Ti_{12}^{[5]}Ti_4^{[4]}AlO_{42}$, where $Ca = Ca, Mn, REE$; $Ti = Ti, Zr, Al$; $Al = Al, Fe$ in synthetic M3 [5]). The present observation demonstrates that Ti, Fe and Al ions are on the same column, whereas Zr is located on the same column as the Ca and Mn, which is the 8 coordination. This data is different from the result of structural analysis for M3 in the previous work [5]. However, the excitation spectrum of Zr was so weak that separation from background seems to be difficult in present work. The detailed study for the determination of site preference of Zr ion is described in Chapter 4.

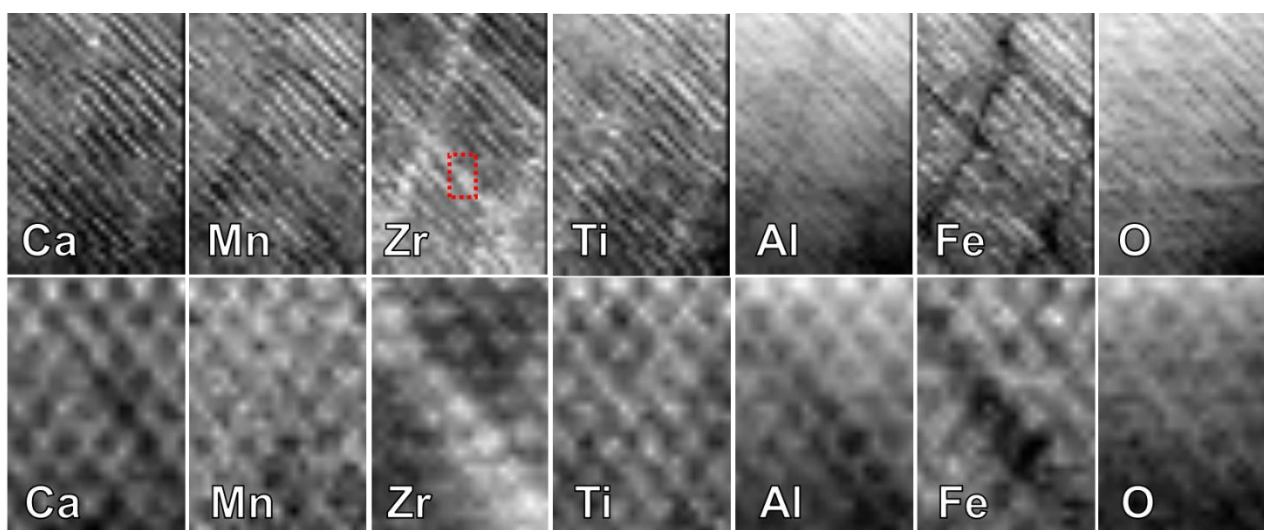


Fig. 2-13 Element mapping of low (upper row) and high (bottom row) magnification in the microstructure of M3. Expanded area (bottom row) is indicated as red square shown inset.

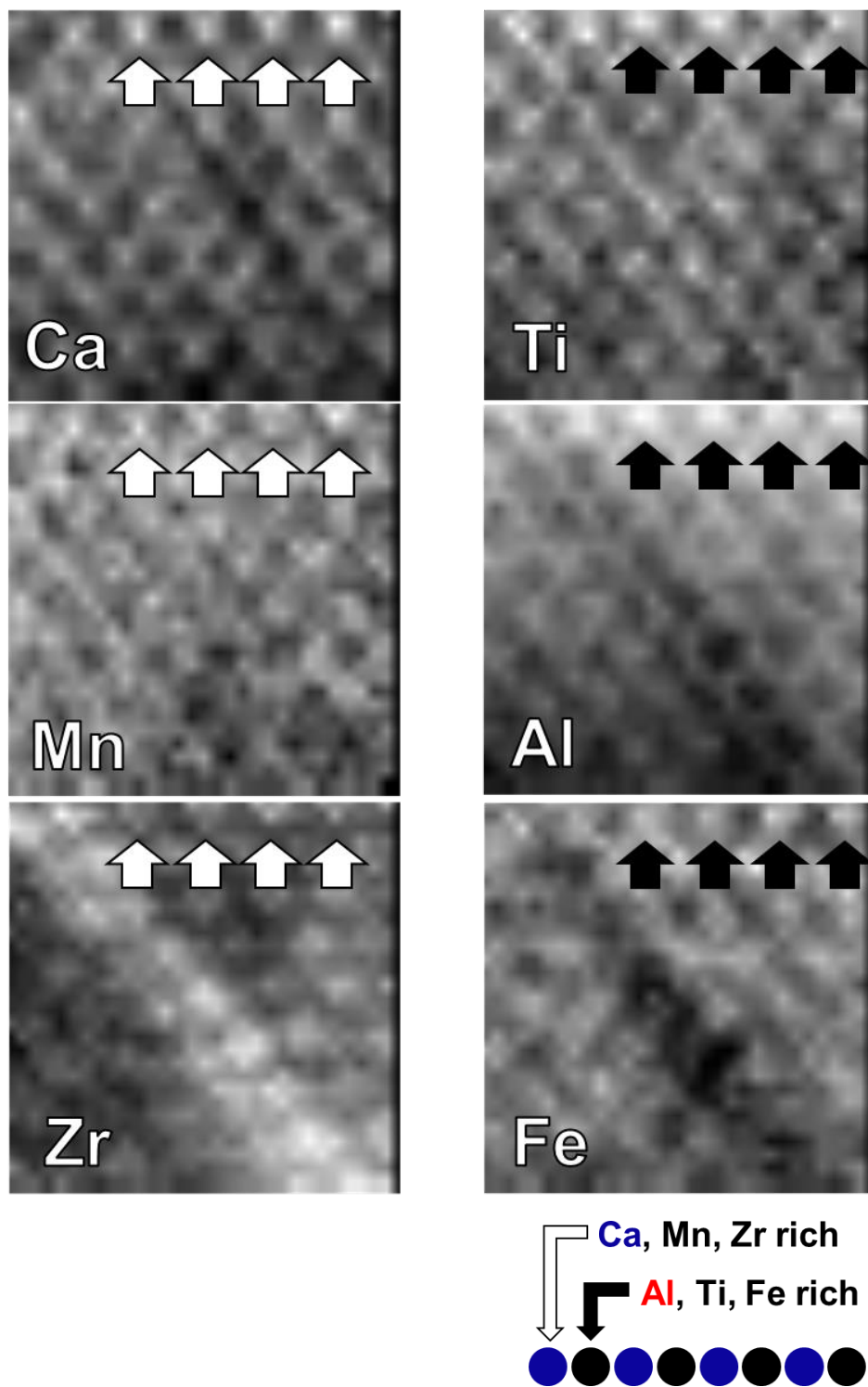


Fig. 2-14 STEM images for element mapping: white and black arrows indicate each element position, which result that there are Ca, Mn and Zr-rich column and Al, Ti and Fe-rich column.

2.4.5 PXRD characterization of the large-volume unit cell of the M8 murataite polytype

PXRD characterization for M8 murataite polytype was carried out using the Sample C, prepared with the powder mixture of the ratio of $\text{CaO} : \text{MnO}_2 : \text{TiO}_2 : \text{ZrO}_2 : \alpha\text{-Al}_2\text{O}_3 : \alpha\text{-Fe}_2\text{O}_3 = 9.6 : 7.1 : 22.1 : 37.7 : 6.4 : 17.1$ in wt.%, (viz. $16.0 : 7.6 : 43.9 : 16.7 : 5.8 : 10.0$ in mol.%), sintered at 1300°C for 6 h in air in an alumina crucible coated with Pt foil.

TEM-SAED (Fig. 2-15) revealed that the murataite phase had an M8 superstructure. Indexing for all peaks of the murataite phase were carried out mostly manually, securely aware of this.

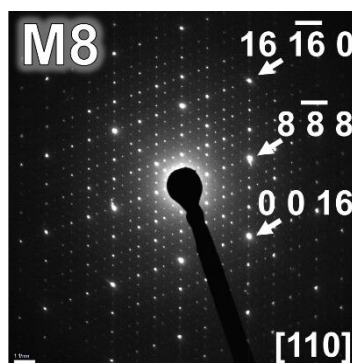


Fig. 2-15 SAED pattern of M8 in the (1 1 0) plane of the reciprocal lattice.

SEM-EDS analyses (Table 2-5) measured the atomic ratio of each element. The pseudobrookite (P)-type phase, containing much Al, Ti, and Fe elements, agrees well with the conventional formula. I concur that Mn in the starting material is an essential condition for synthetic M formation [6], where it may reside in trigonal bipyramids (as it often prefers, *e.g.* in YMnO_3 , as Mn^{3+} [24]). Moreover, Mn is known also to aid in the formation of tranquillityite [7], another reason that we think that it has similarities in this extended polytypic group. M8 has 2 α -Keggin groups with an AlO_4 tetrahedron at its center [14], resulting in the higher Al contents in M8 than in zirconolite (Z).

In Table 2-5, Z's composition is quite like M8 but with a little less Al, and P's composition is quite similar to M8 but with more iron and less zirconium. Reaction appears to be incomplete because the contents of the Z and P sum to about the same composition as the M8. With six elements, it is almost certain that, at 1300°C , a liquid formed from which, on cooling, Z and P crystallized and which facilitated the good crystallization of M8 as micrographic observations indicated (Fig. 2-9 (c)).

Table 2-5 Chemical compositions (EDS) of the coexisting phases in the sintered sample.

Oxide (wt.%)	M8	Pseudobrookite	Zirconolite
CaO	9.3	2.4	10.2
MnO ₂	6.3	6.4	3.1
TiO ₂	37.7	39.7	36.9
ZrO ₂	25.9	8.8	39.3
Al ₂ O ₃	5.9	9.9	2.7
Fe ₂ O ₃	14.9	32.8	7.9

Figures 2-16, 2-17 and Table 2-6 revealed that the resultant phases after sintering were about 90% major M8, about 5% minor $(\text{Fe, Al, Mg})_2(\text{Ti, Zr})\text{O}_5$ P, and about 5% minor $(\text{Ca, Mn})\text{ZrTi}_2\text{O}_7$ -2M Z, (PDF 00-041-1432 and 00-034-0167 (ICDD, 1988 and 1982)). In the present work, the PXRD pattern was collected in three distinct 2θ ranges, with specific experimental conditions in each of them.

The PXRD indexing (Table 2-6) confirms that M8 is FCC, with hkl all odd or all even. Weak, low angle 2θ lines are well visible but with the noticeable absence of the 1 1 1, for which there seems not to be any systematic reason, and we do not believe that it is smothered by the background. M8 conforms also to the extra condition $h00$ where $h = 4n$ only, consequently, and especially noticeable, leading to the absence of the 2 0 0. This allows for four space groups (SGs), $Fd\bar{3}(203)$, $F4_132(210)$, $Fd\bar{3}m(227)$ and $Fd\bar{3}c(228)$. Three of these SGs have $hk0$ where $h+k=4n$ only, but I do find the 6 4 0 and 12 2 0, without overlaps, to be present, thus leaving only $F4_132(210)$, not the same SG of $Fd\bar{3}m(216)$ as for M3. Further investigation with improvement in data is described in next section.

The lattice constant was calculated using only the strong certain reflections at high angles [32 0 0, 24 24 8, 32 16 0, 32 16 16, 40 8 8, 32 32 0, 40 24 8 and 48 0 0] - where all the hkl are divisible by 8, *i.e.* those from the FCC basic sub-cell. The lattice constant, a , of the M8 superstructure is $39.269 \pm 0.001 \text{ \AA}$, calculated using a Nelson–Riley extrapolation.

Here there is no rare earth so those elements are not mandatory but can play a role as they do in the work of Laverov *et al.* The full range of elements that will enter these structures is to be determined but appears to be most of the periodic table excepting, perhaps, the very largest ions - making them especially interesting for long-term radwaste sequestration.

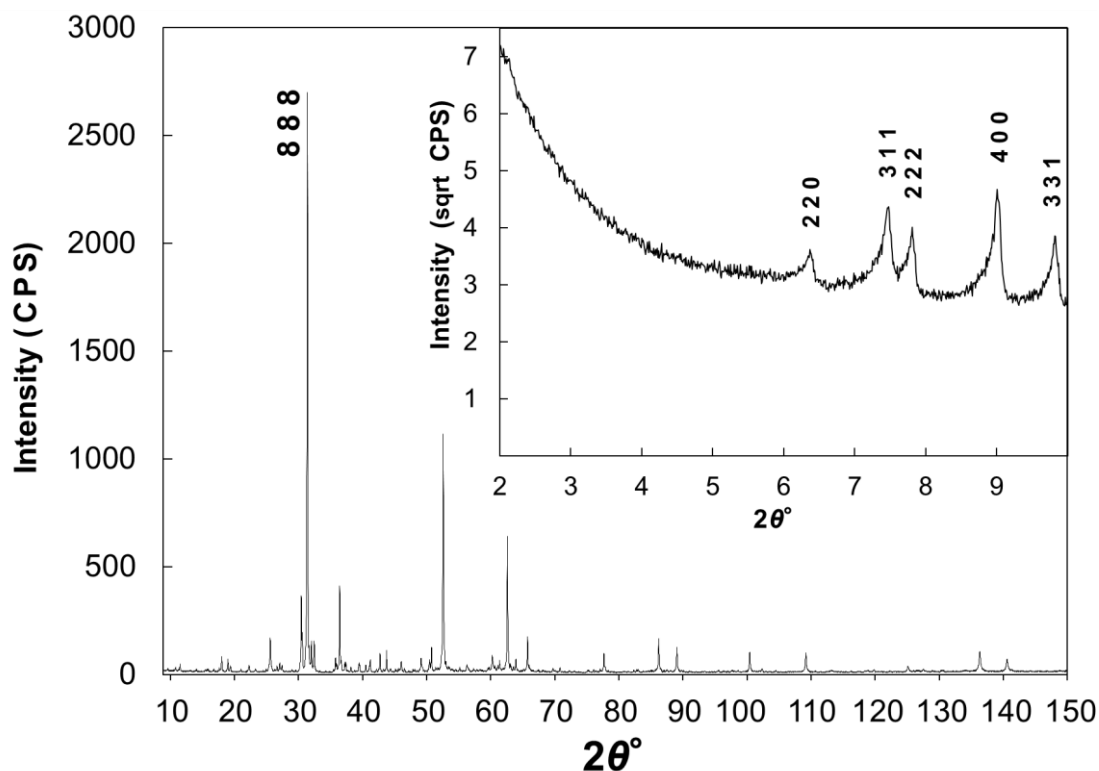


Fig. 2-16 X-ray diffraction pattern on a linear scale exemplifies how very weak are the superlattice lines, dominated by the sub-cell lines. The low angle, $2\theta = 2\text{-}10^\circ$, is shown inset on a square root scale. Advantage accrues at low angles where intensities are slightly enhanced by the $(1 + \cos 2\theta)$ term in the usual scattering equation.

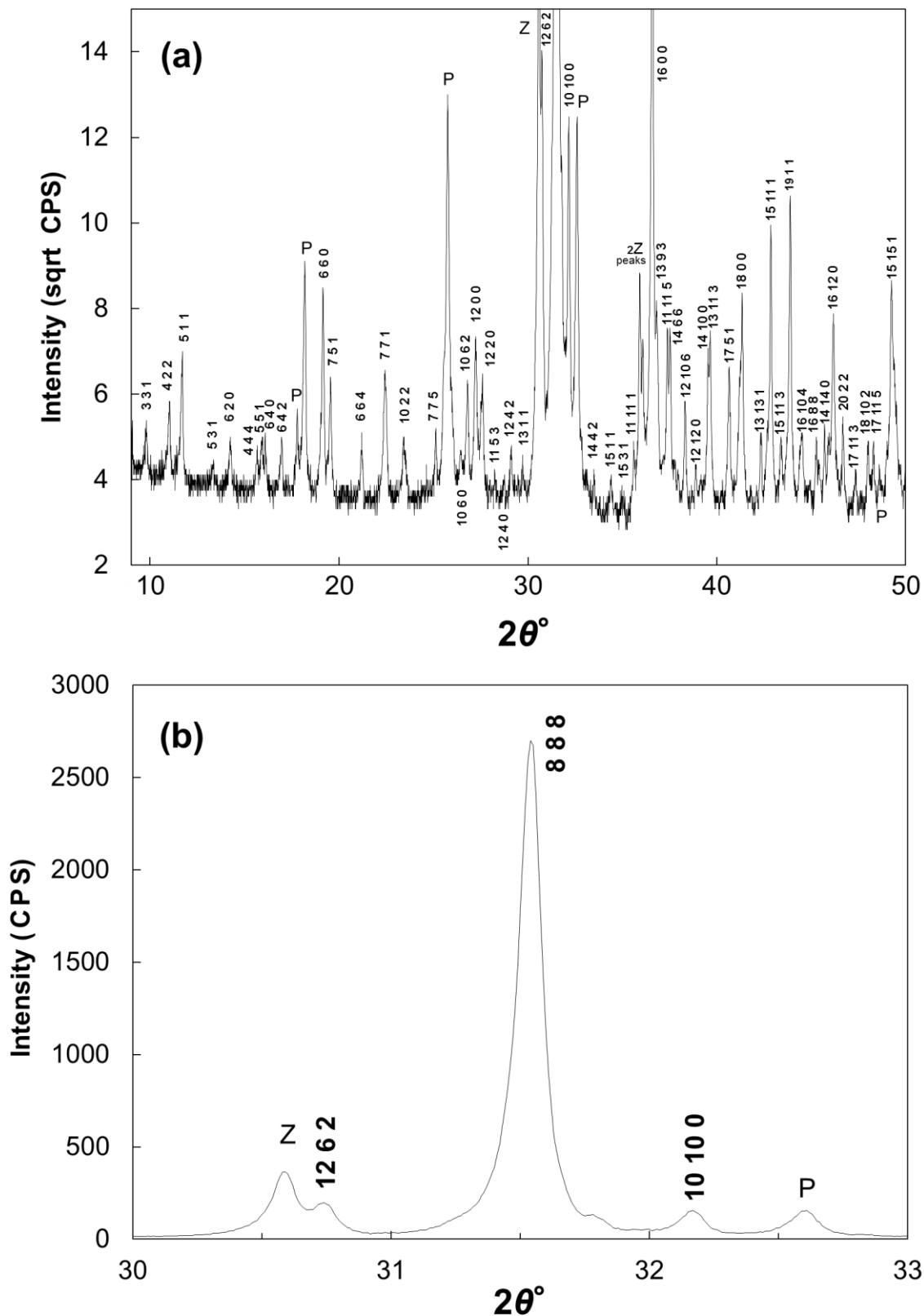


Fig. 2-17 Expanded section of Fig. 2-16. (a) Better to emphasize the many low-intensity peaks from the superlattice on a square root scale. (b) In the region of 8 8 8, all peaks are M8 with minor impurities: P, pseudobrookite and Z, zirconolite; there are no visible peaks belonging to M3 or M5.

Chapter 2

Table 2-6 Detailed list of X-ray diffraction peaks of M8 sample. There are a total of 239, mostly very weak FCC lines, from the supercell, 13 stronger FCC lines come from the fluorite-type basic sub-cell. In the case of many overlapping values of $h^2 + k^2 + l^2$, I choose, for simplicity, to show only the one with the lowest value of l (marked with the "+" symbol).

$2\theta_{\text{obs}}$	d_{obs} (Å)	I/I_0	hkl	$2\theta_{\text{calc}}$	d_{calc} (Å)	$2\theta_{\text{obs}} - 2\theta_{\text{calc}}$
6.37	13.862	4.2	2 2 0	6.36	13.884	0.01
7.48	11.811	6.0	3 1 1	7.46	11.840	0.02
7.81	11.311	5.1	2 2 2	7.79	11.336	0.02
9.01	9.807	6.9	4 0 0	9.00	9.817	0.01
9.82	9.000	4.7	3 3 1	9.81	9.009	0.01
11.01	8.029	6.6	4 2 2	11.03	8.016	-0.02
11.70	7.558	10.0	5 1 1 +	11.70	7.557	0.00
13.29	6.657	5.6	5 3 1	13.33	6.638	-0.04
14.23	6.219	7.2	6 2 0	14.25	6.209	-0.02
15.66	5.654	7.2	4 4 4	15.62	5.668	0.04
15.92	5.562	6.9	5 5 1	16.11	5.499	-0.19
16.06	5.514	7.9	6 4 0	16.26	5.446	-0.20
16.93	5.233	6.9	6 4 2	16.88	5.248	0.05
19.16	4.629	19.3	6 6 0 +	19.16	4.628	0.00
19.56	4.535	9.3	7 5 1 +	19.56	4.534	0.00
21.18	4.191	6.9	6 6 4	21.21	4.186	-0.03
22.45	3.957	12.0	7 7 1 +	22.51	3.947	-0.06
23.45	3.791	7.3	10 2 2 +	23.52	3.779	-0.07
25.09	3.546	6.9	7 7 5	25.13	3.541	-0.04
26.50	3.361	6.6	8 6 6 +	26.45	3.367	0.05
26.81	3.323	8.0	10 6 2	26.84	3.319	-0.03
27.24	3.271	10.6	12 0 0 +	27.23	3.272	0.01
27.51	3.240	9.6	11 5 1 +	27.52	3.239	-0.01
27.60	3.229	12.2	12 2 0	27.61	3.228	-0.01
28.24	3.158	5.3	11 5 3 +	28.27	3.154	-0.03
28.76	3.102	4.9	12 4 0	28.73	3.105	0.03
29.11	3.065	6.6	12 4 2 +	29.10	3.066	0.01
29.73	3.003	6.6	13 1 1 +	29.73	3.003	0.00
30.73	2.907	57.0	12 6 2	30.86	2.895	-0.13
31.54	2.834	1000.0	8 8 8 * #	31.54	2.834	0.00
32.16	2.781	41.6	10 10 0 +	32.21	2.777	-0.05
33.52	2.671	5.9	14 4 2 +	33.51	2.672	0.01
34.34	2.609	5.9	15 1 1 +	34.38	2.606	-0.04
35.03	2.559	4.9	15 3 1	35.00	2.562	0.03
35.61	2.519	8.2	11 11 1 +	35.61	2.519	0.00

Continued

Table 2-6 Continued

$2\theta_{\text{obs}}$	$d_{\text{obs}} (\text{\AA})$	I/I_0	hkl	$2\theta_{\text{calc}}$	$d_{\text{calc}} (\text{\AA})$	$2\theta_{\text{obs}} - 2\theta_{\text{calc}}$
36.58	2.455	116.0	16 0 0 *	36.58	2.454	0.00
36.82	2.439	14.0	13 9 3 +	36.80	2.440	0.02
37.38	2.404	14.0	11 11 5 #+	37.39	2.403	-0.01
37.54	2.394	14.0	14 6 6 +	37.46	2.399	0.08
37.77	2.380	6.9	16 4 4 +	37.75	2.381	0.02
37.97	2.368	5.9	15 7 1 +	37.97	2.368	0.00
38.32	2.347	7.6	12 10 6	38.32	2.347	0.00
38.86	2.316	4.3	12 12 0 +	38.89	2.314	-0.03
39.54	2.277	11.0	14 10 0 +	39.45	2.283	0.09
39.66	2.271	14.6	13 11 3 +	39.65	2.271	0.01
40.65	2.218	10.0	17 5 1 +	40.75	2.213	-0.10
41.24	2.187	10.0	17 5 3 +	41.28	2.185	-0.04
41.36	2.181	19.3	16 8 2 #+	41.35	2.182	0.01
42.08	2.146	4.3	16 8 4	42.15	2.142	-0.07
42.29	2.135	6.6	13 13 1 +	42.34	2.133	-0.05
42.67	2.117	9.2	14 12 2 +	42.67	2.117	0.00
42.86	2.108	27.6	15 11 1 #+	42.86	2.108	0.00
43.39	2.084	7.6	15 11 3 +	43.38	2.084	0.01
43.87	2.062	31.3	19 1 1 #+	43.89	2.061	-0.02
44.50	2.034	7.6	16 10 4	44.46	2.036	0.04
45.25	2.002	7.2	16 8 8	45.21	2.004	0.04
45.73	1.983	5.3	14 14 0 +	45.71	1.983	0.02
45.94	1.974	7.6	14 14 2 +	45.95	1.973	-0.01
46.17	1.965	15.0	16 12 0 +	46.20	1.963	-0.03
46.68	1.944	5.7	20 2 2 +	46.68	1.944	0.00
47.31	1.920	4.9	17 11 3 +	47.35	1.918	-0.04
48.01	1.893	7.2	18 10 2 +	47.88	1.898	0.13
48.30	1.883	6.9	17 11 5 +	48.30	1.883	0.00
48.61	1.871	4.6	20 6 2 +	48.59	1.872	0.02
49.26	1.848	21.9	15 15 1 +	49.24	1.849	0.02
49.52	1.839	9.9	16 14 2 +	49.53	1.839	-0.01
50.56	1.804	15.0	21 5 3 +	50.62	1.802	-0.06
50.90	1.793	30.9	20 8 4	50.90	1.792	-0.01
51.53	1.772	8.9	21 7 1 +	51.53	1.772	0.00
51.86	1.762	8.9	21 7 3 +	51.98	1.758	-0.12
52.46	1.743	21.0	19 11 5 +	52.42	1.744	0.04
52.71	1.735	345.7	16 16 0 *#	52.70	1.735	0.01
52.86	1.731	53.0	7 15 1 +	52.87	1.730	-0.01
53.14	1.722	12.0	18 14 0 +	53.14	1.722	0.00

Continued

Table 2-6 Continued

$2\theta_{\text{obs}}$	d_{obs} (Å)	I/I_0	hkl	$2\theta_{\text{calc}}$	d_{calc} (Å)	$2\theta_{\text{obs}} - 2\theta_{\text{calc}}$
53.35	1.716	9.6	18 14 2 +	53.36	1.716	-0.01
53.58	1.709	9.6	16 16 4 +	53.58	1.709	0.00
53.98	1.697	5.9	18 14 4 +	54.02	1.696	-0.04
54.16	1.692	6.6	23 3 1 +	54.18	1.691	-0.02
54.62	1.679	6.3	23 3 3 +	54.62	1.679	0.00
55.31	1.660	6.3	20 12 4	55.32	1.659	-0.01
56.43	1.629	9.0	20 12 6 +	56.38	1.631	0.05
56.60	1.625	7.0	22 10 0 +	56.59	1.625	0.01
57.42	1.604	8.0	20 14 2 +	57.43	1.603	-0.01
57.96	1.590	6.3	21 13 1 +	58.01	1.589	-0.05
58.44	1.578	5.9	21 13 3 +	58.42	1.578	0.02
59.68	1.548	7.7	24 8 2 +	59.71	1.547	-0.03
59.85	1.544	9.6	18 18 0 +	59.86	1.544	-0.01
60.35	1.533	23.0	20 16 0 +	60.32	1.533	0.03
60.47	1.530	16.0	23 11 3 +	60.47	1.530	0.00
60.76	1.523	7.0	18 18 4 +	60.72	1.524	0.04
61.21	1.513	9.6	25 7 1 +	61.28	1.511	-0.07
61.51	1.506	16.0	22 14 0 +	61.53	1.506	-0.02
61.71	1.502	6.6	22 14 2 +	61.73	1.502	-0.02
61.97	1.496	7.2	20 12 12	61.93	1.497	0.04
62.73	1.480	193.8	24 8 8 *	62.73	1.480	0.00
62.92	1.476	22.0	16 16 14	62.92	1.476	0.00
63.18	1.470	12.9	26 6 0 +	63.12	1.472	0.06
63.68	1.460	6.0	19 19 1 +	63.66	1.460	0.02
64.05	1.453	16.0	21 17 1 +	64.06	1.452	-0.01
65.24	1.429	7.2	23 15 1 +	65.23	1.429	0.01
65.87	1.417	48.9	16 16 16 * #	65.86	1.417	0.01
66.09	1.413	8.0	22 12 12 +	66.05	1.413	0.04
66.26	1.409	6.0	26 10 0 +	66.24	1.410	0.02
66.78	1.400	5.3	27 7 3 +	66.77	1.400	0.01
67.53	1.386	6.6	21 19 1 +	67.54	1.386	-0.01
68.31	1.372	6.6	23 17 1 +	68.30	1.372	0.01
69.10	1.358	5.3	24 16 2 +	69.10	1.358	0.00
69.83	1.346	5.3	25 15 1 +	69.81	1.346	0.02
70.19	1.340	6.3	25 15 3 +	70.19	1.340	0.00
70.94	1.327	7.3	29 5 3 +	70.93	1.328	0.00
71.33	1.321	4.9	21 21 1 +	71.31	1.322	0.02
71.68	1.316	4.9	23 19 1 +	71.68	1.316	0.00
72.33	1.305	6.6	30 2 0 +	72.28	1.306	0.05

Continued

Table 2-6 Continued

$2\theta_{\text{obs}}$	d_{obs} (Å)	I/I_0	hkl	$2\theta_{\text{calc}}$	d_{calc} (Å)	$2\theta_{\text{obs}} - 2\theta_{\text{calc}}$
73.23	1.291	5.6	21 9 1 +	73.16	1.293	0.07
73.89	1.282	4.3	25 17 5 +	73.89	1.282	0.00
75.01	1.265	4.3	29 11 1 +	74.99	1.265	0.02
75.37	1.260	6.6	23 21 1 +	75.36	1.260	0.01
76.14	1.249	6.9	25 19 1 +	76.09	1.250	0.05
76.56	1.243	5.3	28 14 4 +	76.49	1.244	0.07
76.82	1.240	4.9	27 15 7 +	76.81	1.240	0.01
77.17	1.235	8.2	29 13 1 +	77.17	1.235	0.00
77.77	1.227	25.6	32 0 0 *	77.76	1.227	0.01
77.94	1.225	11.9	28 12 10 +	77.94	1.225	0.00
78.49	1.218	5.3	28 16 0 +	78.48	1.218	0.01
78.99	1.211	4.3	31 9 3 +	78.98	1.211	0.01
79.25	1.208	3.6	28 16 4 +	79.20	1.208	0.05
79.76	1.201	3.3	22 22 10 +	79.74	1.202	0.02
80.07	1.197	3.6	25 21 3 +	80.05	1.198	0.02
80.47	1.193	3.3	31 11 1 +	80.41	1.193	0.06
80.94	1.187	4.6	30 14 0 +	80.99	1.186	-0.05
81.54	1.180	4.0	30 12 8 +	81.53	1.180	0.01
81.73	1.177	3.0	28 18 2 +	81.70	1.178	0.03
82.42	1.169	4.6	32 10 2 +	82.42	1.169	0.00
82.90	1.164	5.6	33 7 1 +	82.91	1.164	-0.01
83.10	1.161	5.9	28 18 6 +	83.13	1.161	-0.03
83.91	1.152	3.6	25 23 3 +	83.97	1.152	-0.06
84.72	1.143	4.6	27 21 3 +	84.68	1.144	0.04
85.10	1.139	4.6	28 20 2 +	85.08	1.139	0.02
85.41	1.136	4.9	31 15 3 +	85.39	1.136	0.02
85.84	1.131	5.9	32 12 6 +	85.79	1.132	0.05
86.32	1.126	59.8	24 24 8 *	86.32	1.126	0.00
87.12	1.118	5.3	35 3 1 +	87.16	1.117	-0.04
87.54	1.114	6.9	35 3 3 +	87.51	1.114	0.03
88.25	1.106	4.6	34 10 2 +	88.26	1.106	-0.01
89.15	1.098	33.2	32 16 0 *	89.14	1.098	0.01
89.86	1.091	6.9	36 0 0 +	89.85	1.091	0.01
90.16	1.0878	5.6	30 20 2 +	90.20	1.0875	-0.04
90.69	1.0829	5.3	33 15 1 +	90.68	1.0829	0.01
91.02	1.0798	4.9	31 19 1 +	91.04	1.0796	-0.02
91.46	1.0757	5.3	28 22 8 +	91.43	1.0760	0.03
91.84	1.0723	4.6	33 15 5 +	91.74	1.0732	0.10
92.46	1.0667	5.3	27 25 1 +	92.45	1.0668	0.01

Continued

Table 2-6 Continued

$2\theta_{\text{obs}}$	d_{obs} (Å)	I/I_0	hkl	$2\theta_{\text{calc}}$	d_{calc} (Å)	$2\theta_{\text{obs}} - 2\theta_{\text{calc}}$
93.12	1.0609	5.6	29 23 1 +	93.15	1.0606	-0.03
93.58	1.0569	5.9	32 16 10 +	93.55	1.0571	0.03
93.81	1.0549	4.6	33 17 3 +	93.86	1.0544	-0.05
94.33	1.0504	4.6	36 10 2 +	94.44	1.0495	-0.11
94.55	1.0486	4.9	31 21 1 +	94.57	1.0484	-0.02
94.97	1.0450	5.6	36 10 4 +	94.97	1.0451	0.00
95.25	1.0427	5.3	37 7 1 +	95.28	1.0425	-0.03
95.69	1.0391	5.9	32 20 2 +	95.68	1.0392	0.01
96.43	1.0331	6.3	36 12 2 +	96.39	1.0334	0.04
97.17	1.0271	5.6	32 20 6 +	97.10	1.0277	0.07
97.75	1.0226	6.3	29 25 3 +	97.76	1.0225	-0.01
98.15	1.0195	5.9	34 18 2 +	98.16	1.0194	-0.01
98.67	1.0155	5.9	36 14 2 +	98.70	1.0153	-0.03
99.48	1.0094	5.3	35 17 1 +	99.55	1.0089	-0.07
99.92	1.0061	5.3	39 1 1 +	99.90	1.0063	0.02
100.49	1.0020	28.3	32 16 16 *	100.49	1.0020	0.00
100.87	0.9992	7.9	38 10 0 +	100.85	0.9994	0.02
101.14	0.9973	5.6	36 16 0 +	101.21	0.9968	-0.07
101.33	0.9959	6.3	33 21 5	101.34	0.9958	-0.01
102.43	0.9882	8.6	29 27 3 +	102.42	0.9882	0.01
103.13	0.9834	5.3	37 15 1 +	103.14	0.9833	-0.01
103.53	0.9807	4.9	32 24 2 +	103.55	0.9805	-0.02
103.74	0.9793	4.9	40 2 2 +	103.73	0.9793	0.01
104.20	0.9762	4.6	33 23 1 +	104.23	0.9760	-0.03
104.61	0.9735	6.3	33 23 3 +	104.60	0.9736	0.01
105.39	0.9684	4.6	34 22 2 +	105.37	0.9685	0.02
106.09	0.9639	4.9	37 17 1 +	106.06	0.9641	0.03
106.57	0.9609	5.6	40 8 2 +	106.47	0.9615	0.10
106.89	0.9589	5.6	38 14 6 +	106.84	0.9592	0.05
107.22	0.9569	5.3	36 18 8 +	107.21	0.9569	0.01
107.49	0.9552	5.6	31 27 1 +	107.53	0.9550	-0.04
108.23	0.9508	4.9	41 5 1 +	108.28	0.9505	-0.05
109.25	0.9447	25.9	40 8 8 *+	109.25	0.9447	0.00
109.67	0.9423	8.9	34 24 2 +	109.63	0.9425	0.04
110.48	0.9376	5.6	35 23 1 +	110.52	0.9374	-0.04
110.74	0.9361	5.9	40 12 4 +	110.76	0.9361	-0.02
110.99	0.9347	4.6	38 16 8 +	110.94	0.9350	0.05
111.26	0.9332	4.9	39 15 5 +	111.28	0.9331	-0.02
111.57	0.9315	4.3	35 23 5 +	111.65	0.9310	-0.08

Continued

Table 2-6 Continued

$2\theta_{\text{obs}}$	d_{obs} (Å)	I/I_0	hkl	$2\theta_{\text{calc}}$	d_{calc} (Å)	$2\theta_{\text{obs}} - 2\theta_{\text{calc}}$
112.30	0.9275	4.6	39 15 7 +	112.42	0.9269	-0.12
112.48	0.9265	4.6	36 22 4 +	112.46	0.9266	0.02
112.67	0.9255	5.3	30 30 0 +	112.65	0.9256	0.02
113.21	0.9226	6.3	32 28 2 +	113.23	0.9225	-0.02
113.43	0.9215	6.3	30 30 4 +	113.42	0.9215	0.01
113.95	0.9187	4.9	33 27 3 +	113.95	0.9187	0.00
114.30	0.9169	5.6	37 21 5 +	114.34	0.9167	-0.04
114.86	0.9140	4.6	42 8 4 +	114.77	0.9145	0.09
115.09	0.9129	4.3	35 25 1 +	115.11	0.9128	-0.02
115.47	0.9110	4.3	43 3 1 +	115.50	0.9108	-0.03
116.31	0.9068	5.6	43 5 1 +	116.29	0.9069	0.02
118.52	0.8962	5.9	40 16 8	118.52	0.8962	0.00
118.92	0.8944	5.9	38 22 0 +	118.93	0.8943	-0.01
119.92	0.8898	7.2	31 31 5 +	119.89	0.8900	0.03
120.36	0.8879	5.6	44 4 2 +	120.35	0.8879	0.01
120.52	0.8871	4.9	42 14 0 +	120.55	0.8870	-0.03
120.91	0.8854	4.9	44 4 4 +	120.96	0.8852	-0.05
121.13	0.8845	4.9	39 21 3 +	121.11	0.8845	0.02
122.36	0.8792	5.3	37 25 1 +	122.36	0.8792	0.00
122.81	0.8773	4.9	40 20 2 +	122.83	0.8772	-0.02
125.20	0.8676	11.0	32 32 0 *	125.17	0.8677	0.03
125.75	0.8655	5.9	33 31 3 +	125.77	0.8654	-0.02
126.47	0.8627	5.9	34 30 4 +	126.48	0.8627	-0.01
126.81	0.8614	6.6	36 28 0 +	126.92	0.8610	-0.11
127.52	0.8588	7.6	35 29 5 +	127.52	0.8588	0.00
128.40	0.8556	5.6	37 27 3 +	128.42	0.8555	-0.02
129.11	0.8530	5.6	38 26 0 +	129.15	0.8529	-0.04
130.64	0.8477	5.3	39 25 1 +	130.71	0.8475	-0.07
131.36	0.8453	5.3	38 26 6 +	131.23	0.8457	0.13
132.23	0.8424	4.6	39 25 5 +	132.12	0.8428	0.11
132.63	0.8411	5.6	40 24 2 +	132.66	0.8411	-0.03
133.99	0.8368	5.9	33 33 5	134.05	0.8367	-0.06
136.37	0.8297	29.9	40 24 8 *	136.37	0.8297	0.00
137.07	0.8277	7.9	39 27 1 +	137.07	0.8277	0.00
138.79	0.8229	4.6	40 24 10 +	138.72	0.8231	0.07
139.84	0.8201	5.6	40 26 4 +	139.80	0.8203	0.04
140.61	0.8182	16.3	48 0 0 *+	140.63	0.8181	-0.02
141.38	0.8162	6.6	35 33 1 +	141.40	0.8162	-0.02
141.46	0.8160	7.6	34 34 2 +	141.47	0.8160	-0.01

Continued

Table 2-6 Continued

$2\theta_{\text{obs}}$	d_{obs} (Å)	I/I_0	hkl	$2\theta_{\text{calc}}$	d_{calc} (Å)	$2\theta_{\text{obs}} - 2\theta_{\text{calc}}$
142.25	0.8141	4.9	34 34 4 +	142.32	0.8139	-0.07
142.44	0.8136	4.9	37 31 1 +	142.54	0.8134	-0.10
144.25	0.8094	4.9	37 31 5 +	144.32	0.8092	-0.07
144.98	0.8077	4.6	39 29 1 +	144.93	0.8078	0.05
146.28	0.8049	4.9	38 30 6 +	146.25	0.8050	0.03
146.79	0.8038	4.9	39 29 5 +	146.81	0.8038	-0.02
148.30	0.8007	5.3	36 28 18	148.21	0.8009	0.09
148.75	0.7999	5.9	39 29 7 +	148.80	0.7998	-0.05
149.64	0.7981	5.6	40 28 6 +	149.57	0.7983	0.07

*13 stronger FCC lines come from the fluorite type basic sub-cell.

Several of the stronger lines agree with all the indexing of stronger spots in the SAED patterns [14].

2.4.6 Confirmation for space group using synchrotron X-ray diffraction

In above sections, I illustrated how, for a PXRD pattern of a complex very large FCC unit cell ($a = 39.277(3)$ Å) oxide, M8, it would become mandatory to investigate weak, low angle 2θ lines (around/less-than 2% of the maximum intensity line) thus, provisionally assigning a SG. Originally, we did this with ordinary, but profligate, long scans on a typical laboratory X-ray unit. The result implied that this improvement in data could only come from an intense X-ray source such as a synchrotron, as very well described in [25] and citations therein to earlier papers; here I present the efficacious result from a synchrotron, with my earlier postulated SG confirmed.

The complete synchrotron X-ray diffraction pattern, showing all the peak tops, is as in Fig. 2-18. An accurate beam wavelength of 0.9997 Å was measured using a CeO₂ standard sample under the same conditions. The strongest peak is the sub-cell 888 peak with a peak height ~170,000 counts/sec, which is ~62 times higher and more monochromatic than that from a typical laboratory X-ray source. The strong peaks are from $8 \times (hkl)$ of the FCC sub-cell. It also firmly establishes a very large FCC unit-cell, $a = 39.277$ Å, as for the previous work.

To be certain of the SG, I need to be sure of the hkl of the extremely weak supercell peaks at the low angles - these peaks are only <2,000 counts/second - and are shown expanded in Figs. 2-19, the supplemental material for the whole 2θ range is as in Figs. A1-1 (Appendix 1). There are no visible lines belonging to other members of murataite family, e.g. M7, M5 or M3; viz. no coherent intergrowths, which leads to a singular sharp 888 peak.

Contrasting with the conventional lab. PXRD technique, a very weak 111 line might be present. With the synchrotron capability, the peaks are extremely sharp and highly resolved, which greatly benefits any indexing especially at increasing 2θ . I definitely note that, for $hk0$ $h + k = 4n$ only; especially noticeable is the absence of 200, and true at all the higher angles as well; thus the SG differs from the previously proposed $F\bar{4}3m$ (216) by Pakhomova *et al.* [26]. Due to the immense size of this unit cell (I believe the largest volume unit-cell oxide ever studied) such small differing opinions are not surprising.

Now three possible SGs, $Fd\bar{3}$ (203), $Fd\bar{3}m$ (227) and $Fd\bar{3}c$ (228) are allowed; of these $Fd\bar{3}m$ (227) is the

most likely based on statistical analysis of the structural database (ICSD-2002 and -2006) by Urusov and Nadezhina [27]. Its frequency of occurrence in compounds of inorganic materials is the most common of the three SGs, 5.1%, and four times higher than that of the formerly proposed $F\bar{4}3m$ (216), 1.2%. The SGs $Fd\bar{3}$ (203) and $Fd3c$ (228) have maybe a very low or zero frequency of occurrence in inorganic crystal chemistry.

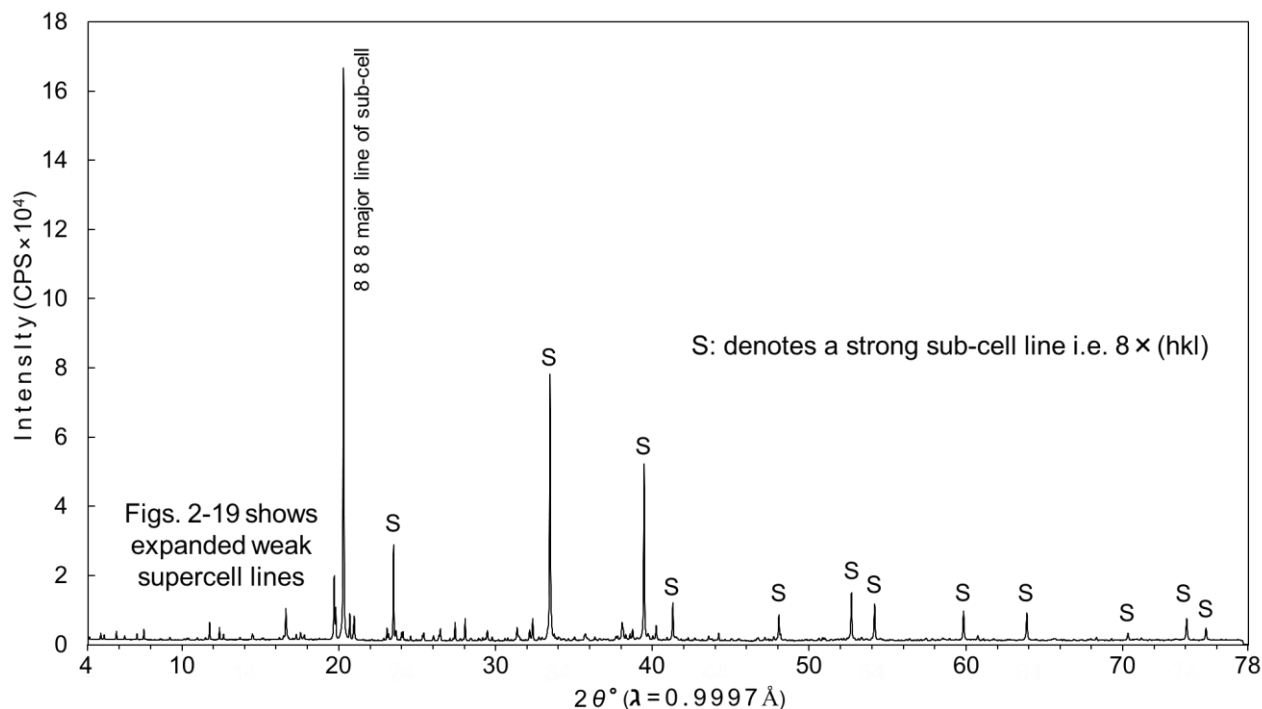
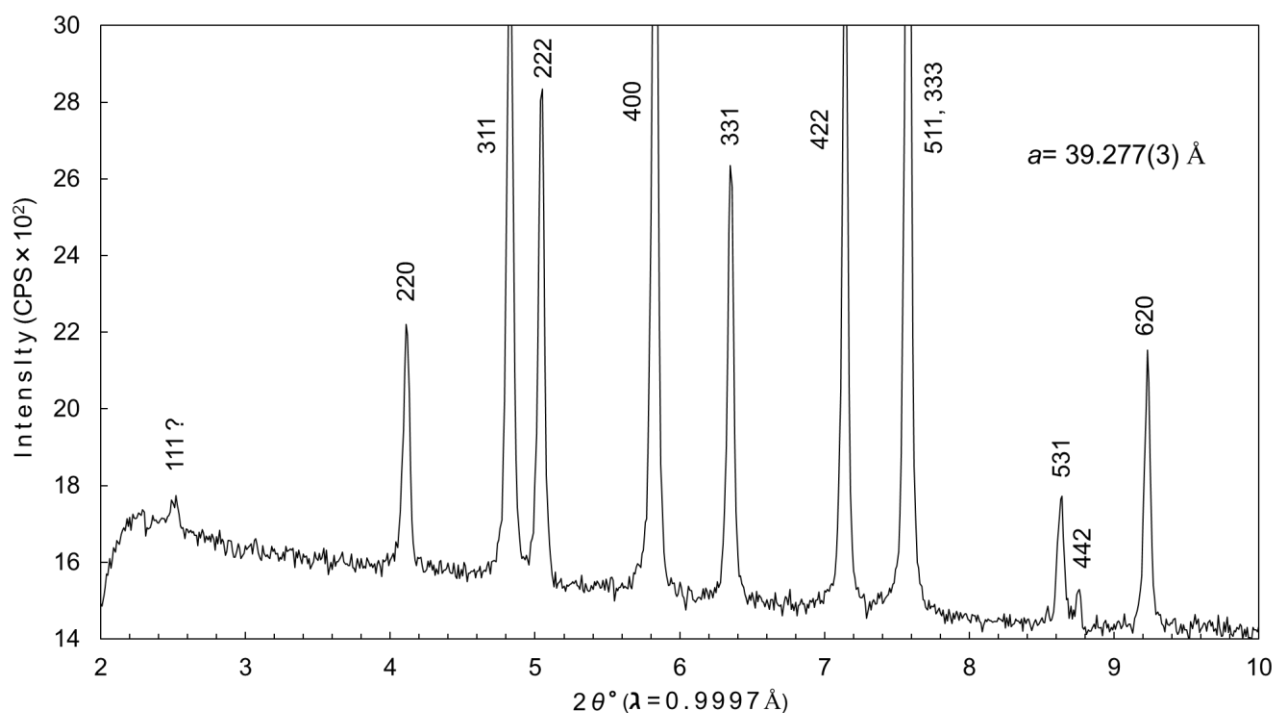


Fig. 2-18 Complete synchrotron X-ray diffraction pattern of M8-murataite on a linear scale.



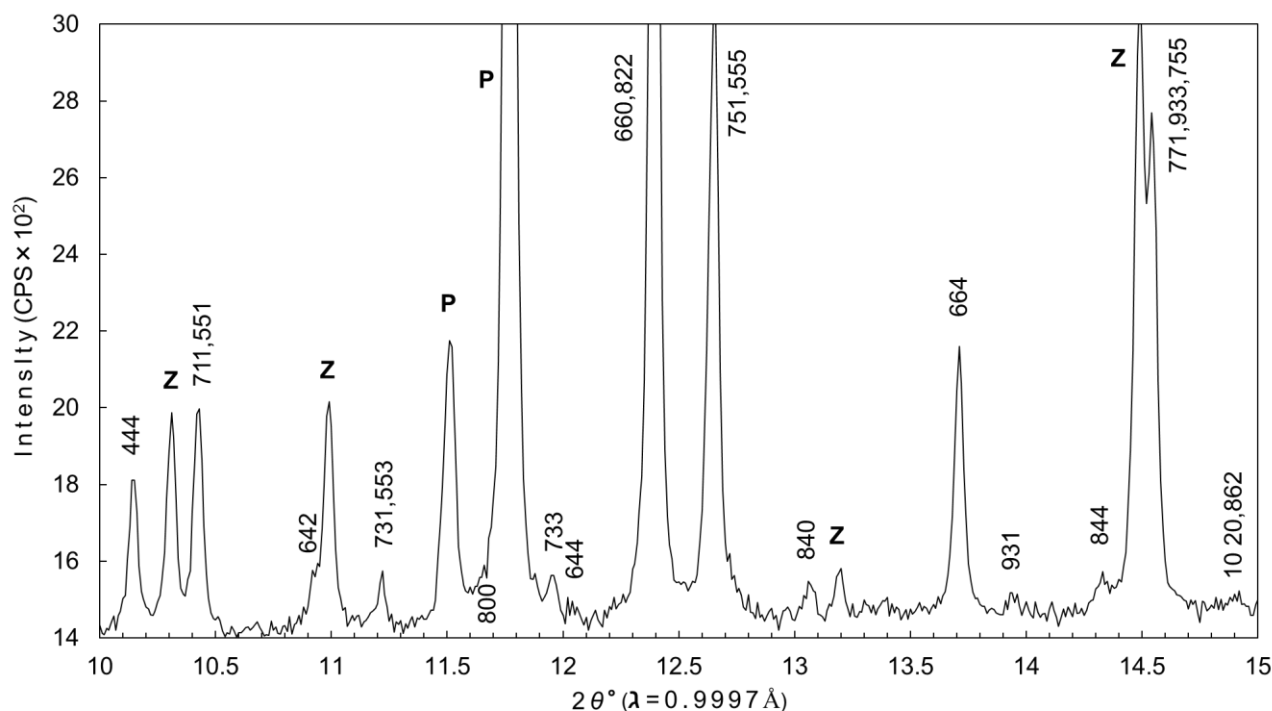


Fig. 2-19 Expanded synchrotron X-ray diffraction pattern of the all-important low 2θ section of M8, with slight impurities: P, pseudobrookite [PDF 00-041-1432 (ICDD, 1991) and Z, zirconolite [PDF 00-034-0167 (ICDD, 1984)].

2.5 Discussion

2.5.1 Comparison between microstructure of murataite series synthesized by solid-state and melting

Many reports on the crystal structural analysis for M3 by XRD technique reported good agreement with the data of elemental analysis by the electron microprobe analysis, which is generally micro scale analysis. The determination of the chemical formula by XRD, however, is strongly responsible for the diffraction intensity, and ordinary diffraction techniques do not take into account the localization of Zr ions with enormous periodicity as confirmed in section 2.4.3-2.4.4. Therefore, there might be structural analysis mistakes caused by this huge defect. In addition to this, the element mapping by STEM-EELS demonstrated that Zr ion seems to be present in the same column as Ca and Mn, thus further investigations about the site preference of Zr ion should be done.

The design and control of the microstructure at the atomic scale, such as defect structure, for the physical properties of inorganic materials have been actively researched and developed, but considered to be not easy work. It is noteworthy that the murataite ceramics, as shown here, with enormous superstructure and defect produced spontaneously is very rare case in inorganic field. Since similar defect was observed also in M8-type murataite, it seems to be a very important task for widening (discussing) the possible application of this unique structure. Furthermore, it is predicted that these findings of site preference and huge defect will develop the study on the SYNROC technique as well because actinides are appeared to be placed at same site of Zr ion in murataite polysomatic series.

2.5.2 Important approach for quick/speedy monitoring of families of very complex polytypes

There is considerable risk when not observing possible low-angle very weak peaks, especially as I move to these more complex materials. One particularly “good” example hampered the (maybe overspecialized) applied luminescent/ fluorescent community; these researchers published well over 70 papers that maintained that YBO_3 , and its isotopes, were “vaterites” (isotypic with a form of CaCO_3) and/or had hexagonal symmetry – this was actually the strong basic sub-cell with B hardly contributing to the intensities. Low-angle very weak peaks would have revealed the larger monoclinic two-layer pseudowollastonite cell, isotypic with CaSiO_3 (pseudowollastonites are notorious for having polytypic complexity [28-29]); un-awareness of the true unit cells, or intergrowths thereof, quite possibly might partly explain some variable luminescence results. Single-crystal work was necessary, coming to the rescue [30-31] even though the powder technique had, indeed, much earlier flagged the problem [28]. Although Lin *et al.* identified the correct monoclinic cell, they were unaware that it is a known pseudowollastonite type.

For routine “fingerprinting”, slow scans only from $\sim 2^\circ$ to $15\text{-}20^\circ$ may be sufficient. Higher intensity sources would be beneficial, but may not be available on a day-to-day basis. A rotating stage would also help as so many planes must orient in the diffraction mode.

This approach should be applied to M5 and M7 (M3 already done) so as to provide the engineering synthesizer a speedier monitoring to gauge progress in his/her efforts with so many possible cations. Likely other families of very complex polytypes may be discovered more quickly as ceramics style efforts pursue evermore complex cationic mixes for novel/exotic physical properties.

2.5.3 The deference of SG from that already proposed in previous works

As one suggestion, the difference of SG from that proposed by Laverov and Pakhomova [14,26] could be considered as follows. In the fluorite-type structure, the structural symmetry enhanced from monoclinic to cubic with continually increasing temperature; in other words, phase transition from low temperature phase to high temperature phase. It is indicated that the difference of the SG confirmed as $F4\bar{3}m$ (216) in earlier work using melting method and as $Fd\bar{3}$ (203), $Fd\bar{3}m$ (227) and $Fd3c$ (228) in this work using solid-state synthesis (probably partially melting) might be due to the synthesis conditions and formation temperature of M8.

2.6 Conclusions

The synthesis of murataite series, M3 and M8, were carried out by solid-state reaction without actinide and REE. A single superstructure of M8 was successfully fabricated. HAADF-STEM observation and element mapping with EELS demonstrated a layered defect having a periodicity much larger than the lattice constant and localization of Zr ion. Moreover, Zr ion may place on the same column as the Ca and Mn with 8 coordination in STEM-EELS images, which is different from the result of structural analysis for M3 previously reported. These findings indicated that further careful investigations for the structural analysis of murataite series should be done.

As for the PXRD characterization of the large-volume unit cell of the M8 murataite polytype, conclusions

Chapter 2

are summarized as follows;

- (1) M8 has been synthesized remarkably pure by the simple standard ceramic procedure of co-firing oxides. Its conventional lab. PXRD contains more than the 239 surely identified lines.
- (2) The M8 superstructure was first observed by TEM–SAED enabling the analysis by the powder method with some confidence. The calculated lattice constant, a , of this M8 superstructure is 39.269(1) Å; it is most likely the largest inorganic mixed-oxide unit cell ever studied by somewhat conventional powder diffraction.
- (3) The existence of only $h k 0$ peaks, where $h + k = 4n$, as confirmed by synchrotron data, suggests that M8 most likely belongs to the $Fd\bar{3}m$ (227) SG, contrasting with the previously proposed $F4\bar{3}m$ (216). Synchrotron methods are the most accurate and probably necessary from now on in this area.

Supplemental materials

To view supplementary material for the all x-ray diffraction pattern data of the large-volume unit cell of the M8 murataite polytype, please visit <http://dx.doi.org/10.1017/S0885715615000913> [32].

References

- [1] V. S. Urusov, N. I. Organova, O. V. Karimova, S. V. Yudintsev, and R. C. Ewing, "A modular model of the pyrochlore-murataite polysomatic series," *Crystallogr. Rep.*, **52** [1] 37-46 (2007).
- [2] J. W. Adams, T. Botinelly, W. N. Sharp, and K. Robinson, "Murataite, a new complex oxide from El Paso County, Colorado," *Am. Mineral.*, **59** [1-2] 172-176 (1974).
- [3] P. E. D. Morgan and F. J. Ryerson, "A new "cubic" crystal compound," *J. Mater. Sci. Lett.*, **1** [8] 351-352(1982).
- [4] P. E. D. Morgan, A. B. Harker, and J. F. Flintoff, "Developments in SRP "composite" defense ceramic radwaste forms," in: G. G. Wicks, W. A. Ross (Eds.), *Nuclear Waste Management*, Am. Ceram. Soc., Columbus, OH, 1984, pp. 234-246.
- [5] A. S. Pakhomova, S. V. Krivovichev, S. V. Yudintsev, and S. V. Stefanovskii, "Synthetic murataite-3C, a complex form for long-term immobilization of nuclear waste: crystal structure and its comparison with natural analogues," *Z. Kristallogr.*, **228** [3] 151-156 (2013).
- [6] N. P. Laverov, S. V. Yudintsev, B. I. Omel'yanenko, B. S. Nikonov, and S. V. Stefanovskii, "Murataite ceramics for the immobilization of actinides," *Geol. Ore Deposits*, **41** [2] 85-93 (1999).
- [7] B. M. Gatehouse, L. N. Grey, J. F. Lovering, and D. A. Wark, "Structure studies on tranquillityite and related synthetic phases," *Proc. Lunar. Sci. Conf.*, **2** 1831-1838 (1977).
- [8] R. E. Morris, J. J. Owen, J. K. Stalick, and A. K. Cheetham, "Determination of complex structures from powder diffraction data: The crystal structure of $\text{La}_3\text{Ti}_5\text{Al}_{15}\text{O}_{37}$," *J. Solid State Chem.*, **111** [1] 52-57 (1994).
- [9] P. E. D. Morgan, "Preparing new extremely difficult-to-form crystal structures," *Mater. Res. Bull.*, **19** [3] 369-376 (1984).
- [10] M. Strunk and V. Müller-Buschbaum, "Zur kristallstruktur von $\text{SrAl}_8\text{Ti}_3\text{O}_{19}$," *J. Alloy Compd.*, **198** [1-2] 101-104 (1993).
- [11] M. Kasunič, A. Meden, S. D. Škapin, D. Suvorov, and A. Golobič, "Structure of $\text{LaTi}_2\text{Al}_9\text{O}_{19}$ and reanalysis of the crystal structure of $\text{La}_3\text{Ti}_5\text{Al}_{15}\text{O}_{37}$," *Acta Crystallogr. B*, **67** 455-460 (2011).
- [12] A. Aliev, V. M. Kovrugin, M. Colmont, C. Terryn, M. Huve, O. I. Siidra, S. V. Krivovichev, and O. Mentre, "Revised bismuth chloroselenite system: evidence of a non-centrosymmetric structure with a giant unit cell," *Cryst. Growth Des.*, **14** [6] 3026-3034 (2014).
- [13] N. P. Laverov, S. V. Yudintsev, S. V. Stefanovskii, B. I. Omel'yanenko, and B. S. Nikonov, "Murataite as a universal matrix for immobilization of actinides," *Geol. Ore Deposits*, **48** [1] 335-356 (2006).
- [14] N. P. Laverov, V. S. Urusov, S. V. Krivovichev, A. S. Pakhomova, S. V. Stefanovsky, and S. V. Yudintsev, "Modular nature of the polysomatic pyrochlore-murataite series," *Geol. Ore Deposits*, **53** [4] 273-294 (2011).
- [15] T. S. Ercit and F. C. Hawthorne, "Murataite, a UB_{12} derivative structure with condensed Keggin molecules," *Can. Mineral.*, **33** [1] 1223-1229 (1995).
- [16] N. P. Laverov, S. V. Yudintsev, S. V. Stefanovskii, B. I. Omel'yanenko, and B. S. Nikonov, "Murataite matrices for actinide wastes," *Radiochemistry*, **53** [3] 229-243 (2011).
- [17] M. N. Rahaman, "Ceramic Processing and Sintering," Marcel Dekker, Inc., New York, USA, 2003.
- [18] C. C. Barry, N. M. Grant, "Ceramic Materials: Science and Engineering," Springer Science and Business Media New York, New York, USA, 2013.
- [19] P. C. Angelo, R. Subramanian, "Powder metallurgy: Science, Technology and Applications," PHI

Chapter 2

Learning Pvt. Ltd., New Delhi, India, 2008.

- [20] R. L. Coble, "Sintering crystalline solids. I. intermediate and final state diffusion models," *J. Appl. Phys.*, **32** [5] 787-792 (1961).
- [21] R. L. Coble, "Sintering crystalline solids. II. experimental test of diffusion models in powder compacts," *J. Appl. Phys.*, **32** [5] 793-799 (1961).
- [22] S. -J. L. Kang, "Sintering - densification, grain growth, and microstructure," Elsevier, Oxford, 2005.
- [23] F. J. Ryerson, "Phase equilibria of nuclear waste ceramics: The effect of oxygen fugacity," *J. Am. Ceram. Soc.*, **67** [2] 75-82 (1984).
- [24] B. B. V. Aken, A. Meetsma, and T. T. M. Pastra, "Hexagonal YbMnO₃ revisited," *Acta Cryst.*, **57** [3] i87-i89 (2001).
- [25] A. Boultif and D. Louër, "Powder pattern indexing with the dichotomy method," *J. Appl. Crystallogr.*, **37** [5] 724-731 (2004).
- [26] A. S. Pakhomova, S. V. Krivovichev, S. V. Yudintsev, and S. V. Stefanovsky, "Polysomatism and structural complexity: Structure model for murataite-8C, a complex crystalline matrix for the immobilization of high-level radioactive waste," *Eur. J. Mineral.*, **28** [1] 205-214 (2016).
- [27] V. S. Urusov and T. N. Nadezhina, "Frequency Distribution and Selection of Space Groups in Inorganic Crystal Chemistry," *J. Struct. Chem.*, **50** [1] 22-37 (2009).
- [28] P. E. D. Morgan, P. J. Carrol, and F. F. Lange, "Crystal structure of YSiO₂N and a reappraisal of the "vaterite" type, YBO₃," *Mater. Res. Bull.*, **12** [3] 251-260 (1977).
- [29] H. Yang and C. T. Prewitt "On the crystal structure of pseudowollastonite (CaSiO₃)," *Am. Mineral.*, **84** [5-6] 929-932 (1999).
- [30] J. Lin, D. Sheptyakov, Y. Wang, and P. Allenspach, "Structures and phase transition of vaterite-type rare earth orthoborates: A neutron diffraction study," *Chem. Mater.*, **16** [12] 2418-2424 (2004).
- [31] A. Pitscheider, R. Kaindl, O. Oeckler, and H. Huppertz, "The crystal structure of π -EuBO₃: New single-crystal data for an old problem," *J. Solid State Chem.*, **184** [1] 149-153 (2011).
- [32] R. S. S. Maki, P. E. D. Morgan, and Y. Suzuki, "X-ray powder diffraction characterization of the large volume unit-cell of the M8 murataite polytype," *Powder Diffr.*, **31** [1] 8-15 (2016).

Chapter 3

Synthesis and Characterization of a Simpler Mn-free, Fe-rich M3-type Murataite

Chapter 3: Synthesis and Characterization of a Simpler Mn-free, Fe-rich M3-type Murataite

I report here the first finding of a Mn-free, Fe-rich M3-type murataite by solid-state reaction. While formerly this family of polytypes were classified as titanates, now I have added high iron members, *i.e.* Fe plays a defining role in the new M3s with no Mn. XRD patterns and SEM-EDS reveal that the samples in the system of Ca-Ti-Zr-Al-Fe-O and Ca-Mn-Ti-Zr-Al-Fe-O consist of three-fold fluorite-type FCC superstructures, which now only have 5 cations, Ca, Ti, Zr, Al, and Fe; this will necessarily simplify structural investigations of these complex synthetic versions of the murataite-pyrochlore polysomatic series.

3.1 Introduction

Natural mineral murataite is very rare [1], being somewhat like pyrochlore, but having a three-fold fluorite-related sub-cell instead of pyrochlore's two-fold one. The closely related synthetic versions, however containing very different elements, have a similar three-fold fluorite-type FCC superstructure, denoted M3; they are very promising as future crystalline radioactive waste host materials [2,3]. Actinide elements, such as Pu and U, which are in high-level radioactive waste (HLW), can occupy specific sites in the crystal structure of the murataite as major constituent elements [4]. Murataite has long-term stability and low leachability for immobilization of actinide wastes compared to other solidification methods, *e.g.* borosilicate glass.

Synthetic murataite is believed to contain five systematically independent cation sites instead of only four positions in natural murataite (space group believed to be: $F\bar{4}3m$) [5]. Here I begin the study of a new/simpler M3, synthesized with only five cations, instead of the previously synthesized ones containing six or more. The impetus for this is that *e.g.* difficult Rietveld refinements, are simplified and the chance of getting a more exact correct crystal structure is enhanced for this large FCC unit cell of $a = \sim 14.56 \text{ \AA}$.

Several other synthetic varieties of the murataite-pyrochlore polysomatic series with $5 \times 5 \times 5$, M5, $7 \times 7 \times 7$, M7 and $8 \times 8 \times 8$, M8 fluorite-type superstructures have been discovered [6-8]. These polysomatic varieties were mainly achieved by melt methods which usually produces crystals with complicating zoning of mixed types. These synthetic murataites can contain transition and rare earth cations (the clue to their ability also to contain actinides), *e.g.* as formally $^{[8]}Ca_6^{[8]}Ca_4^{[6]}Ti_{12}^{[5]}Ti_4^{[4]}AlO_{42}$, where $Ca = Ca, Mn, REE$; $Ti = Ti, Zr, Al$; $Al = Al, Fe$ in synthetic M3 (Fig. 3-1 illustrated by VESTA [9]). The synthetic M3 is presently believed to contain five symmetrically independent cation positions, while natural murataite contains only four cation positions. Ca2 is the additional site coordinated by eight oxygen ions, and cation substitution can typically occur at each cation site [10]. This complexity makes the structural analyses of murataites quite challenging.

As is previously supposed, and Russian workers (*e.g.* Sergey V. Yudintsev - private communication) tentatively agreed, that Mn may be required to promote the crystal structures of the murataite series. However, as here, I recently produced an M3 murataite phase which does not contain Mn. The new M3, which "only" has Ca, Ti, Zr, Al, and more Fe than formerly, should greatly simplify and aid our structural investigations.

Additionally, several major differences between the results of solid-state synthesis, as here, and the earlier melting method are noted.

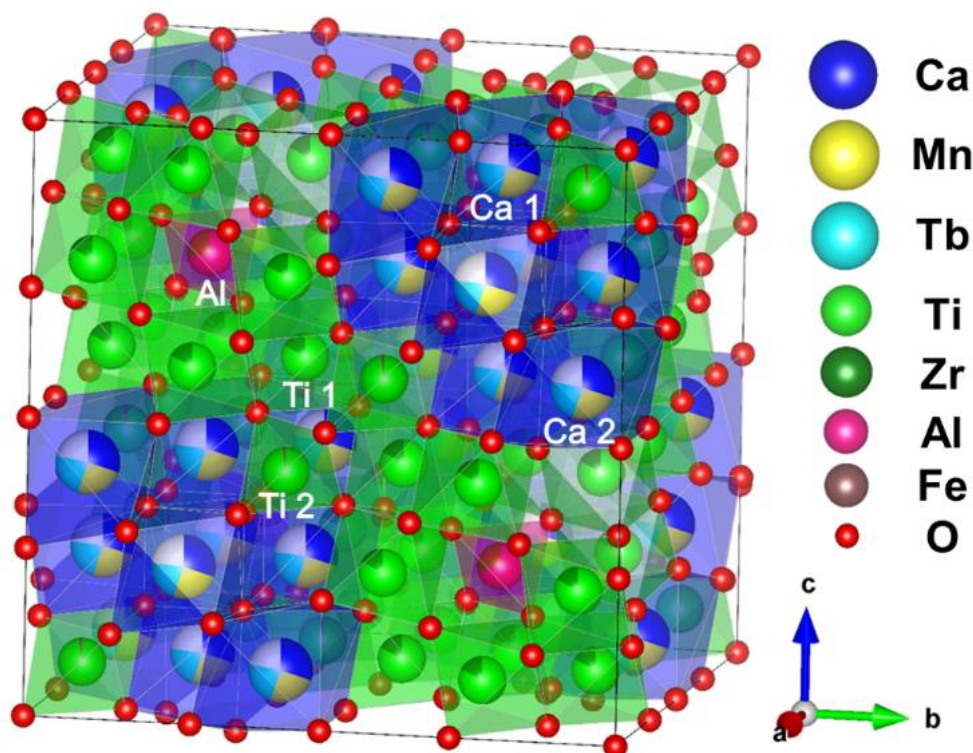


Fig. 3-1 Crystal structure of M3 containing five symmetrically independent cation positions: Ca1, Ca2, Ti1, Ti2 and Al site [10]. The [8]-coordinated, [6, 5]-coordinated and [4]-coordinated polyhedrons are colored to blue, green and red, respectively (illustrated by VESTA [9]).

3.2 Experimental procedure

3.2.1 Sample preparation

Commercial CaO (99.9% purity, Kojundo Chemical Laboratory Co. Ltd.), MnO₂ (99% purity, Kojundo Chemical Laboratory Co. Ltd.), TiO₂ anatase (99% purity, Kojundo Chemical Laboratory Co. Ltd.), ZrO₂ (98% purity, Kojundo Chemical Laboratory Co. Ltd.), α -Al₂O₃ (99.99% purity, Taimei Chemicals Co. Ltd., Saitama, Japan) and α -Fe₂O₃ (99.9% purity, Wako Pure Chemical Industries Ltd.) powders were used as starting materials. Mn ion could easily be an impurity in one of the five starting oxides used in the synthesis procedure for Mn-free M3. Therefore, starting powders with quite small amount of Mn (<0.5 ppm) were selected as shown in Table 3-1.

The starting powders were ground in an agate mortar with ethanol. Cylindrical pellets (diameter of 15 mm) were prepared by the uniaxial pressing of the mixed oxides at 27.7 MPa for 1 min. The green samples were then sintered at 1300°C for 6 h with heating rate of 5°C/min in air in an alumina crucible coated with Pt foil. The sintered samples were cooled down in the furnace. The makeup of the starting powder mixtures in the CaO-MnO₂-TiO₂-ZrO₂-Al₂O₃-Fe₂O₃ system are shown in Table 3-2.

Table 3-1 Metal impurities in starting powders (ppm). The impurities, measured by inductively coupled plasma atomic emission spectroscopy (ICP-AES), were given in inspection reports from each supplier.

Impurity	CaO	MnO ₂	TiO ₂	ZrO ₂	α -Al ₂ O ₃	α -Fe ₂ O ₃
Al	ND					≤0.5
As						≤5
Ba	10					≤0.5
Ca		50	10		2	1
Cd						≤0.5
Co		10				10
Cr			10			2
Cu						≤0.5
Fe		30	10	10	2	
Ga						≤0.5
Hf						≤0.5
K			900		1	≤30
Mg		20			1	≤0.5
Mn						0.5
Mo						≤0.5
Na		2000	1000	10	2	≤10
Nb						3
Ni						4
Pb						≤5
Sc						≤0.5
Si		30		10	3	
Sr	90					≤0.5
Ta						≤0.5
Th						
Ti				10		≤0.5
U						
V						1
W						≤0.5
Zn						4
Zr						≤0.5

Table 3-2 Compositions of murataite samples (in mol.%)

Starting powder	CTZAF	CMTZAF
CaO	20.1	15.6
MnO ₂	-	10.2
TiO ₂	31.2	37.1
ZrO ₂	15.2	12.7
α -Al ₂ O ₃	11.3	9.5
α -Fe ₂ O ₃	22.2	14.9

3.2.2 Sample characterizations

Transmission electron microscope-selected area electron diffraction pattern (TEM-SAED: JEOL, JEM-ARM200F, Japan) was observed in order to discover the superstructure of this particular murataite.

The phases in the pulverized samples were analyzed by XRD (Rigaku, Multiflex, counter diffractometer with graphite-monochromatized Cu-K α radiation ($\lambda_{\text{CuK}\alpha 1} = 1.54056 \text{ \AA}$, $\lambda_{\text{CuK}\alpha 2} = 1.54439 \text{ \AA}$), operated at 40 kV and 40 mA), using a reflection-free single-crystal silicon stage. The slit sizes of divergence slit, scatter slit, and receiving slit were 1°, 1°, and 0.15 mm, respectively. A step scan (step: 0.01° for 2 s) was done in a range of $2\theta = 8\text{--}115^\circ$. The lattice constant, a , of the murataite superstructure was calculated using a Nelson–Riley extrapolation with emphasis on the stronger sub-cell lines.

The chemical composition on the polished section of the bulk samples were measured by scanning electron microscopy (Hitachi TM3000, operated at 15 kV) equipped with energy dispersive X-ray spectrometry (SEM–EDS).

3.3 Results

3.3.1 Phase identification of the M3-type murataite

TEM-SAED (Fig. 3-2) and XRD (Fig. 3-3, 3-4 and Tables 3-3, 3-4) revealed that the samples in the system of Ca-Ti-Zr-Al-Fe-O (CTZAF) and Ca-Mn-Ti-Zr-Al-Fe-O (CMTZAF) after sintering consisted of mainly M3 murataite phases. Phase-pure murataite is difficult to make; however, I produced a phase-pure M3 murataite in the system of CMTZAF. The stronger lines from the FCC fluorite-type sub-cells, those hkl all divisible by 3, were confirmed, which indicates that these samples contained the $3\times 3\times 3$ fluorite-type superstructures. These XRD patterns have good agreement with previous reports by Ercit and Hawthorne [11], Morgan and Ryerson [12], and Pakhomova *et al.* [10]. Their XRD patterns were obtained from the ICDD-JCPDS database (01-086-0888 and 00-036-0138), while Pakhomova's XRD pattern was simulated by using RIETAN-FP software [13].

Most of the very weak peaks from the FCC supercell were clearly observed in the new, simpler M3. The lattice constants were calculated by using the strong certain reflections at high angles, 12 0 0, 9 9 3, 12 6 0, 12 6 6, 15 3 3, 12 12 0, 9 9 9, and 18 0 0. The lattice constants of the CTZAF and CMTZAF are 14.568Å and 14.559Å, respectively.

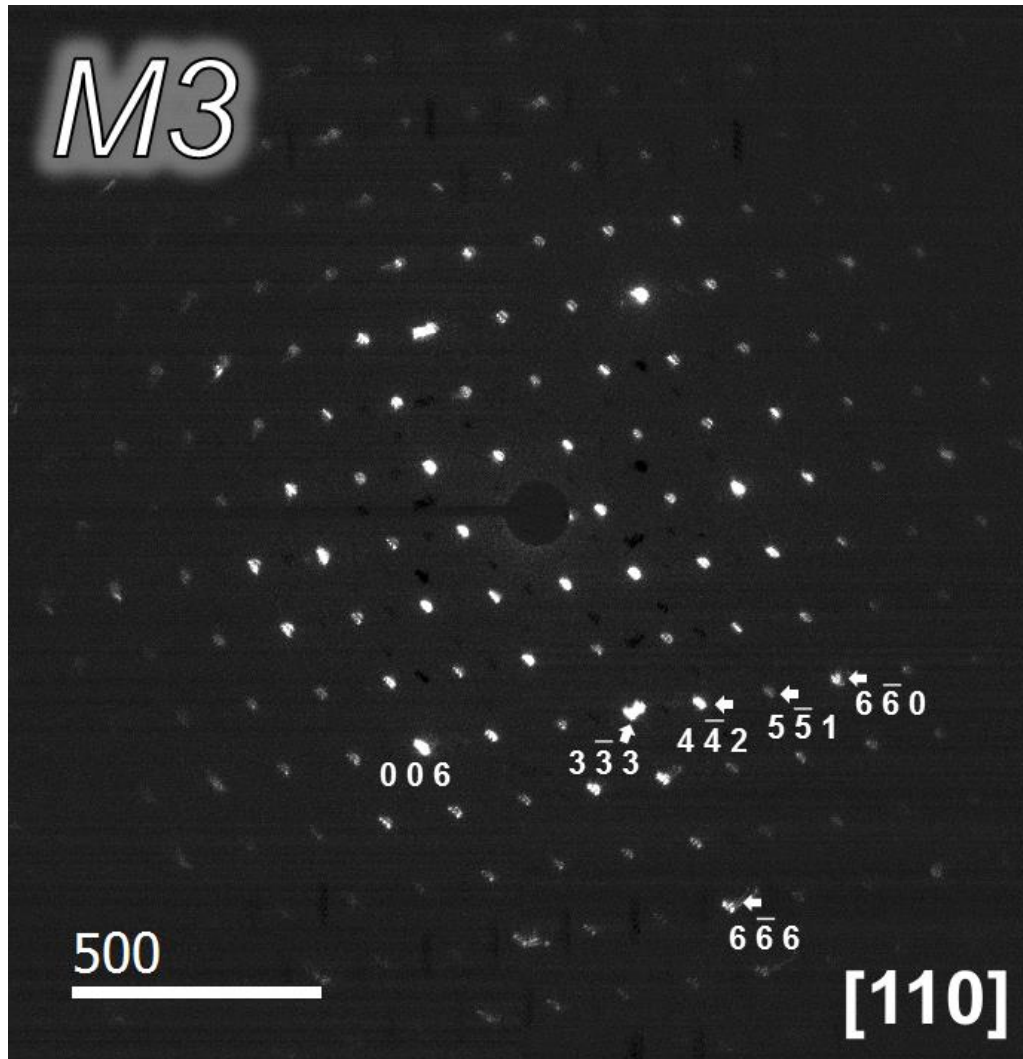


Fig. 3-2 SAED pattern of M3 in the (1 1 0) plane of the reciprocal lattice from new M3 (CTZAF). The hkl reflections with $h, k, l = 3n$ from FCC fluorite-type sub-cell are strong in M3 murataite. The weak reflections from the fluorite-type supercell are observed between the strong reflections.

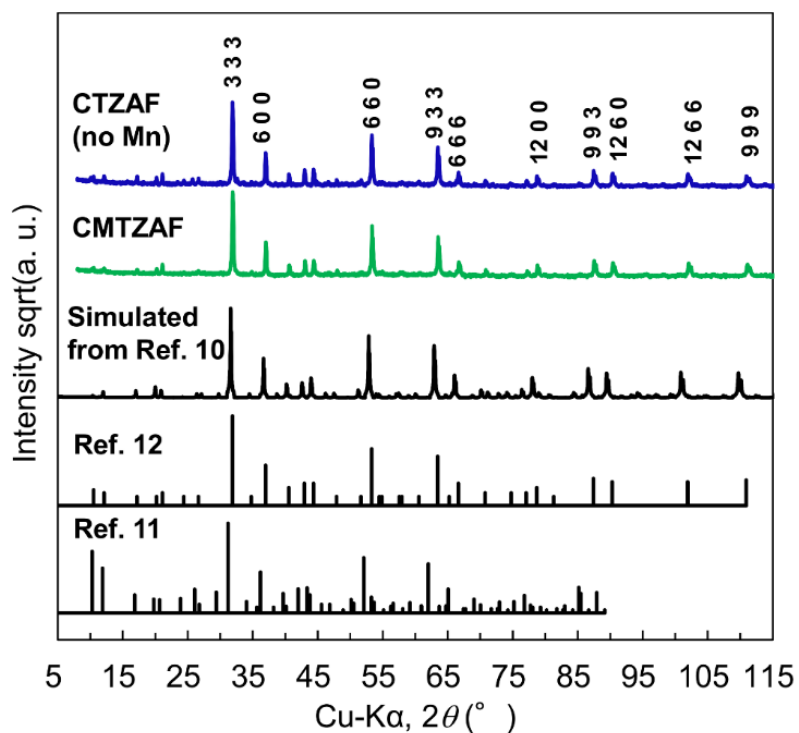


Fig. 3-3 X-ray diffraction patterns of M3 from this work, natural [11] and synthetic [10,12] murataite. All XRD patterns are shown on a square root intensity scale to emphasize the weak peaks from the supercell.

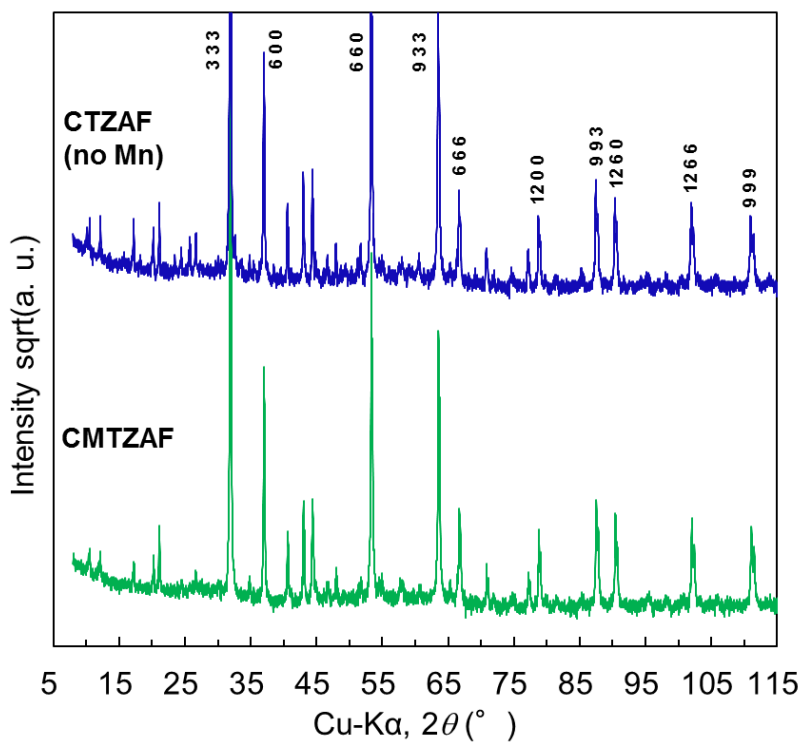


Fig. 3-4 X-ray diffraction patterns obtained in this study on a square root scale.

Table 3-3 X-ray spacing, peak intensities, indices and d spacing from M3 (CMTZAF) at $2\theta = 10\text{-}115^\circ$ (Cu- $K\alpha_1$ radiation)

$2\theta_{\text{obs}}$	$d_{\text{obs}} (\text{\AA})$	I/I_0	hkl	$d_{\text{calc}} (\text{\AA})$	Δd
10.54	8.386	2.4	1 1 1	8.406	-0.019
12.14	7.284	2.2	2 0 0	7.279	0.005
17.20	5.151	1.8	2 2 0	5.147	0.004
20.24	4.384	2.1	3 1 1	4.390	-0.006
21.12	4.203	3.6	2 2 2	4.203	0.000
24.40	3.645	1.1	4 0 0	3.640	0.005
26.64	3.343	1.4	3 3 1	3.340	0.003
30.08	2.968	1.1	4 2 2	2.972	-0.003
31.92	2.801	100.0	5 1 1	2.802	0.000
34.84	2.573	1.2	4 4 0	2.574	-0.001
36.72	2.445	1.3	5 3 1	2.461	-0.015
37.02	2.426	19.4	6 0 0	2.426	0.000
39.28	2.292	0.7	6 2 0	2.302	-0.010
40.62	2.219	3.3	5 3 3	2.220	-0.001
41.16	2.191	0.8	6 2 2	2.195	-0.004
43.04	2.100	5.3	4 4 4	2.101	-0.002
44.38	2.040	5.4	7 1 1	2.039	0.001
44.96	2.015	1.1	6 4 0	2.019	-0.004
46.66	1.945	1.1	6 4 2	1.946	0.000
48.00	1.894	1.5	7 3 1	1.895	-0.002
51.44	1.775	1.0	7 3 3	1.779	-0.004
51.78	1.764	1.2	8 2 0	1.766	-0.001
53.34	1.716	38.6	6 6 0	1.716	0.000
54.54	1.681	1.2	7 5 1	1.681	0.000
54.96	1.669	1.3	6 6 2	1.670	-0.001
56.60	1.625	0.8	8 4 0	1.628	-0.003
57.68	1.597	1.1	9 1 1	1.598	-0.001
58.04	1.588	1.1	8 4 2	1.588	-0.001
59.76	1.546	0.8	6 6 4	1.552	-0.006
60.64	1.526	1.0	9 3 1	1.526	0.000
62.56	1.484	0.8	8 4 4	1.486	-0.002
63.52	1.463	24.8	7 7 1	1.463	0.000
65.28	1.428	1.1	10 2 0	1.428	0.001
66.38	1.407	1.3	9 5 1	1.407	0.000

Continued

Table 3-3 Continued

$2\theta_{\text{obs}}$	$d_{\text{obs}} (\text{\AA})$	I/I_0	hkl	$d_{\text{calc}} (\text{\AA})$	Δd
66.70	1.401	4.8	10 2 2	1.401	0.000
69.06	1.359	0.6	9 5 3	1.358	0.001
70.84	1.329	1.7	10 4 2	1.329	0.000
71.92	1.312	0.7	11 1 1	1.313	-0.001
73.62	1.286	0.6	8 8 0	1.287	-0.001
74.82	1.268	0.7	8 8 2	1.267	0.001
77.12	1.236	0.8	11 3 3	1.235	0.001
77.20	1.235	1.4	10 6 2	1.230	0.004
78.80	1.214	3.4	12 0 0	1.213	0.000
79.82	1.201	0.7	11 5 1	1.201	0.000
81.46	1.181	0.7	12 2 2	1.181	0.000
85.32	1.137	0.7	10 8 0	1.137	0.000
87.52	1.114	5.3	13 1 1	1.113	0.000
90.40	1.086	4.4	12 6 0	1.085	0.000
95.62	1.040	0.7	14 0 0	1.040	0.000
98.10	1.020	0.7	14 2 2	1.019	0.001
100.76	1.000	0.7	14 4 0	1.000	0.000
102.04	0.991	4.1	14 4 2	0.991	0.000
105.94	0.965	0.7	14 4 4	0.964	0.001
111.12	0.934	3.6	11 11 1	0.934	0.000
113.92	0.919	0.7	15 5 1	0.919	0.000
117.14	0.903	0.8	16 2 0	0.903	0.000
118.64	0.896	0.7	16 2 2	0.896	0.000
119.70	0.891	1.3	11 11 5	0.891	0.000
122.66	0.878	1.0	15 7 1	0.878	0.000
122.98	0.877	1.0	16 4 2	0.876	0.000
127.74	0.858	1.6	12 12 0	0.858	0.000

Table 3-4 X-ray spacing, peak intensities, indices and d spacing from new M3 (CTZAF) at $2\theta = 10\text{-}115^\circ$ (Cu- $K\alpha_1$ radiation)

2θ	d_{obs} (Å)	I (%)	hkl	d_{calc} (Å)	Δd
10.50	8.418	3.1	1 1 1	8.411	0.007
12.14	7.284	3.2	2 0 0	7.284	0.000
17.22	5.145	3.1	2 2 0	5.151	-0.005
20.20	4.392	2.6	3 1 1	4.392	0.000
21.10	4.207	4.0	2 2 2	4.205	0.002
24.42	3.642	1.6	4 0 0	3.642	0.000
26.68	3.338	2.3	3 3 1	3.342	-0.004
27.24	3.271	1.2	4 2 0	3.258	0.014
30.00	2.976	1.3	4 2 2	2.974	0.002
31.88	2.805	100.0	5 1 1	2.804	0.001
34.82	2.574	1.4	4 4 0	2.575	-0.001
36.32	2.471	1.1	5 3 1	2.462	0.009
36.98	2.429	19.1	6 0 0	2.428	0.001
39.06	2.304	0.8	6 2 0	2.303	0.001
40.56	2.222	4.0	5 3 3	2.222	0.001
41.20	2.189	0.9	6 2 2	2.196	-0.007
42.98	2.103	6.2	4 4 4	2.103	0.000
44.36	2.040	6.4	7 1 1	2.040	0.000
44.82	2.021	1.5	6 4 0	2.020	0.000
46.62	1.947	1.4	6 4 2	1.947	0.000
47.92	1.897	1.9	7 3 1	1.897	0.000
50.34	1.811	1.0	8 0 0	1.821	-0.010
51.28	1.780	1.3	7 3 3	1.780	0.000
51.70	1.767	1.8	8 2 0	1.767	0.000
53.30	1.717	40.1	6 6 0	1.717	0.000
54.48	1.683	1.3	7 5 1	1.682	0.001
54.92	1.670	1.4	6 6 2	1.671	-0.001
56.50	1.627	0.9	8 4 0	1.629	-0.001
57.54	1.600	1.1	9 1 1	1.599	0.001
57.96	1.590	1.3	8 4 2	1.590	0.000
59.54	1.551	1.0	6 6 4	1.553	-0.002
60.60	1.527	1.4	9 3 1	1.527	0.000
62.08	1.494	0.9	8 4 4	1.487	0.007
63.48	1.464	25.1	7 7 1	1.464	0.000

Continued

Table 3-4 Continued

2θ	d_{obs} (Å)	I (%)	hkl	d_{calc} (Å)	Δd
65.32	1.427	1.1	10 2 0	1.429	-0.001
66.34	1.408	1.6	9 5 1	1.408	0.000
66.66	1.402	4.8	10 2 2	1.402	0.000
69.08	1.359	0.9	9 5 3	1.358	0.000
70.78	1.330	1.6	10 4 2	1.330	0.000
71.96	1.311	0.9	11 1 1	1.314	-0.002
74.64	1.271	1.0	8 8 2	1.268	0.003
77.14	1.235	1.6	11 3 3	1.236	0.000
78.72	1.215	3.2	12 0 0	1.214	0.001
79.72	1.202	0.7	11 5 1	1.202	0.000
81.32	1.182	0.8	12 2 2	1.182	0.001
85.22	1.138	0.9	10 8 0	1.138	0.000
87.46	1.114	5.6	13 1 1	1.114	0.000
90.36	1.086	4.3	12 6 0	1.086	0.000
91.72	1.073	0.7	12 6 2	1.074	-0.001
94.34	1.050	0.7	8 8 8	1.051	-0.001
95.12	1.044	0.8	13 5 1	1.043	0.001
98.06	1.020	0.8	14 2 2	1.020	0.000
100.48	1.002	0.8	11 9 3	1.003	-0.001
101.96	0.991	4.0	14 4 2	0.991	0.000
102.96	0.985	0.8	13 7 1	0.984	0.000
105.64	0.967	0.8	15 1 1	0.967	0.000
108.42	0.950	0.7	15 3 1	0.950	-0.001
110.94	0.935	3.2	11 11 1	0.935	0.000
113.86	0.919	0.8	15 5 1	0.920	0.000
116.94	0.904	0.8	16 2 0	0.903	0.000
118.30	0.897	0.8	16 2 2	0.897	0.001
119.46	0.892	1.0	11 11 5	0.892	0.000
121.36	0.883	0.8	16 4 0	0.883	0.000
122.80	0.877	0.9	16 4 2	0.877	0.000
127.58	0.859	1.7	12 12 0	0.858	0.000

3.3.2 Microstructural observation of Mn-free and regular M3

The measured chemical composition of cations of each murataite are shown in Table 3-5. Figure 3-5 shows the detected area in the SEM images. The chemical compositions of M3 phase measured by EDS agreed well with starting compositions of each sample (Table 3-2), which endorses that the elemental analysis was correctly done. The samples of CTZAF, CMTZAF and Ref. 12 were obtained by the solid-state reaction method. (Incidentally, regrinding and refiring, did not improve the amount/purity of the M3). The sample of Ref. 10 was synthesized by the melting method; the murataites by solid-state synthesis, especially in CTZAF, have much more Al and Fe ions compared with that formed by the melt-method. On the other hand, a noticeably lower amount of Ti ion was confirmed in my M3 phases.

Table 3-5 Chemical compositions (atom.%) of cations of each M3

	CTZAF	CMTZAF	Ref. 9 (Morgan)	Ref. 10 (Pakhomova)
Tb	-	-	-	9.05
Ca	15.10	12.53	12.0	12.13
Mn	-	8.23	8.0	10.11
Ti	23.42	29.77	30.0	56.10
Zr	11.39	10.18	10.0	8.25
Al	16.89	15.28	15.0	3.19
Fe	33.20	24.01	25.0	1.17

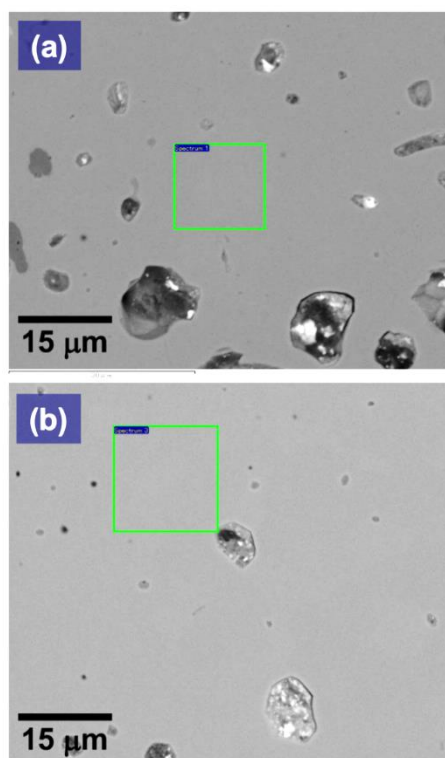


Fig. 3-5 Microstructural mirror polished surface of (a) CTZAF and (b) CMTZAF. The detected areas are shown in Green Square.

3.4 Discussion

3.4.1 Comparison of XRD patterns between the natural and synthetic murataite

The mineral murataite displayed rather stronger low-angle peaks. Thus the weaker low-angle peaks in synthetic murataite must relate to the presence of the additional site of the larger cations such as actinide, rare earth and alkaline earth metal with 8-coordinated, which are absent in the natural mineral.

3.4.2 Comparison of chemical compositions between the conventional and Mn-free murataite

Fe ion is now the major cation in CTZAF, likely because Fe can easily fill 6-, 5- and 4-coordination sites. This should make analyses easier in future. In previous work, Ryerson [14] and Begg [15] also reported a Fe-rich murataite with low Mn. These murataites, however, contained more other metal cations with the lower Mn.

Various compounds with fluorite-related structures, such as pyrochlore and zirconolite, have been considered promising for immobilization of actinide-containing HLW. It was found that five volume percent of synthetic murataite accumulate about 40% of the total amount of uranium present in a sample [16]. The optimal content, 10 wt.%, of wastes in murataite-pyrochlore series, which is close to the values of pyrochlore ceramics for Pu immobilization, was reported in the previous work [7]. Furthermore, its radiation resistance is comparable to titanate pyrochlores [17]. The further investigations for structural analysis and capability of the murataite-pyrochlore polysomatic series could lead to a superior crystalline radioactive waste host material with immobilization of a large proportion of HLW, including REE and (normally hindering) corrosion products such as iron and aluminum; with the natural mineral assurance, for hundreds of millions of years. It is noteworthy that the finding about Fe-rich murataite series supports the immobilization of waste streams that have complex compositions in the nuclear fuel cycle, eliminating some need for awkward chemical separations [18-20].

3.5 Conclusions

The new M3 phase, with no Mn, is synthesized by solid-state synthesis; interestingly, it also contains much Fe. There were some general differences of chemical composition between the M3 by solid-state synthesis and by the melting method - my M3 phases have much more Al and Fe cations. On the other hand, much less Ti cation was seen, so that the major cation in the new M3 is Fe instead of Ti.

An interesting possibility also, is that this M3 type may exist as a yet undiscovered (rare) mineral; other minerals with fluorite sub-cells, pyrochlore, zirconolite, tranquillityite and ordinary-mineral-type murataite, are known.

To view whole investigation described in this Chapter, please visit <http://dx.doi.org/10.1016/j.jallcom.2016.12.142> [21].

References

- [1] J. W. Adams, T. Botinelly, W. N. Sharp, and K. Robinson, "Murataite, a new complex oxide from El Paso County, Colorado," *Am. Mineral.*, **59** [1-2] 172-176 (1974).
- [2] S. V. Yudintsev, S. V. Stefanovsky, B. S. Nikonov, K. I. Maslakov, and A. G. Ptashkin, "Structural characterization of Pu-bearing murataite ceramic," *J. Alloys Compd.*, **444-445** 606–609 (2007).
- [3] K. I. Maslakov, A. Yu. Teterin, Yu. A. Teterin, K. E. Ivanov, S. V. Yudintsev, and S. V. Stefanovskii, "X-ray photoelectron study of murataite ceramics containing Th, U, Np, and Pu," *Radiochemistry*, **54** [2] 115-121 (2012).
- [4] N. P. Laverov, S. V. Yudintsev, S. V. Stefanovskii, B. I. Omel'yanenko, and B. S. Nikonov, "Murataite as a universal matrix for immobilization of actinides," *Geol. Ore Deposits*, **48** [1] 335-356 (2006).
- [5] N. P. Laverov, V. S. Urusov, S. V. Krivovichev, A. S. Pakhomova, S. V. Stefanovsky, and S. V. Yudintsev, "Modular nature of the polysomatic pyrochlore-murataite series," *Geol. Ore Deposits*, **53** [4] 273–294 (2011).
- [6] O. V. Karimova, N. I. Organova, and V. G. Balakirev, "Modulation in the murataite structure," *Crystallogr. Rep.*, **47** [6] 957-960 (2002).
- [7] N. P. Laverov, S. V. Yudintsev, S. V. Stefanovskii, B. I. Omel'yanenko, and B. S. Nikonov, "Murataite matrices for actinide wastes," *Radiochemistry*, **53** [3] 229-243 (2011).
- [8] S. V. Krivovichev, V. S. Urusov, S. V. Yudintsev, S. V. Stefanovsky, O. V. Karimova, and N. N. Organova, "Crystal structure of murataite Mu-5, a member of the murataite-pyrochlore polysomatic series," in: S. V. Krivovichev (Eds.), *Minerals as Advanced Materials II*, Berlin Heidelberg, 2012, pp. 293-304.
- [9] K. Momma and F. Izumi, VESTA 3 for three-dimensional visualization of crystal, volumetric and morphology data, *J. Appl. Cryst.*, **44** 1272-1276 (2011).
- [10] A. S. Pakhomova, S. V. Krivovichev, S. V. Yudintsev, and S. V. Stefanovsky, "Synthetic murataite-3C, a complex form for long-term immobilization of nuclear waste: crystal structure and its comparison with natural analogues," *Z. Kristallogr.*, **228** [3] 151-156 (2013).
- [11] T. S. Ercit and F. C. Hawthorne, "Murataite, a UB_{12} derivative structure with condensed Keggin molecules," *Can. Mineral.*, **33** 1223-1229 (1995).
- [12] P. E. D. Morgan and F. J. Ryerson, "A new "cubic" crystal compound," *J. Mater. Sci. Lett.*, **1** [8] 351-352(1982).
- [13] F. Izumi and K. Momma, "Three-dimensional visualization in powder diffraction," *Solid State Phenom.*, **130** 15-20 (2007).
- [14] F. J. Ryerson, "Phase equilibria of nuclear waste ceramics: the effect of oxygen fugacity," *J. am. Ceram. Soc.*, **67** [2] 75-82 (1984).
- [15] B. D. Begg, E. R. Vance, H. Li, T. McLeod, N. Scales, and M. Bhati, "Titanate ceramic matrices for alumina-rich wastes," *Mat. Res. Soc. Symp. Proc.*, **807** 321-326 (2004).
- [16] N. P. Laverov, I. A. Sobolev, S. V. Stefanovskii, S. V. Yudintsev, B. I. Omel'yanenko, and B. S. Nikonov, "Synthetic murataite: a new mineral for actinide immobilization," *Dokl. Earth Sci.*, **363** [8] 1104-1106 (1998).
- [17] S. V. Stefanovsky, S. V. Yudintsev, and T. S. Livshits, "New cubic structure compounds as actinide host phases," *IOP Conf. Ser.: Mater. Sci. Eng.*, **9** [1] 012001 (2010).
- [18] R. C. Ewing, "Safe management of actinides in the nuclear fuel cycle: Role of mineralogy," *C. R. Geoscience*, **343** [2-3] 219-229 (2011).

- [19] A. S. Pakhomova, S. V. Krivovichev, S. V. Yuditsev, and S. V. Stefanovsky, "Polysomatism and structural complexity: Structure model for murataite-8C, a complex crystalline matrix for the immobilization of high-level radioactive waste," *Eur. J. Mineral.*, **28** [1] 205-214 (2016).
- [20] Committee on waste forms technology and performance, Nuclear and radiation studies board, Division on earth and life studies, National research council, possible opportunities in waste form science and technology, Waste Forms Technology and Performance: Final Report, National Research Council of National Academies, The National Academies Press, Washington D.C., 2011.
- [21] R. S. S. Maki, P. E. D. Morgan and Y. Suzuki, "Synthesis and Characterization of a Simpler Mn-free, Fe-rich M3-type Murataite," *J Alloys Compd.*, **698** [25] 99-102 (2017).

Chapter 4

Structural Analysis and Visual Characterization for M3-type Murataite

Chapter 4: Structural Analysis and Visual Characterization for M3-type Murataite

In earlier Chapters, I noted some differences between the murataite ceramics synthesized by solid-state reaction and melting method. In addition to this, very pure M3 sample and simpler (Mn-free) one were successfully synthesized. I reported here the structural characterizations for M3-type murataite with powder X-ray diffraction, calculation of powder diffraction intensities (plus simulation) and STEM-EELS analysis using the general and simpler M3. It was indicated that the site preference of Zr ion was slightly different from that reported in previous works; in this work, mainly occupied at *Ca1* site instead of *Ti* site. HAADF-STEM observation demonstrated that the huge layered defects observed in Chapter 2 were not confirmed in the highly stable M3 phase in purer samples. The instability of the superstructure of murataite series could be important for the formation of these enormous defects.

4.1 Introduction

A synthetic murataite ceramics is now recognized as an anion-deficient $3\times 3\times 3$ fluorite-type superstructure (M3) with ordered arrangement of cations [1]. The first finding of the similar crystal structure, natural mineral murataite, was reported by Adams *et al.* in 1972 [2], and then its structural analysis was developed by Ercit and Hawthorne in 1995 [3]; cubic, space group $F\bar{4}3m$ (216) and $a = 14.886(2)$ Å. The ideal formula is $(Y, Na)_6(Zn, Fe)_5Ti_{12}O_{29}(O, F)_{10}F_4$ with $Z = 4$, but its simple appearance is likely due to extensive cation disorder within the structure. This crystal structure contains four symmetrically independent cation positions with α -Keggin cluster, $^{[4]T^{[6]}}M_{12}O_{40}$ ($T = Zn, Al; M = Ti$), considered to be the fundamental building block of murataite structure. The synthetic version of murataite M3 was firstly synthesized by Morgan in 1982 [4]. Subsequently, detailed crystal structure was presented much later by Pakhomova *et al.* in 2013 [1].

A synthetic M3 is presently believed to contain five symmetrically independent cation positions instead of only four positions in natural murataite, and formulated as $^{[8]}CaI_6^{[8]}Ca2_4^{[6]}TiI_{12}^{[5]}Ti2_4^{[4]}AlO_{42}$, where $Ca = Ca, Mn, REE; Ti = Ti, Zr, Al; Al = Al, Fe$ with space group $F\bar{4}3m$ (216) and $Z = 4$ [1]. *Ca2* is the additional site with 8-coordination in synthetic M3. The formation of M3 phase was mainly achieved by melting methods, which produces crystals with complicating zoning of mixed types [5-8] such as other murataite varieties, $5\times 5\times 5$ (M5), $7\times 7\times 7$ (M7) and $8\times 8\times 8$ (M8) fluorite-type superstructure [9-11]. Depending on the synthesis procedure and conditions, the phase transition between these superlattices and cation substitution at each cation site can typically occur [12]. This complexity makes the structural analyses of murataite series quite challenging.

In this study, the crystal structure of M3-type murataite was characterized with powder X-ray diffraction technique (PXRD) using general and simpler M3 samples synthesized in above Chapter 3 [13]. I have tried to substitute Hf ion into Zr site within M3 structure of CMTZAF in order to determine the site preference of Zr ion. The ionic radius of Hf and Zr at 8-coordination is almost same, $r = 0.83$ and 0.84 , respectively [14], but this Hf-substituted M3-type murataite (CMTHAF) indicates different diffraction intensities in XRD pattern depending on the different atomic scattering factor of both Hf and Zr atoms. Furthermore, an element distribution was visually characterized by element mapping with scanning transmission electron microscopy-electron energy loss spectroscopy (STEM-EELS) to confirm the site preference of each cation, especially Zr

ion.

4.2 Experimental procedure

4.2.1 Sample preparation

Commercial CaO (99.9% purity, Kojundo Chemical Laboratory Co. Ltd.), MnO₂ (99% purity, Kojundo Chemical Laboratory Co. Ltd.), TiO₂ anatase (99% purity, Kojundo Chemical Laboratory Co. Ltd.), ZrO₂ (98% purity, Kojundo Chemical Laboratory Co. Ltd.), α -Al₂O₃ (99.99% purity, Taimei Chemicals Co. Ltd., Saitama, Japan), α -Fe₂O₃ (99.9% purity, Wako Pure Chemical Industries Ltd.) and HfO₂ (95.0% purity, Wako Pure Chemical Industries Ltd.) powders were used as starting materials. The selected starting powders with quite small amount of Mn (≤ 1.0 ppm) are shown in detail in Chapter 3.

The starting powders were ground in an agate mortar with ethanol. Cylindrical pellets (diameter of 15 mm) were prepared by the uniaxial pressing of the mixed oxides at 27.7 MPa for 1 min. The green samples were then sintered at 1300°C for 6 h with heating rate of 5°C/min in air in an alumina crucible coated with Pt foil. The sintered samples were cooled down in the furnace. The samples prepared with the powder mixture of the ratio of CaO: MnO₂: TiO₂: ZrO₂: α -Al₂O₃: α -Fe₂O₃ = 20.1 : 0.0 : 31.2 : 15.2 : 11.3 : 22.2 (CTZAF) and 15.6 : 10.2 : 37.1 : 12.7 : 9.5 : 14.9 (CMTZAF) in mol.% after sintering consist of mainly murataite M3 phase [13]. CTZAF is simpler (Mn-free) M3 sample, which only has 5 cations, Ca, Ti, Zr, Al and Fe, instead of 6 cations in conventional M3-type murataite. To prepare the Hf-substituted sample, a powder mixture using HfO₂ instead of ZrO₂ was ground and sintered by the same method as above.

4.2.2 Microstructural observation

High angle annular dark field-scanning transmission electron microscopy (HAADF-STEM: JEOL, JEM-ARM200F, Japan) was used for microstructural observation of the crushed sample. In the HAADF-STEM method, it is possible to obtain a z-contrast which depends on the atomic number. In addition to this, element mapping was performed by STEM- electron energy loss spectroscopy (EELS)/ multivariate analysis method.

The chemical composition on the polished section of the bulk samples were measured by scanning electron microscopy (Hitachi TM3000, operated at 15 kV) equipped with energy dispersive X-ray spectrometry (SEM-EDS).

4.2.3 Chemical analysis

X-ray photoelectron spectroscopy (XPS) was performed to determine the oxidation state of iron and manganese ions within the murataite. The pulverized samples were immediately set into the XPS measurement chamber since the sample surface can be easily oxidized and contaminated, which change the oxidation states of transition metals such as Fe and Mn. The analyzer was operated with an incident monochromated X-ray beam from the Al target (10 kV, 20 mA) and a pass energy of 50 eV (JEOL, JPS-9010TR, Japan). The step size of 0.1 eV was conducted and each peak was scanned 30 times. Carbon commonly present on all surface for XPS analysis, and carbon C 1s peak at 285 eV was used as a reference for charge correction throughout this study. The Savitzky-Golay method and Shirley method were selected for peak smoothing and background

subtraction, respectively. In this study, the Fe and Mn oxidation states was distinguished using satellite features of Fe2p and Mn2p, respectively [15-17].

4.2.4 Sample characterizations

The phases in the pulverized samples were analyzed by XRD (Rigaku, Multiflex, counter diffractometer with graphite-monochromatized Cu-K α radiation ($\lambda_{\text{CuK}\alpha 1} = 1.54056 \text{ \AA}$, $\lambda_{\text{CuK}\alpha 2} = 1.54439 \text{ \AA}$), operated at 40 kV and 40 mA), using a reflection-free single-crystal silicon stage. The slit sizes of divergence slit, scatter slit, and receiving slit were 1°, 1°, and 0.15 mm, respectively. A step scan (step: 0.01° for 2 s) was done in a range of $2\theta = 10\text{-}50^\circ$ at room temperature.

Calculation of powder diffraction intensities (plus simulation) for the determination of the site preference of Zr ion was performed by substituting the Hf ion into the each cation site within M3 crystal structure reported by Pakhomova *et al.* with the RIETAN-FP program [18].

4.3 Results and discussion

4.3.1 Cation distribution in Mn-free M3 observed by HAADF-STEM and EELS analysis

Z-contrast images in the (100) plane of the reciprocal lattice were obtained by HAADF-STEM observation using crushed sample of simpler (Mn-free) M3, CTZAF. The technique of Z-contrast can provides the intensity of atom columns which directly reflects their mean square atomic number (Z), and the location of atom column positions is greatly simplified. In this study, scanning was performed horizontally in the horizontal direction with respect to the screen in order from the top of the image. Thus, the deviation of the column position in the vertical direction in the HAADF-STEM image is due to the drift of the sample. The EEL spectrum in the energy range from 40 to 550 eV was separately applied for the analysis of Al spectra. Multivariate statistical analysis was carried out to remove the noise from single crystals with principal component analysis in MSA software (HREM Research Inc., Japan) [19].

An element mapping by EELS (Fig. 4-1 and 4-2) produced that Zr ions are present in the same column as Ca instead of Ti, on the other hand, Ti, Fe and Al ions seems to be present in the same column. The present observation demonstrates that Ti, Fe and Al ions are on the same column, whereas Zr is located on the same column as the Ca, which is the 8-coordination. This data is slightly different from the result of structural analysis for M3 using single crystal XRD method in the previous work by Pakhomova *et al.*, but agreed well with the cation distribution observed in Chapter 2.4.4. In this study, good HAADF-STEM images for element mapping with atomic resolution, especially in Ca and Fe, were successfully observed by using simpler M3-type murataite sample, CTZAF, compared with in Chapter 2.

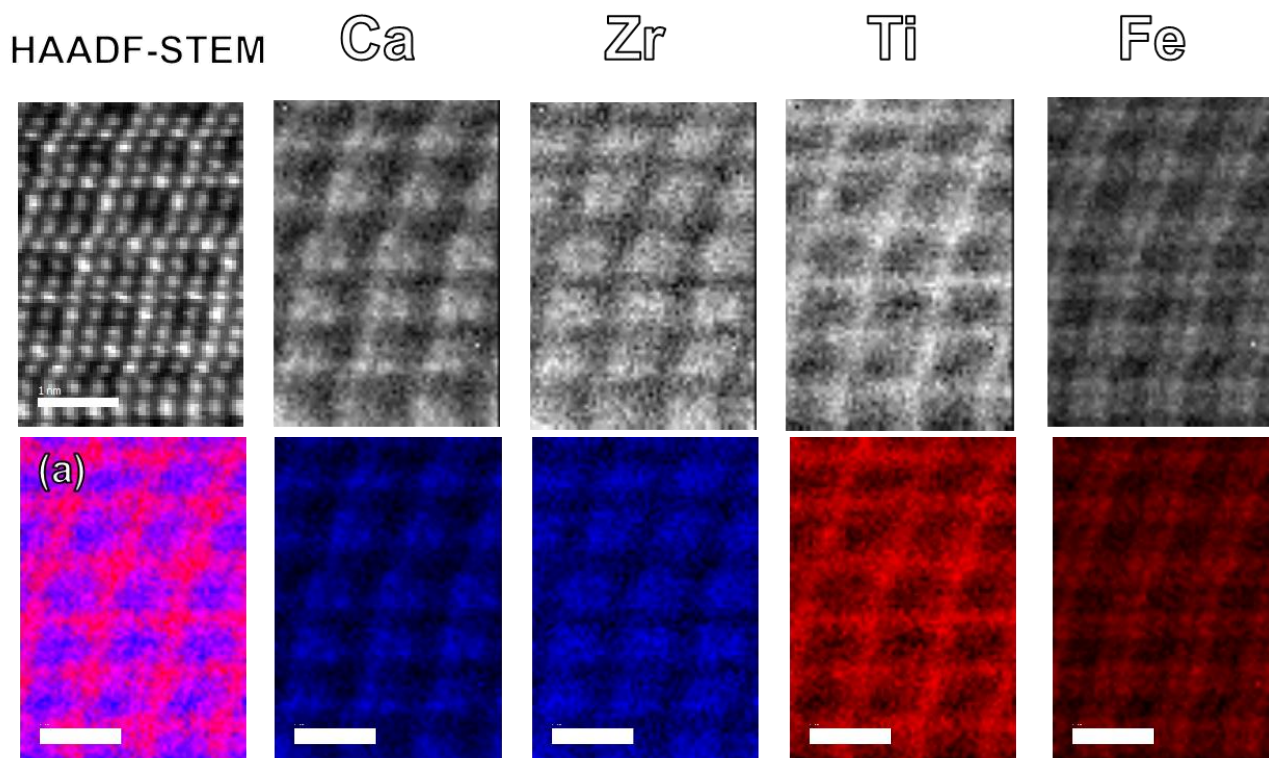


Fig. 4-1 HAADF-STEM image and STEM-EELS maps showing the distribution of Ca, Zr, Ti and Fe from simpler (Mn-free) M3 sample of CTZAF (Upper row). (a) RGB color-overlay image of CTZAF is shown in bottom row.

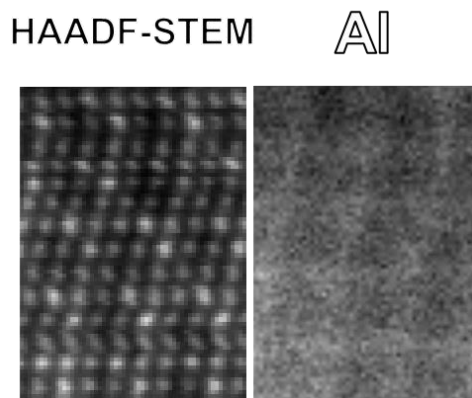


Fig. 4-2 HAADF-STEM image and STEM-EELS map showing the distribution of Al from simpler (Mn-free) M3 sample of CTZAF.

4.3.2 Dependence of the microstructure of murataite series on synthesis conditions

HAADF-STEM image (Fig. 4-3) shows the microstructure of CMTZAF. In the sample, a layered defect having a periodicity much larger than the lattice constant of M3 (it appears as diamond-like in Fig. 2-11) as observed in Sample A-1 (described in Chapter 2) was not presented. Also in the CTZAF, this layered defect was not confirmed, thus, I considered that the presence of the large layered defect might depend on the intergrowth of the murataite series.

Chapter 4

In XRD pattern (Fig. 4-3), the M3 phase of CTZAF and CMTZAF unchanged depending on sintering conditions. There are no visible lines belonging to other members of murataite family, *e.g.* M8, M7 or M5; *viz.* no coherent intergrowths, which leads to a singular sharp 333 peak at all sintering condition. On the other hand, Sample A-1 showed the formation of M8 phase with increasing the sintering time (Fig. 4-4). The huge layered defects observed in Chapter 2 were not confirmed in the phase-pure M3 sample, CMTZAF and CFTZAF, suggesting that the sample preparation (control of starting powders) greatly affects the microstructure of murataite series likely due to a coherent intergrowth with other murataite phase. Surprisingly, the cation ratios of M3 phase between CMTZAF and Sample A-1 were almost same, except for Ti and Fe ion, analyzed by SEM-EDS (Table 4-1).

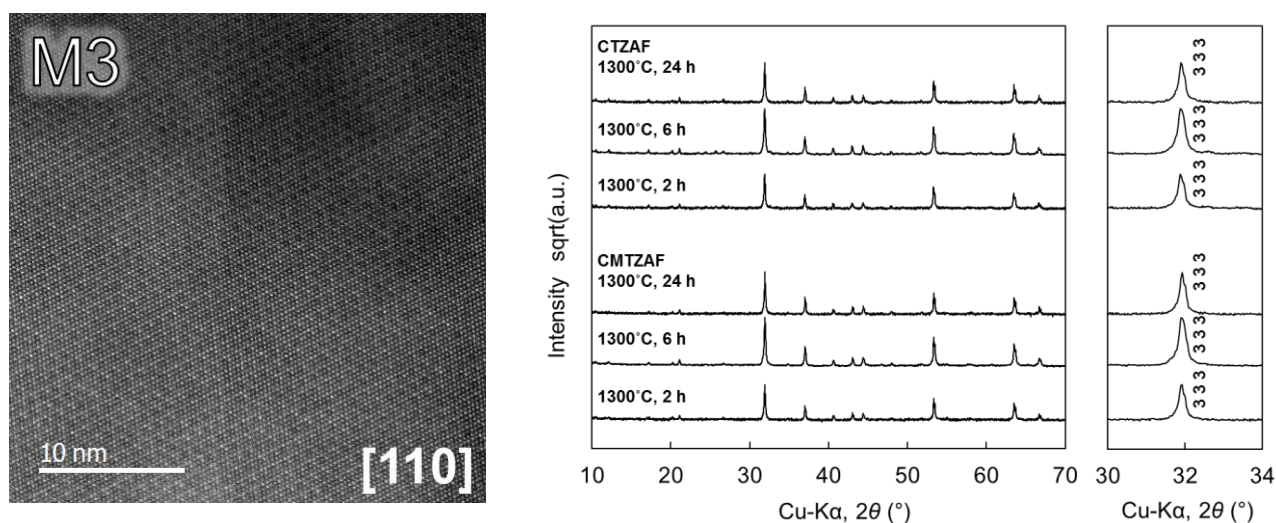


Fig. 4-3 HAADF-STEM image of CMTZAF sintered at 1300°C for 6 h and the dependence of the formation of murataite series on synthesis conditions for CTZAF and CMTZAF.

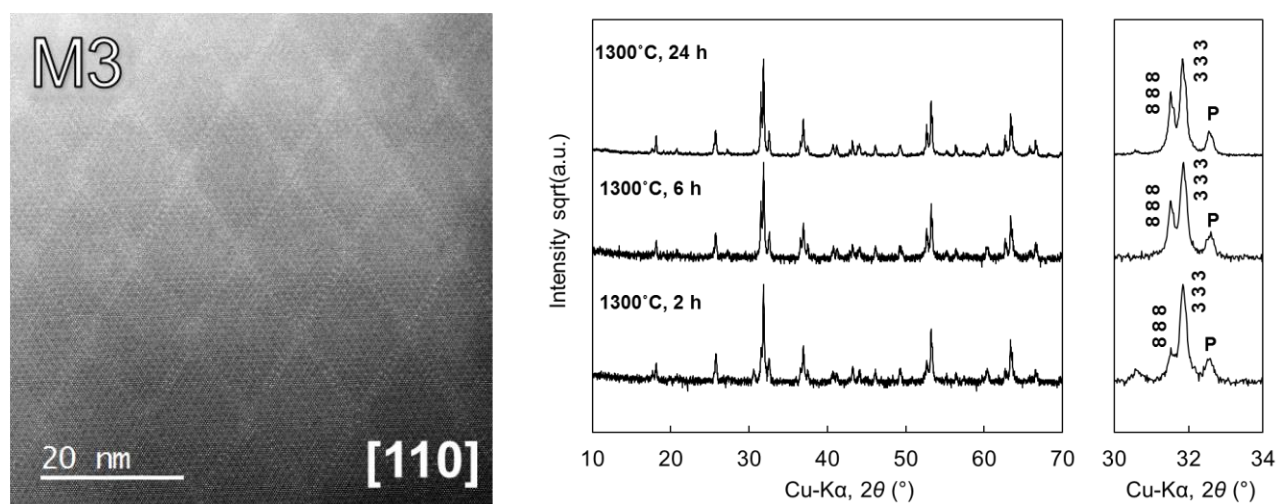


Fig. 4-4 HAADF-STEM image of Sample A-1 sintered at 1300°C for 24 h (described in Chapter 2) and its dependence of the formation of murataite series on synthesis conditions.

Table 4-1 Chemical compositions (atom.%) of cations of each M3 phase in CTZAF, CMTZAF and Sample A-1

	CTZAF	CMTZAF	Sample A-1 (in Chapter 2)
Ca	15.1	12.5	12.0
Mn	0.0	8.2	7.1
Ti	23.4	29.8	34.3
Zr	11.4	10.2	10.8
Al	16.9	15.3	14.8
Fe	33.2	24.0	21.0

4.3.3 Site preference of Zr ion in the M3-type murataite

CMTZAF sample was single phase, and Hf-substituted M3-type murataite (CMTHAF) sample contained some impurities, but chemical composition of these two M3 phase were almost same in SEM-EDS analysis (Fig. 4-5 and Table 4-2).

The experimental XRD patterns of CMTZAF and CMTHAF are given in Fig. 4-6. The diffraction intensity is normalized with the strongest diffraction peak, 511 and 333, as 100%. In the experimental XRD pattern, increase of 111, 200, 222, 400, 420, 600 and 711 peak intensities and 311 peak intensity reduction were confirmed. Other diffraction peak intensities almost unchanged. In the simulated XRD pattern using Pakhomova's M3 structural parameters with replaced site of only *Ca1* site (substitution of Hf into Mn and Tb ion), the intensity change of the each peak showed good agreement with the experimental pattern. On the other hand, the simulated pattern with the replacement site of *Ti1* site (substitution of Hf into Zr ion only) was very different from the intensity change in the experimental pattern. (Fig. 4-7). Thus, site preference of Zr ion was considered to be mainly *Ca1* site in this study. This result agreed well with the element distribution analyzed by STEM-EELS method.

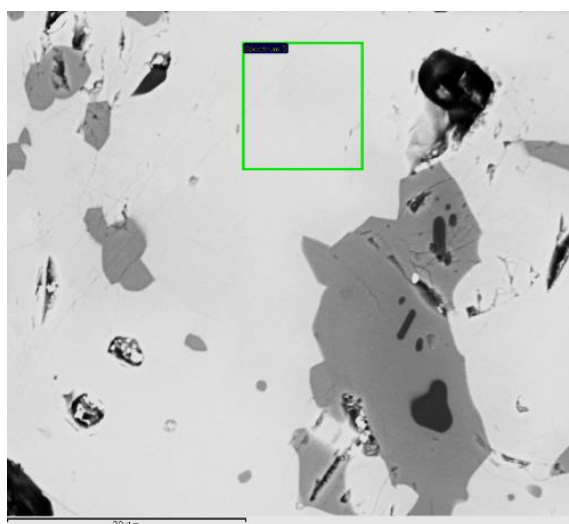
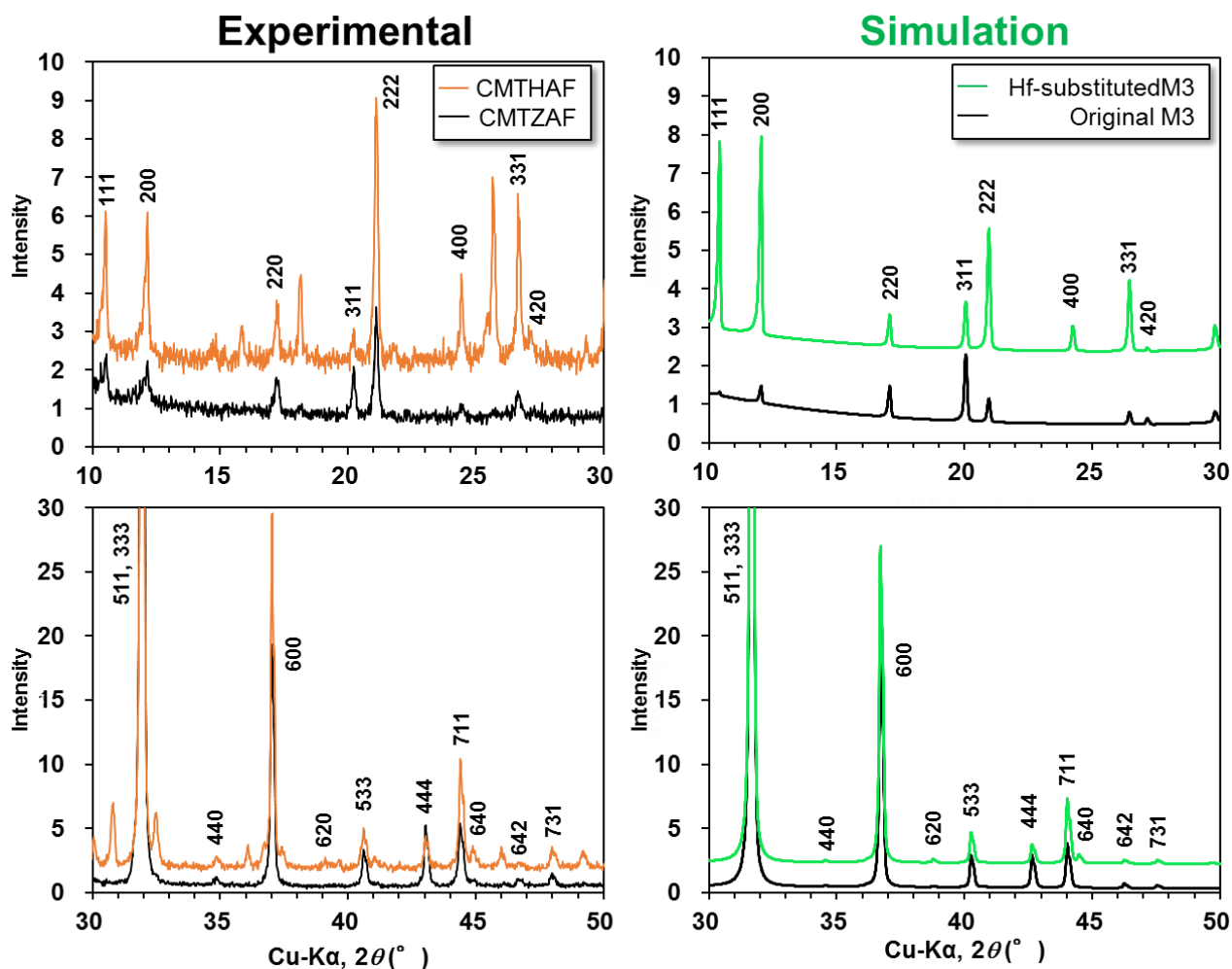
**Fig. 4-5** Microstructural mirror polished surface of CMTHAF. The detected areas are shown in Green Square.

Table 4-2 Chemical compositions (atom.%) of cations in CMTZAF and Hf-substituted M3 (CMTHAF) detected by SEM-EDS.

	CMTZAF	CMTHAF
Ca	12.5	11.9
Mn	8.2	8.0
Ti	29.8	30.1
Zr/Hf	10.2 (Zr)	11.8 (Hf)
Al	15.3	15.0
Fe	24.0	23.2

**Fig. 4-6** The experimental XRD patterns of CMTZAF and Hf-substituted M3 (CMTHAF) and simulated pattern using Pakhomova's M3 structural parameters with replaced site of only *Ca1* site, Mn and Tb ions.

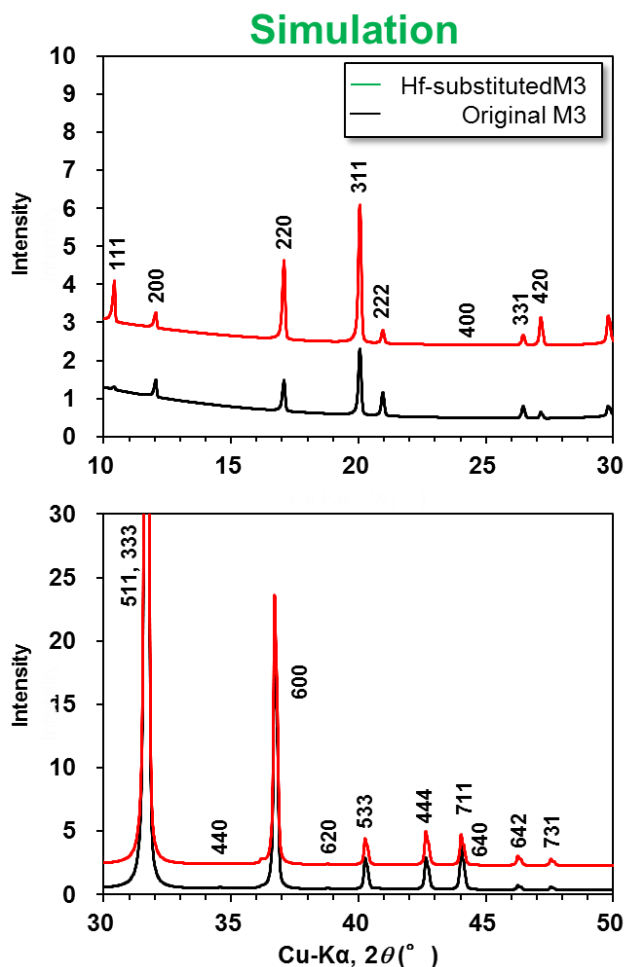


Fig. 4-7 The simulated pattern using Pakhomova's M3 structural parameters with replaced site of TiI site (Zr ion only).

4.3.4 Chemical analysis for transition elements, Fe and Mn ions

It is possible to distinguish Fe and Mn oxidation states using satellite features of Fe2p and Mn2p. In the Fe2p spectra, the satellite peaks at binding energy of 720 eV and 734 eV were observed. The peak at 720 eV is characteristics of Fe (III) Fe2p_{3/2}. MnO also has a satellite feature, which is no present for either Mn₂O₃ or MnO₂. Mn (II) 2p_{3/2} satellite at binding energy of 647 eV was confirmed in the XPS analysis for CMTZAF sample.

As above, confirmed Fe and Mn oxidation states agreed with that already reported in previous report [20-22]. I know that the quantitative determination of Fe²⁺/Fe³⁺ and Mn²⁺/Mn³⁺/Mn⁴⁺ ratios in murataite oxides was difficult in this study, thus, in reference of previous study using XPS, Mössbauer spectroscopy and XANES, the oxidation states of Fe and Mn were determined to be mainly Fe³⁺ and Mn²⁺, respectively. Ca, Zr, Ti and Al in murataite could be distinguished as their typical oxidation state.

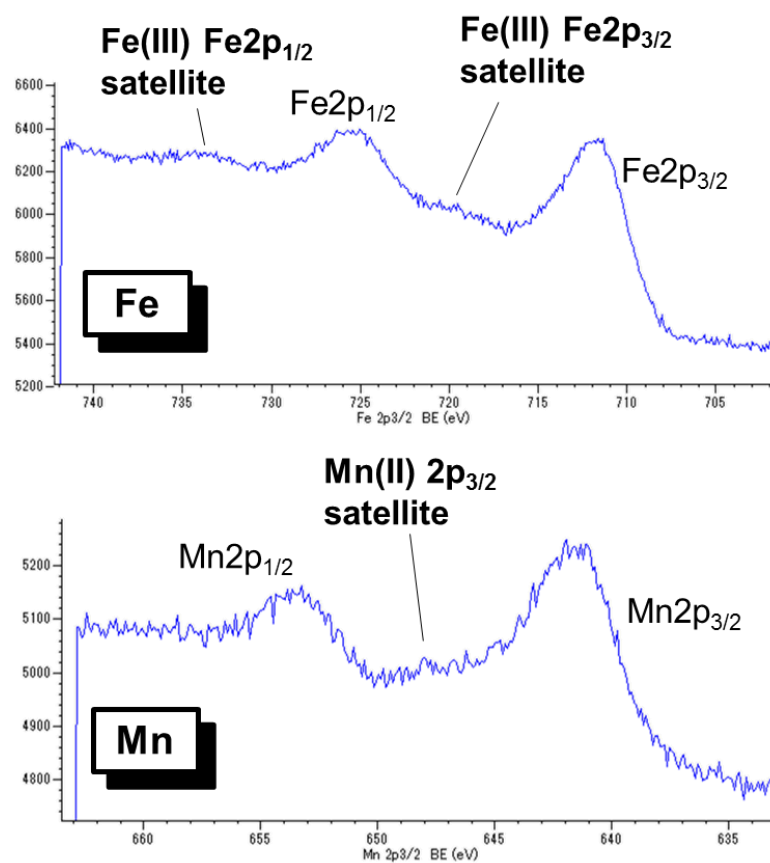


Fig. 4-8 Fe2p and Mn2p spectra for CMTZAF.

4.4 Conclusions

I reported here the crystal structure of M3-type murataite characterized with PXRD and STEM-EELS analysis using the general and simpler M3 samples synthesized by solid-state reaction method. Interestingly, the site preference of Zr ion was slightly different from that reported in previous works; in this study, mainly occupied at *Ca1* site instead of *Ti* site. The technique as shown here, substitution of Hf into Zr site, is very helpful for structural analysis. This approach should be applied to other complex structures including murataite families, M5, M7 and M8.

Surprisingly, HAADF-STEM observation demonstrated that the huge layered defects as observed in Chapter 2 were not confirmed in the phase-pure M3 sample, CMTZAF and CFTZAF. The formation of this enormous defect strongly depends on the synthesis condition of murataite series.

References

- [1] A. S. Pakhomova, S. V. Krivovichev, S. V. Yudintsev, and S. V. Stefanovsky, "Synthetic murataite-3C, a complex form for long-term immobilization of nuclear waste: crystal structure and its comparison with natural analogues," *Z. Kristallogr.*, **228** [3] 151-156 (2013).
- [2] J. W. Adams, T. Botinelly, W. N. Sharp, and K. Robinson, "Murataite, a new complex oxide from El Paso County, Colorado," *Am. Mineral.*, **59** [1-2] 172-176 (1974).
- [3] T. S. Ercit and F. C. Hawthorne, "Murataite, a UB_{12} derivative structure with condensed Keggin molecules," *Can. Mineral.*, **33** [1] 1223-1229 (1995).
- [4] P. E. D. Morgan and F. J. Ryerson, "A new "cubic" crystal compound," *J. Mater. Sci. Lett.*, **1** [8] 351-352 (1982).
- [5] N. P. Laverov, S. V. Yudintsev, B. I. Omel'yanenko, B. S. Nikonov, and S. V. Stefanovskii, "Murataite ceramics for the immobilization of actinides," *Geol. Ore Deposits*, **41** [2] 85-93 (1999).
- [6] S. V. Stefanovsky, S. V. Yudintsev, B. S. Nikonov, B. I. Omelianenko, A. I. Gorshkov, A. V. Sivtsov, M. I. Lapina, and R. C. Ewing, "Pyrochlore-type phases for actinides and rare earth elements immobilization," *Mat. Res. Soc. Symp. Proc.*, **556** [4] 27-34 (1999).
- [7] S. V. Stefanovskii, O. A. Stefanovskaya, S. V. Yudintsev, and B. S. Nikonov, "Phase relationships in systems based on Y, Gd, Mn, Ti, and U oxides with addition of Ca, Al, and Fe oxides," *Radiochemistry*, **49** [4] 354-360 (2007).
- [8] S. V. Stefanovsky, A. G. Ptashkin, O. A. Knyazev, M. S. Zen'kovskaya, O. I. Stefanovsky, S. V. Yudintsev, B. S. Nikonov, and M. I. Lapina, "Melted murataite ceramics containing simulated actinide/rare earth fraction of high level waste," WM2008 Conference, Phoenix, Arizona, 2008, Abstract #8036.
- [9] S. V. Krivovichev, V. S. Urusov, S. V. Yudintsev, S. V. Stefanovsky, O. V. Karimova, and N. N. Organova, "Crystal structure of murataite Mu-5, a member of the murataite-pyrochlore polysomatic series," in: S. V. Krivovichev (Eds.), *Minerals as Advanced Materials II*, Berlin Heidelberg, 2012, pp. 293-304.
- [10] S. V. Stefanovskii, S. V. Yudintsev, B. S. Nikonov, and O. I. Stefanovskaya, "Phase composition of ceramics in systems with oxides of rare-earth elements, manganese, and titanium," *Radiochemistry*, **49** [4] 346-353 (2007).
- [11] A. S. Pakhomova, S. V. Krivovichev, S. V. Yudintsev, and S. V. Stefanovsky, "Polysomatism and structural complexity: Structure model for murataite-8C, a complex crystalline matrix for the immobilization of high-level radioactive waste," *Eur. J. Mineral.*, **28** [1] 205-214 (2016).
- [12] R. S. S. Maki, K. Kobayashi, and Y. Suzuki, "Electrical properties of murataite modules with complex and large-volume fluorite-type superstructures," *Mater. Res. Bull.*, **84** 254-258 (2016).
- [13] R. S. S. Maki, P. E. D. Morgan and Y. Suzuki, "Synthesis and Characterization of a Simpler Mn-free, Fe-rich M3-type Murataite," *J Alloys Compd.*, **698** [25] 99-102 (2017).
- [14] R. D. Shannon, "Revised effective ionic radii and systematic studies of interatomic distances in Halides and chalcogenides," *Acta Crystallogr. A*, **32** [Sep1] 751-767 (1976).
- [15] T. Yamashita and P. Hayes, "Analysis of XPS spectra of Fe^{2+} and Fe^{3+} ions in oxide materials," *Appl. Surf. Sc.*, **254** [8] 2441-2449 (2008).
- [16] M. C. Biesinger, B. P. Payn, A. P. Grosvenor, L. W. M. Lau, A. R. Gerson, R. St. C. Smart, "Resolving surface chemical states in XPS analysis of first row transition metals, oxides and hydroxides: Cr, Mn, Fe, Co and Ni," *Appl. Surf. Sc.*, **257** [7] 2717-2730 (2011).
- [17] I. Uhlig, R. Szargan, H. W. Nesbitt, K. Laajalehto, "Surface states and reactivity of pyrite and marcasite," *Appl. Surf. Sc.*, **179** [1-4] 222-229 (2001).

Chapter 4

- [18] F. Izumi, K. Momma, “Three-dimensional visualization in powder diffraction,” *Solid State Phenom.* **130** 15–20 (2007).
- [19] M. Watanabe, E. Okunishi, and K. Ishizuka, “Analysis of Spectrum-Imaging Datasets in Atomic-Resolution Electron Microscopy,” *Microscopy and Analysis*, **23** 5-7 (2009).
- [20] V. S. Urusov, V. S. Rusakov, S. V. Yudintsev, and S. V. Stefanovsky, “Examination of synthetic murataite structure using data of Mössbauer spectroscopy,” *Mat. Res. Soc. Symp. Proc.*, **807** 243-248 (2004).
- [21] S. V. Yudintsev, S. V. Stefanovsky, B. S. Nikonov, K. I. Maslakov, and A. G. Ptashkin, “Structural characterization of Pu-bearing murataite ceramic,” *J. Alloys Compd.*, **444-445** (2007) 606–609.
- [22] S. V. Stefanovsky, S. V. Yudintsev, B. S. Nikonov, A. A. Shiryayev, “Valence State of manganese, iron and gadolinium in murataite ceramic for immobilization of REE and actinides,” V-th Conf. Radiochemistry-2006, Abstracts, Dubna Russia, October 23-28 2006, pp. 212-213.

Chapter 5

Electrical Properties of Murataite Modules with Complex and Large-Volume Fluorite-type Superstructures

Chapter 5: Electrical Properties of Murataite Modules with Complex and Large-Volume Fluorite-type Superstructures

In this chapter, I have synthesized murataite series with oxygen-deficient fluorite-type superstructures by a solid-state reaction method, and investigated their electrical properties. The multiples of the fluorite-type unit-cell were determined by using X-ray diffraction (XRD) and transmission electron microscope-selected area electron diffraction (TEM-SAED). It revealed that well-crystalized $3\times 3\times 3$ (M3) and $8\times 8\times 8$ (M8) fluorite-type superstructures were successfully synthesized with minor impurities. The calculated lattice constant of the M3 and M8 were 14.589 and 39.269 Å, respectively. Based on four-probe D.C. method and two-probe A.C impedance spectroscopy measurement, the electrical conductivity was measured as functions of temperature and oxygen partial pressure. The electrical conductivities of murataites increased with elevating temperature, which indicated typical semiconducting behavior. Impedance spectra suggest that either electronic or hole conduction must be superior to ionic conduction in M3 phase. The M3 phase demonstrated good thermal stability under oxidizing and reducing atmosphere at 300-700°C.

5.1 Introduction

The research on murataite began in 1978; the natural murataite, now defined as a derivative of the fluorite-type structure, was discovered by Adams *et al.* [1], and the crystal structure of natural murataite was solved ($F\bar{4}3m$, $a = 14.886$ Å, $Z = 4$) [2] and recognized as an anion-deficient $3\times 3\times 3$ fluorite-type superstructure with ordered arrangement of cations [3]. In 1982, Morgan and Ryerson [4] first identified synthetic murataite in complex radwaste ceramics. The crystal structure of the synthetic murataite is very similar to that of the natural murataite, but with a surprisingly very different elemental content, less number of cation vacancies and five symmetrically independent cation site [5,6]. In addition, other murataite modules, $5\times 5\times 5$, $7\times 7\times 7$ and $8\times 8\times 8$ fluorite-type superstructures referred to as M5, M7 and M8, also have been confirmed by transmission electron microscopy (TEM) [7,8]. It is well-known that these superstructures are built up from murataite and pyrochlore structures, and then the detailed crystal structures of M3 and M5 were reported [9,10]. Since the discovery in 1978, 39 years have passed, and various murataite polysomatic series have been confirmed during this period. Their structural analysis have been progressed. However, study on the physical properties of the murataite series has never been done ever.

Murataite ceramics are constituted of various elements including rare-earth and actinide [11,12], which make it difficult to obtain single murataite phase. Furthermore, depending on the synthesis conditions, the cation occupancy of specific sites and the superstructures easily change. As mentioned previous chapters, I have synthesized very complex oxide crystal with an $8\times 8\times 8$ fluorite-type superstructure (M8) with relatively high purities [13]. This modular structure contains $8 \times 8 \times 8 = 512$ basic sub-cells, about 5,250 atoms and 40 distinct symmetry cation positions [10,14]. This crystal structure is considered as the most complex mixed oxide known to date.

In this chapter, I focus on the electrical properties of murataite polysomatic series. Anion-deficient fluorite-related structures, such as yttrium-stabilized zirconia, are well-known as potential important applications, *e.g.* oxygen gas sensors and catalysts [15,16]. In addition to these, the materials with fluorite-type superstructure (*e.g.* pyrochlore) have been investigated for functional materials such as electrolyte of solid oxide fuel cells [17]. The electrical conductivity of murataite series, M3 and M8, under various temperatures and atmospheres are first presented to clarify their electrical conductivity and charge carrier because no report

ever attempted as a functional ceramics despite its unique crystal structure. Furthermore, I discuss the potential applications of murataite ceramics with taking account of their electrical properties, thermal stability and distinct lattice parameters. Murataite structure, M3, and the largest murataite modular structure, M8, were individually obtained by the standard ceramic procedure of co-firing oxides. Unlike conventional procedure, synthesis of murataite samples were carried out without rare-earth element (REE) and actinide, resulting in a low cost and environmentally friendly processing.

5.2 Experimental procedure

5.2.1 Sample preparation

Commercial CaO (99.9% purity, Kojundo Chemical Laboratory Co. Ltd.), MnO₂ (99% purity, Kojundo Chemical Laboratory Co. Ltd.), TiO₂ anatase (99% purity, Kojundo Chemical Laboratory Co. Ltd.), ZrO₂ (98% purity, Kojundo Chemical Laboratory Co. Ltd.), α -Al₂O₃ (99.99% purity, Taimei Chemicals Co. Ltd., Saitama, Japan) and α -Fe₂O₃ (99.9% purity, Wako Pure Chemical Industries Ltd.) powders were used as starting materials. The starting powders were mixed by planetary ball-milling with ZrO₂ media for 30 min (acceleration: 4G). The powder mixtures were sieved through a 150-mesh screen. Cylindrical pellets (diameter of 15 mm) and rectangular specimens (4×6×50 mm) were prepared by the uniaxial cold isostatic pressing of the mixed oxides at 200 MPa for 10 min (Fig. 5-1). The green compacts were then sintered at 1300°C for 30 min (Sample A) and 6 h (Samples B and C) in air in an alumina crucible coated with Pt foil. The compositions and synthesis conditions of murataite samples in the CaO-MnO₂-TiO₂-ZrO₂-Al₂O₃-Fe₂O₃ system are shown in Table 5-1.

Table 5-1 Compositions of murataite samples (in mol.%).

	Samples		
	A	B	C
CaO	14.0	15.1	16.0
MnO ₂	9.3	9.0	7.6
TiO ₂	41.9	41.4	43.9
ZrO ₂	11.2	13.2	16.7
α -Al ₂ O ₃	8.8	8.7	5.8
α -Fe ₂ O ₃	14.9	12.6	10.0



Fig. 5-1 Sintered cylindrical pellet and rectangular specimen for measurements of electrical properties.

5.2.2 Sample characterizations

TEM-SAED pattern of the crushed samples were observed by aberration-corrected transmission electron microscopy (JEOL, JEM-2200FS, operated at 200 kV), in order to discover the superstructure of these particular murataites. The phases in the pulverized samples were analyzed by XRD (Rigaku, Multiflex, counter diffractometer with graphite-monochromatized Cu-K α_{1+2} radiation, operated at 40 kV and 40 mA), using a reflection-free single-crystal silicon stage. A step scan (step: 0.01°) was done in a range of $2\theta = 2-10^\circ$ with judicious masking of the incident beam and background forward scatter. A normal scan (*viz.* without masking) was done in a range of $2\theta = 10-150^\circ$ with the background removed. $K\alpha_2$ lines were removed by the Rachinger algorithm. The lattice constant, a , of the murataite superstructure was calculated using a Nelson–Riley extrapolation. The ICDD-JCPDS database was used for identifying non-murataite phases. Indexing for peaks of murataite phases were carried out based on the superlattice reflections observed from TEM-SAED pattern. The atomic composition on the polished section of the bulk samples were measured by scanning electron microscopy (Hitachi TM3000, operated at 15 kV) equipped with energy dispersive X-ray spectrometry (SEM–EDS).

5.2.3 Methods for measuring the electrical conductivity

For the electrical conductivity measurements, the surface of the samples were polished by waterproof abrasive paper to enhance electrode adhesion. Platinum paste electrodes was attached to the surfaces of sintered samples and then heated up to 1200°C. The electrical conductivity measurement was carried out in air using conventional four-probe D.C. method (34410A, Agilent, Japan). The rectangular sample was positioned in the center of a tubular furnace. The measurement temperature range was from 300 to 1000°C monitored with a K-type thermocouple placed at the vicinity to the sample. Prior to the measurement, the temperature was kept at the target temperature for 20 min to stabilize the sample temperature. In order to confirm the long-term stability, the electrical conductivity was continuously measured every 10 s at 800°C. Before and after 100 h aging, the thermal expansion coefficient (CTE) was measured twice under atmospheric pressure in air by thermomechanical analysis (Thermoplus EVO II, Rigaku, Japan) to determine the influence of microcracks induced by minor impurity phase (pseudobrookite). These microcracks strongly affect the electrical conductivity and thermal expansion coefficient of specimen [18].

Oxygen partial pressure (P_{O_2}) dependence of the electrical conductivity was measured at 300-700°C by combination of the frequency response analyzer (1255, SolarTron, UK) with the potentio/galvanostat (1287, SolarTron, UK) over the frequency ranging from 1 MHz to 0.1 Hz with an A.C. amplitude set at 50 mV under flowing of O $_2$, air, Ar, and Ar-H $_2$ gas mixture under fixed water vapor pressure. Water vapor pressure was controlled by the following step: the sample gas was mixed with water vapor above 40°C, and then the mixed gas was flowing through the Liebig condenser line at 20°C; the water vapor pressure is 0.02 atm ($\log P_{H_2O} = -1.63$).

The oxygen partial pressure of the outlet gas was measured using the zirconia oxygen sensor set at downstream of the conductivity measurement cell. Temperature of the oxygen sensor was fixed about 900°C. In the case of O $_2$, air, and Ar containing of water vapor gaseous, P_{O_2} measured at the oxygen sensor is the same with the P_{O_2} at the vicinity of the sample because no chemical reaction among the gas species were

made. On the other hand, the P_{O_2} measured using the sensor is different from the P_{O_2} at the vicinity of the sample when the sample temperature is different from the sensor temperature using Ar + H₂ + H₂O gas mixture due to the chemical equilibrium among H₂, H₂O and O₂. Hence, the P_{O_2} at the vicinity of the sample under Ar + H₂ + H₂O gas mixture was calculated based on the chemical thermodynamics as following procedures.

The P_{O_2} at the vicinity of the sample was calculated from the thermodynamic data using the following equation:

$$K = \frac{(P_{H_2O})^2}{(P_{H_2})^2 \cdot P_{O_2}}$$

$$\left(\frac{P_{H_2O}}{P_{H_2}}\right)^2 = K_{\text{sensor}} \cdot P_{O_2} (\text{sensor})$$

and

$$P_{O_2} (\text{sample}) = \frac{1}{K_{\text{sample}}} \cdot \left(\frac{P_{H_2O}}{P_{H_2}}\right)^2$$

by monitoring the temperature close to the sample and oxygen sensor. The specimen for the two-probe A.C. impedance measurement was prepared by attaching the platinum paste electrode to both sides of the cylindrical pellet. In order to calculate the conductivity, Z-view software (Scribner Associate Inc., USA) was used for fitting the impedance spectra.

5.2.4. Measurement of electromotive force for evaluation of ionic transport number

For an electromotive force measurement, a test cell was fabricated using a sample in which platinum paste was added at both sides as electrodes. The electromotive force was measured by flowing gas mixture of various oxygen partial pressures (O₂, 20% O₂, Ar, 1% H₂, 10% H₂ and H₂) to the one side of the sample under the atmospheric environment at 700°C.

5.3 Results

5.3.1 Phase identification by XRD and TEM-SAED

XRD (Fig. 5-2, 5-3, 5-4) revealed that all of the samples after sintering had major murataite, minor P, pseudobrookite, and Z, zirconolite phases. Sample A contained only M3 phase and Sample C contained only M8 phase. In Sample B, M3 and M8 phases were confirmed. Most of very weak peaks from the supercell and stronger peaks from the fluorite-type basic sub-cell were clearly observed. TEM-SAED patterns apparently exhibited superlattice reflections of (b) M3 and (c) M8 between basic reflections from fluorite-type sub-cell at 3 and 8 intervals in the (110) plane of the reciprocal lattice, respectively. These results indicate that the samples were well-crystalized. The composition ratios of cations of murataite phases in the Sample A and C detected by SEM-EDS were Al_{12.5}Ca_{12.2}Ti_{35.6}Mn_{7.9}Fe_{21.7}Zr_{10.1} and Al_{9.5}Ca_{13.7}Ti_{38.4}Mn_{6.0}Fe_{15.2}Zr_{17.1}, respectively. The amounts of Fe, Mn and Al elements increased corresponding to the phase transition from M8 to M3. In contrast, Ca and Zr amounts were decreased.

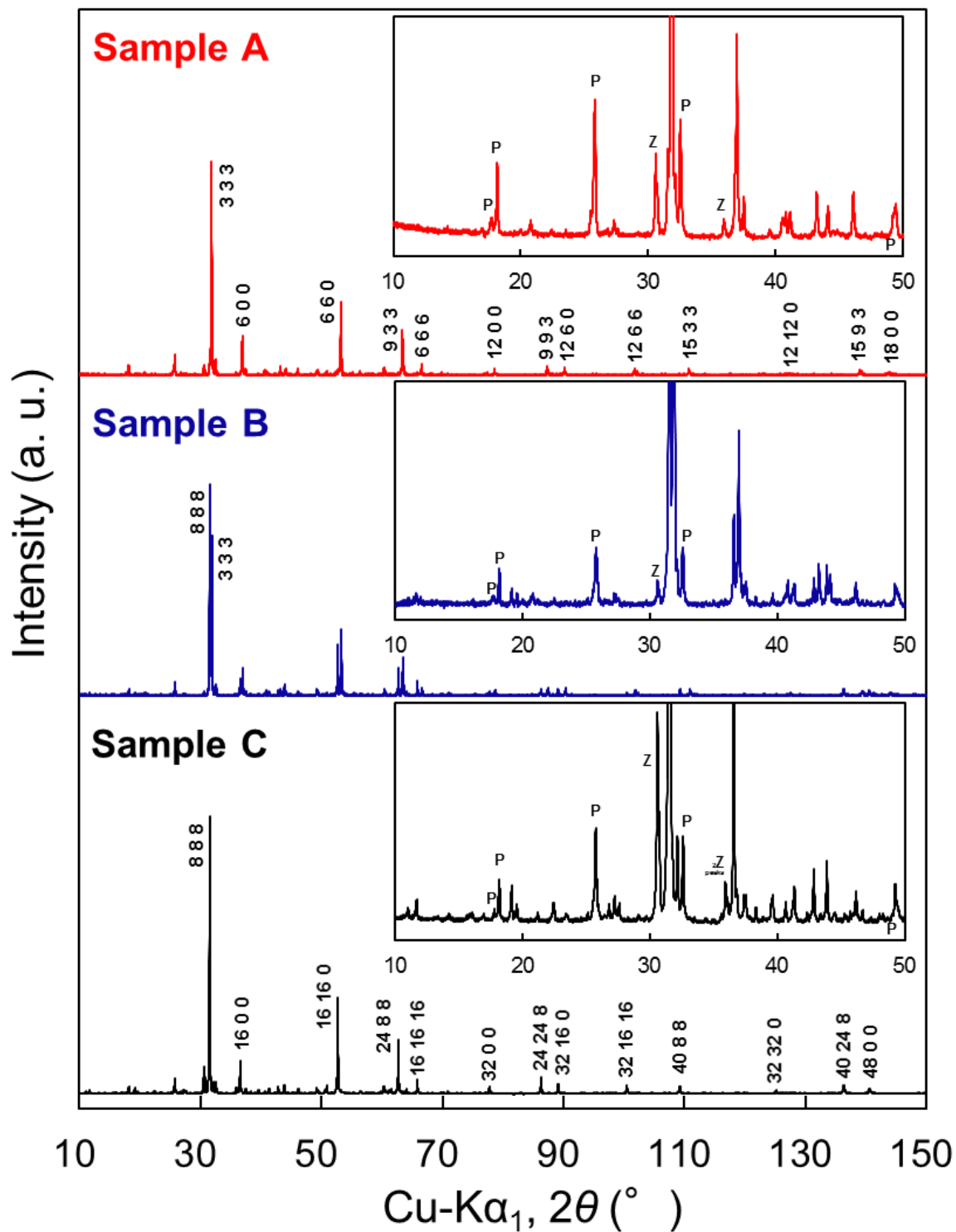


Fig. 5-2 X-ray diffraction patterns of samples prepared with different powder mixtures. Expanded sections of low angle $2\theta=10-50^\circ$ are shown insets. All peaks are murataite phases (M3 in Sample A, M3 and M8 in Sample B, and M8 in Sample C) with minor impurities: P, pseudobrookite and Z, zirconolite.

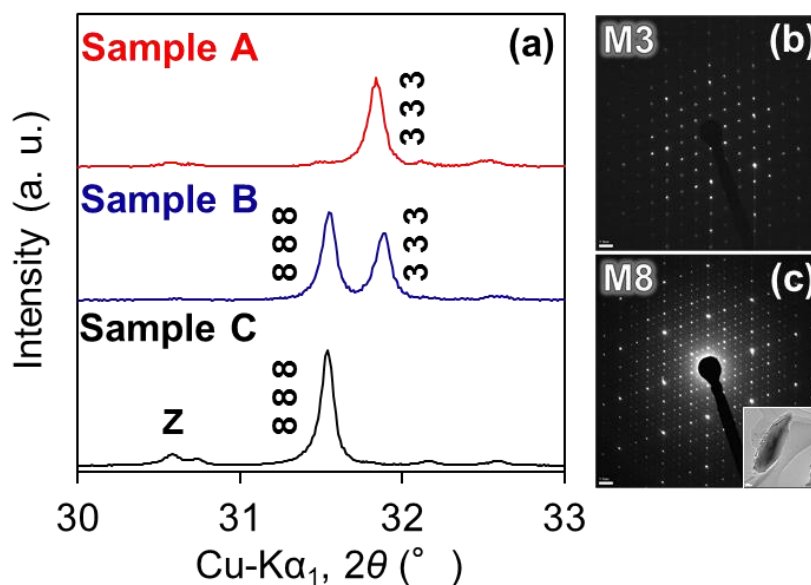


Fig. 5-3 (a) Expanded section of Fig. 5-2, in the region of major M3 and M8 peaks; there are no visible peaks due to M5 or M7. TEM-SAED patterns of (b) M3 and (c) M8 in the (110) plane of the reciprocal lattice are confirmed. Low mag. TEM image from pulverized sample is shown inset in part (c).

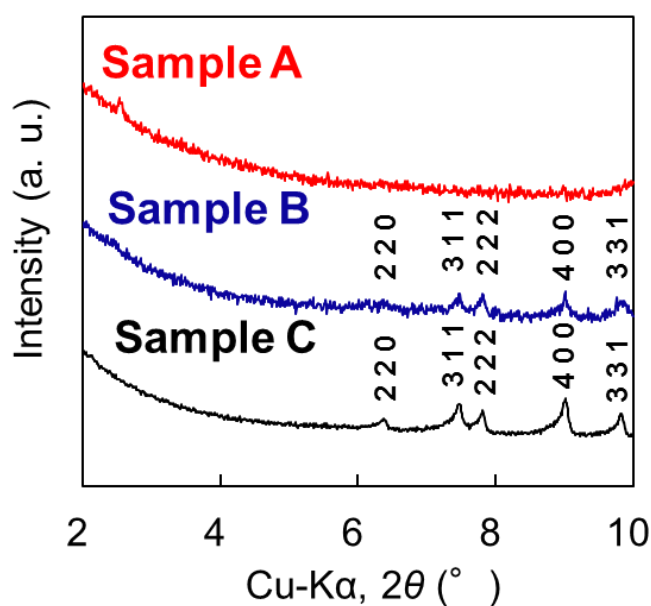


Fig. 5-4 Expanded X-ray diffraction patterns of low angle $2\theta = 2-10^\circ$, emphasizing the many low intensity peaks from the M8 in Sample B and C on a square root scale.

The lattice constants of Samples A and C were calculated by only using the strong certain reflections at high angles [12 0 0, 9 9 3, 12 6 0, 12 6 6, 15 3 3, 12 12 0, 15 9 3 and 18 0 0 in Sample A] and [32 0 0, 24 24 8, 32 16 0, 32 16 16, 24 24 24, 32 32 0, 40 24 8 and 48 0 0 in Sample C], which were from the fluorite-type basic sub-cell. The lattice constant of the M3 and M8 were 14.589 ± 0.0001 and 39.269 ± 0.0001 Å, respectively. In Sample A, the lowest angle peak, 1 1 1, was observed at around $2\theta = 10^\circ$ which is closed to that of natural murataite, *i.e.* M3 [1]. The detailed indexing result for M8 was described in Chapter 2 [13].

5.3.2 Electrical conductivities of M3- and M8-type murataite

Temperature dependence of the electrical conductivity for each specimen determined by four-probe D.C. method is shown in Fig. 5-5. The electrical conductivities for all samples increased with elevating temperature, which indicated typical semiconducting behavior. The electrical conductivities of Samples A, B and C were $3.46 \times 10^{-2} \text{ S}\cdot\text{cm}^{-1}$, $1.95 \times 10^{-2} \text{ S}\cdot\text{cm}^{-1}$ and $0.62 \times 10^{-2} \text{ S}\cdot\text{cm}^{-1}$ at 800°C , respectively. The electrical conductivity increased with phase transition from M8 to M3, and exhibited the increase tendency according to the amounts of Fe and Mn elements. In this study, Sample A exhibited the highest conductivity.

Annealing time dependence of Samples A, B and C on the electrical conductivity at 800°C are shown in Fig. 5-6. The magnitudes of the conductivity degradation of the Samples A, B and C by the annealing for 100 h at 800°C were -2.3 , -2.6 and -16.8% , respectively. Sample A, which mainly contained M3, exhibited the smallest decrease in conductivity. In XRD results, the peaks from the supercell and basic sub-cell of M3 and M8 did not change before and after 100 h aging (Fig. 5-7), which exhibited the long-term stability of M3 and M8 phases at 800°C . A drastic reduction of electrical conductivity due to phase transition/decomposition was not found.

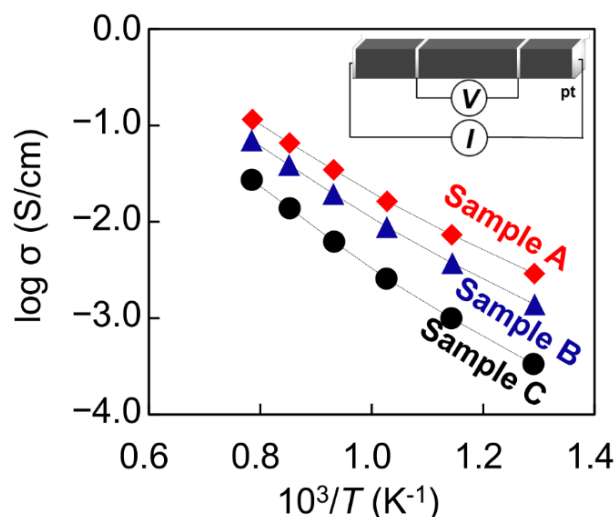


Fig. 5-5 Temperature dependence of the electrical conductivities determined by four-probe D.C. method. The dot lines are guides to the eye.

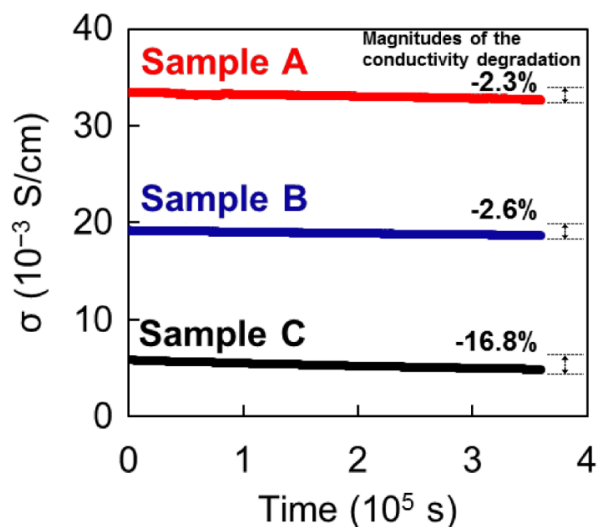


Fig. 5-6 Annealing time dependence on the electrical conductivity measured at 800°C for $3.6 \times 10^5 \text{ s}$ (100 h).

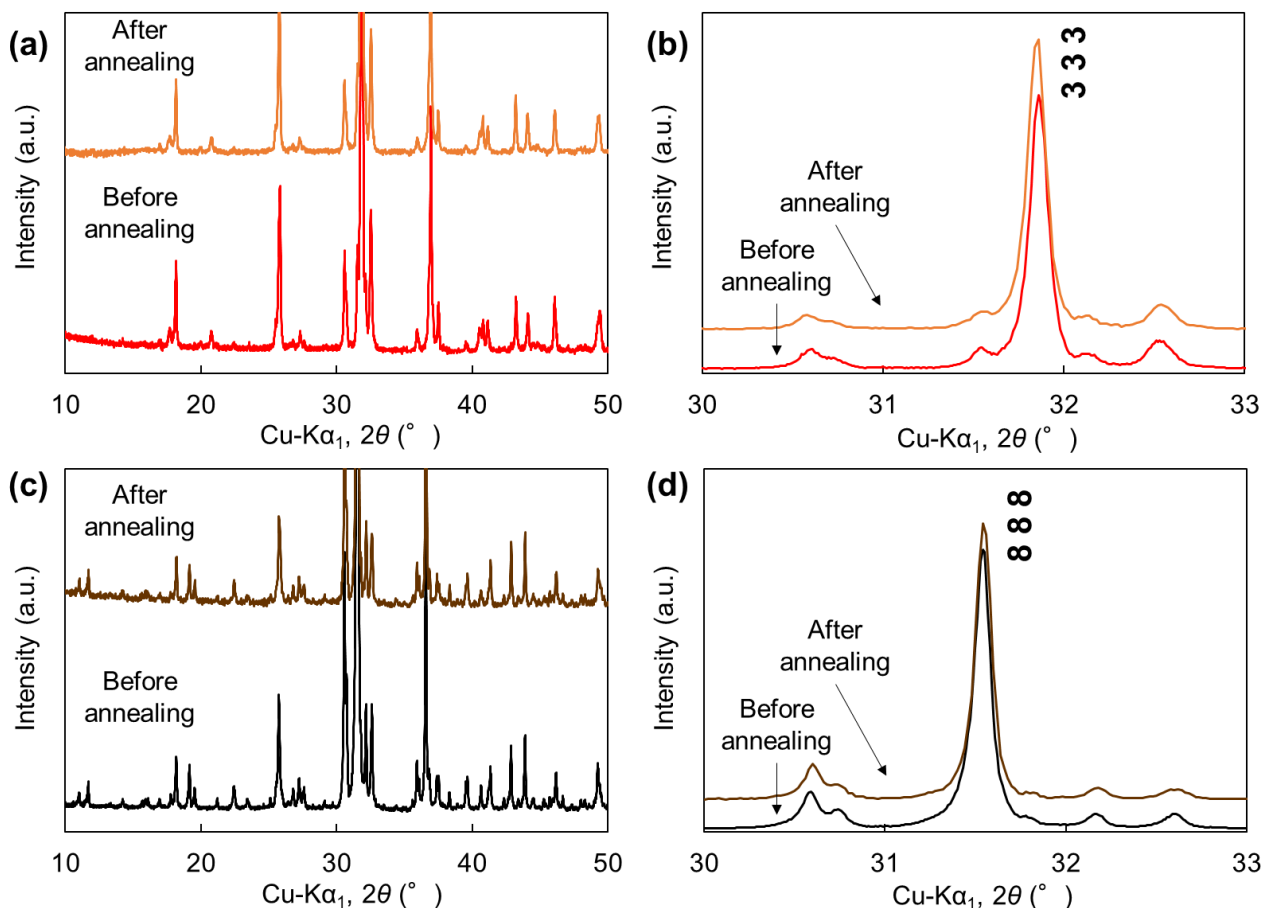


Fig. 5-7 (a) X-ray diffraction patterns obtained from each specimen before and after annealing at 800°C for 100 h: (a) $2\theta = 10\text{-}50^\circ$ and (b) the region of 3 3 3 in Sample A; (c) $2\theta = 10\text{-}50^\circ$ and (d) the region of 8 8 8 in Sample C. The peaks from the supercell and basic sub-cell of M3 and M8 did not change before and after 100 h annealing.

Based on my previous study [18], the influence of microcracks induced by anisotropic thermal expansion of pseudobrookite phase during annealing were evaluated by thermomechanical analysis. The CTE before and after 100 h aging were 8.21×10^{-6} and 8.31×10^{-6} /K (Sample A), and 8.55×10^{-6} and 8.58×10^{-6} /K (Sample C) from RT to 800°C, respectively (Fig. 5-8). These results indicate that CTE is not sensitive to the annealing at 1073 K. The result of thermomechanical analysis suggested slight microcracks induced from pseudobrookite phase; the influence of microcracks on the magnitudes of the conductivity degradation most likely be negligible for Sample A and C.

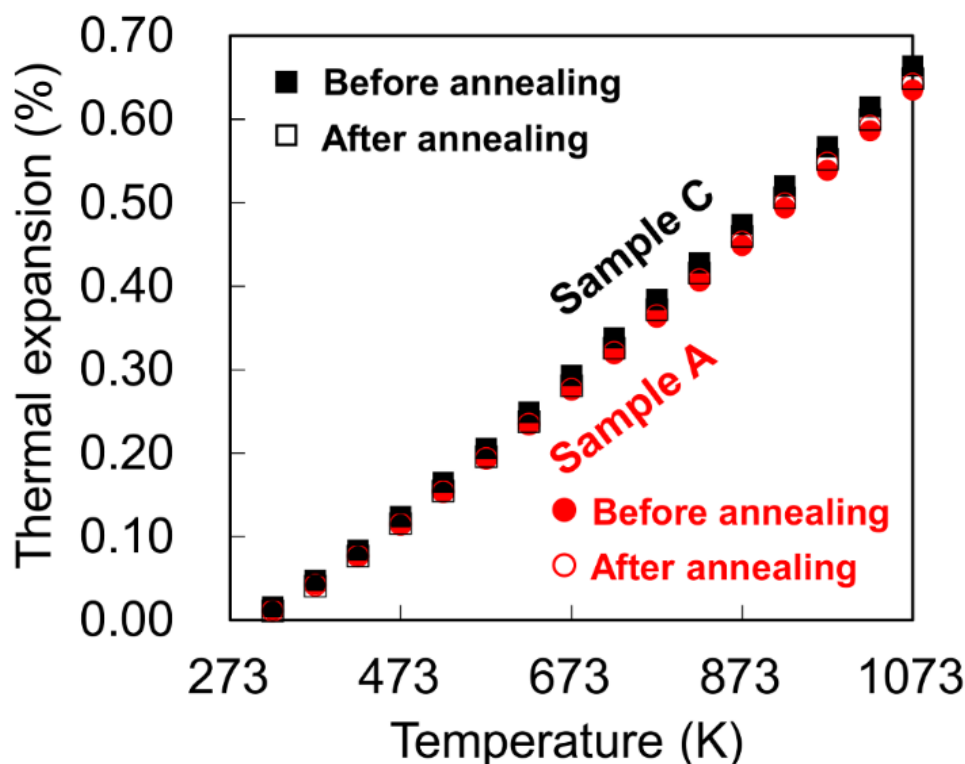


Fig. 5-8 The CTE of sample A (circles) and C (squares) before and after 100 h aging at 800°C.

5.3.3 Dependence of electrical conductivity on oxygen partial pressure

Dependence of the electrical conductivity for Sample A, which mainly contains M3 phase, on oxygen partial pressure is shown in Fig. 5-9. At 300-400°C, the electrical conductivity was almost independent of P_{O_2} under oxidizing and reducing atmosphere. However, in the temperature range of 500-700°C, conductivity slightly increased with decreasing oxygen partial pressure, and impedance spectra did not depend on the frequency range (I was unable to differentiate between the bulk and grain boundary resistance from the impedance spectra); these two findings noticeably suggest that either electronic or hole conduction must be superior to ionic conduction in M3 phase. The impedance spectra according to each resistance component such as grain, grain-boundary and electrode were not separately confirmed. On the other hand, the reduction of conductivity due to the phase transition/decomposition was not found, which demonstrates the durability of M3 phase under oxidizing and reducing atmosphere. In this study, M3 phase did not perform the oxygen ionic conduction behavior in spite of quite similar crystal structure to anion-deficient fluorite-type ceramics. It is likely attributed to no mobile oxygen vacancies (ions); both of the cations and oxygen vacancies are ordered. This suggests the possibility to enhance the oxygen ionic conductivity by inducing structural disordering and dissociation of cation-vacancy interactions, *e.g.* ion-beam irradiation [19], allowing the oxygen vacancy to migrate freely.

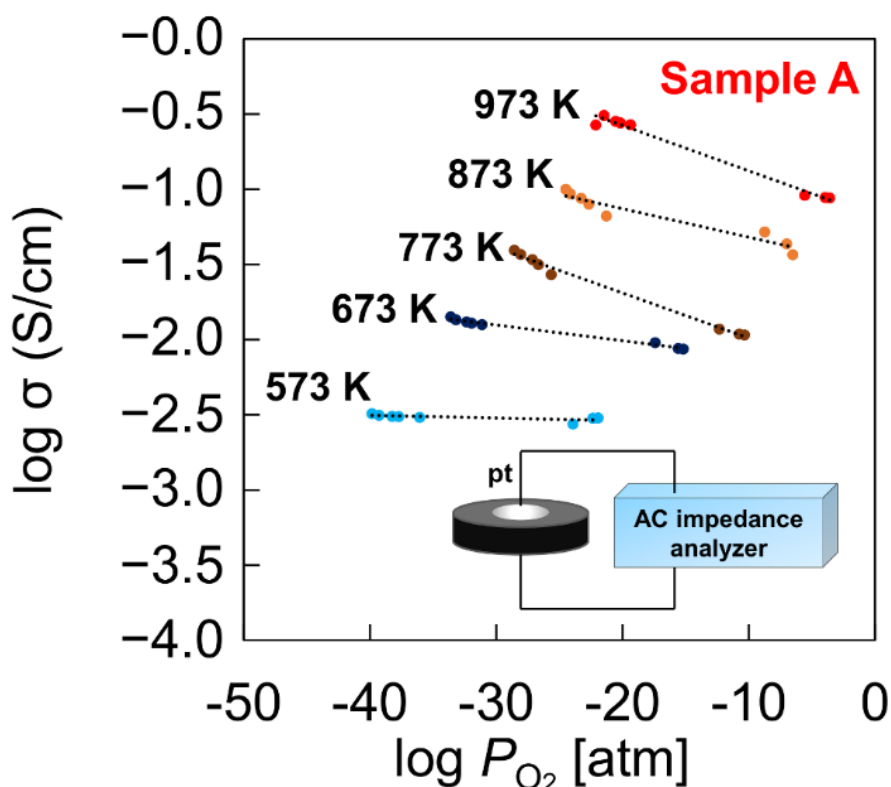


Fig. 5-9 Dependence of electrical conductivity on oxygen partial pressure measured by two-probe A.C. impedance spectroscopy measurement.

5.3.4 Measurement of electromotive force

As a result of measuring the electromotive force of the test cell, occurrence of electromotive force was not confirmed in any oxygen partial pressure atmosphere, resulting that oxygen ionic transport number of M3 is very low. This result is consistent with the result confirmed by the impedance measurement, which confirms the superiority of electron or hole conduction.

5.4 Discussion

5.4.1 Potential application of murataite as functional ceramics

Due to the electrical properties and thermal stability of these complex and giant structure, thermoelectric material appeared to be a potential application of murataite ceramics for use at high temperature. To evaluate the attractiveness of compound as thermoelectric materials, the figure of merit $Z = \sigma \alpha^2 / \kappa$ is important, where σ is the electrical conductivity, α is Seebeck coefficient, and κ is the thermal conductivity. One key parameter in the design of a thermoelectric material is the Seebeck coefficient, which strongly depends on carrier

concentration. Based on classical semiconductor physics and experimental results, $\sigma\alpha^2$ shows maximum value when the absolute value of the Seebeck coefficient is about 200 $\mu\text{V/K}$ [20]. Therefore, the design of thermoelectric material with controllable carrier concentration is important to optimize the thermoelectric efficiency. In murataite structure, cation substitutions typically occur, *e.g.* $\text{Ti}^{4+} = \text{Zr}^{4+}$, $\text{Al}^{3+} = \text{Fe}^{3+}$, $2\text{Ca}^{2+} = \text{Na}^+ + \text{REE}^{3+}$ and $2\text{Ti}^{4+} = (\text{Al}, \text{Fe})^{3+} + \text{Nb}^{5+}$; various elements are incorporated into murataite structure [6,19]. Its wide selectable elements make it easy to control the carrier concentration. In addition to this, the material including magnetic elements, such as Fe and Mn, shows increase in Seebeck coefficient below the Neel temperature due to the magnetic phase transition between the paramagnetic phase and antiferromagnetic phase [21]. Murataite ceramics is expected to show this phenomenon by handling the constituent elements.

Since semiconductor basically has small carrier concentration, the phonon conductivity (κ_L) is important, and hence, small κ_L / σ ratio is required. It is reported that superstructure typically exhibits very small κ_L because of its structural complexity. Tamura *et al.* [22] and Simkin *et al.* [23] pointed out the dramatic reduction of thermal conductivity in the superstructure due to the flattening of the dispersion of curves associated with Brillouin zone folding in the growth direction of periodic superlattice. As revealed by XRD and TEM in this work, murataite series are also constituted of enormous and complex superstructures, and their multiplicity of superstructure is controllable by synthesis condition and atomic composition. High-resolution TEM observation clearly exhibited the periodic atomic-layers with various sizes depending on the multiples of the fluorite-type unit-cell [14]. Due to the complex structure and very extensive cation substitutions in murataite, I predict the drastic enhancement of the physical properties of murataite ceramics by controlling the intrinsic structural modules and constituent elements.

5.5 Conclusions

In the present chapter, I have studied the electrical properties of members of the pyrochlore-murataite modular family with $3 \times 3 \times 3$ and $8 \times 8 \times 8$ superstructures of a fluorite-type sub-cell.

- (1) Well-crystallized M3 and M8 superstructures have been synthesized with minor impurities by solid-state reaction method. The calculated lattice constants of the M3 and M8 were 14.589 and 39.269 Å, respectively.
- (2) The electrical conductivities for murataite series increased with elevating temperature, which indicated typical semiconducting behavior. Sample A, mainly containing M3, exhibited the highest conductivity. The components of Fe and Mn elements seem to be responsible for increase in the conductivities of murataite ceramics rather than the phase transition from M8 to M3.
- (3) M3 phase demonstrated good thermal stability under oxidizing and reducing atmosphere at 300-700°C. In air, the superstructure was stable up to 1000°C. The dependence on oxygen partial pressure revealed that electronic or hole conduction must be superior to ionic conduction in M3 phase. Present study suggested a potential application of murataite ceramics for the thermoelectric material due to the structural complexity and extensive selectable constituent elements.

To view whole investigation described in this Chapter, please visit <http://dx.doi.org/10.1016/j.materresbull.2016.08.016> [24].

References

- [1] J. W. Adams, T. Botinelly, W. N. Sharp, and K. Robinson, "Murataite, a new complex oxide from El Paso County, Colorado," *Am. Mineral.*, **59** [1-2] 172-176 (1974).
- [2] T. S. Ercit and F. C. Hawthorne, "Murataite, a UB_{12} derivative structure with condensed Keggin molecules," *Can. Mineral.*, **33** [1] 1223-1229 (1995).
- [3] S. V. Krivovichev, S. V. Yudintsev, S. V. Stefanovsky, N. I. Organova, O. V. Karimova, and V. S. Urusov, "Murataite-pyrochlore series: A family of complex oxides with nanoscale pyrochlore clusters," *Angew. Chem. Int. Ed.*, **49** 9982-9984 (2010).
- [4] P. E. D. Morgan and F. J. Ryerson, "A new "cubic" crystal compound," *J. Mater. Sci. Lett.*, **1** [8] 351-352(1982).
- [5] P. E. D. Morgan, A. B. Harker, and J. F. Flintoff, "Developments in SRP "composite" defense ceramic radwaste forms," in: G. G. Wicks, W. A. Ross (Eds.), *Nuclear Waste Management*, Am. Ceram. Soc., Columbus, OH, 1984, pp. 234-246.
- [6] A. S. Pakhomova, S. V. Krivovichev, S. V. Yudintsev, and S. V. Stefanovsky, "Synthetic murataite-3C, a complex form for long-term immobilization of nuclear waste: crystal structure and its comparison with natural analogues," *Z. Kristallogr.*, **228** [3] 151-156 (2013).
- [7] O. V. Karimova, N. I. Organova, and V. G. Balakirev, "Modulation in the murataite structure," *Crystallogr. Rep.*, **47** [6] 957-960 (2002).
- [8] N. P. Laverov, S. V. Yudintsev, S. V. Stefanovskii, B. I. Omel'yanenko, and B. S. Nikonov, "Murataite matrices for actinide wastes," *Radiochemistry*, **53** [3] 229-243 (2011).
- [9] S. V. Krivovichev, V. S. Urusov, S. V. Yudintsev, S. V. Stefanovsky, O. V. Karimova, and N. N. Organova, "Crystal structure of murataite Mu-5, a member of the murataite-pyrochlore polysomatic series," in: S. V. Krivovichev (Eds.), *Minerals as Advanced Materials II*, Berlin Heidelberg, 2012, pp. 293-304.
- [10] N. P. Laverov, V. S. Urusov, S. V. Krivovichev, A. S. Pakhomova, S. V. Stefanovsky, and S. V. Yudintsev, "Modular nature of the polysomatic pyrochlore-murataite series," *Geol. Ore Deposits*, **53** [4] 273-294 (2011).
- [11] N. P. Laverov, S. V. Yudintsev, B. I. Omel'yanenko, B. S. Nikonov, and S. V. Stefanovskii, "Murataite ceramics for the immobilization of actinides," *Geol. Ore Deposits*, **41** [2] 85-93 (1999).
- [12] S. V. Yudintsev, S. V. Stefanovsky, B. S. Nikonov, K. I. Maslakov, and A. G. Ptashkin, "Structural characterization of Pu-bearing murataite ceramic," *J. Alloys Compd.*, **444-445** (2007) 606-609.
- [13] R. S. S. Maki, Peter E. D. Morgan, and Y. Suzuki, "X-ray powder diffraction characterization of the large volume unit-cell of the M8 murataite polytype," *Powder Diffr.*, **31** [1] 8-15 (2016).
- [14] N. P. Laverov, S. V. Yudintsev, S. V. Stefanovskii, B. I. Omel'yanenko, and B. S. Nikonov, "Murataite as a universal matrix for immobilization of actinides," *Geol. Ore Deposits*, **48** [1] 335-356 (2006).
- [15] Z. Y. Can, H. Narita, J. Mizusaki, and H. Tagawa, "Detection of carbon monoxide by using zirconia oxygen sensor," *Solid State Ionics*, **79** 344-348 (1995).
- [16] J. B. Goodenough and R. N. Castellano, "Defect pyrochlores as catalyst supports," *J. Solid State Chem.*, **44** [1] 108-112 (1982).
- [17] T. Hagiwara, H. Yamamura, K. Nomura, and M. Igawa, "Relationship between crystal structure and oxide-ion conduction in $Ln_2Zr_2O_7$ ($Ln = Eu, Nd$ and La) system deduced by neutron and X-ray diffraction," *J. Ceram. Soc. jpn.*, **121** [1410] 205-210 (2013).
- [18] R. S. S. Maki and Y. Suzuki, "Mechanical strength and electrical conductivity of reactively-sintered

- pseudobrookite-type $\text{Al}_2\text{TiO}_5\text{-MgTi}_2\text{O}_5$ solid solutions,” *J. Ceram. Soc. Jpn.*, **124** [1] 1-6 (2016).
- [19] J. Lian, L. M. Wang, R. C. Ewing, S. V. Yudintsev, and S. V. Stefanovsky, “Ion-beam-induced amorphization and order-disorder transition in the murataite structure,” *J. Appl. Phys.*, **97** [11] 113536 (2005).
- [20] R. W. Ure Jr. and R. R. Heikes, “Thermoelectricity: Science and engineering,” R. R. Heikes, R. W. Ure Jr., Interscience, New York, 1961 pp. 339.
- [21] K. Kobayashi, M. Nishioka, K. Sato, T. Inoue, S. Hamakawa, T. Tsunoda, T. Higuchi, and S. Yamaguchi, “Anomalous temperature dependence of the thermoelectric power for $\text{Ln}_{0.9}\text{Sr}_{0.1}\text{FeO}_{3-\delta}$ (Ln = La and Nd),” *Trans. Mater. Soc. Jpn.*, **31** [4] 903-906 (2006).
- [22] S. Tamura, Y. Tanaka, and H. J. Maris, “Phonon group velocity and thermal conduction in superlattices,” *Phys. Rev. B*, **60** [4] 2627-2630 (1999).
- [23] M. V. Simkin and G. D. Mahan, “Minimum thermal conductivity of superlattices,” *Phys. Rev. Lett.*, **84** [5] 927-930 (2000).
- [24] R. S. S. Maki, K. Kobayashi, and Y. Suzuki, “Electrical properties of murataite modules with complex and large-volume fluorite-type superstructures,” *Mater. Res. Bull.*, **84** 254-258 (2016).

Chapter 6

Summary and Conclusions

Chapter 6: Summary and Conclusions

Murataite series, firstly found as natural mineral, are considered to be $3\times 3\times 3$ fluorite-related ceramics of very rare case of a 3D polysomatic structure constructed from two parent frameworks. Recent works developed the structural investigation of the synthetic murataite series, and some structural families have been discovered, $5\times 5\times 5$ (M5), $7\times 7\times 7$ (M7), $8\times 8\times 8$ (M8). An interesting possibility is that murataite ceramics may exist as a yet undiscovered (rare) mineral, including its crystal structure, properties and future (possible) applications.

In this thesis, the author presented new findings of murataite series throughout characterizations using the synthetic murataite of M3 and M8 prepared by solid-state reaction method without actinide/REE. This approach produced the proper samples to clarify the structural features of murataite ceramics. The author first reported their electrical properties in detail. Several excellent approaches, which should be applied to other very complex polytypes such as murataite family, were also noted in this thesis. The main conclusions throughout this study are summarized as follows.

In Chapter 2, the synthetic murataite series, M3 and M8, were synthesized by solid-state reaction without actinide and REE. A pure M8 phase was successfully fabricated, and characterized by careful powder X-ray diffraction technique. HAADF-STEM observation of M3 discovered a layered defect having a periodicity much larger than the lattice constant and localization of Zr ion; this finding was not reported in previously produced murataite ceramics.

As for the PXRD characterization of the large-volume unit cell of the M8 murataite (I believe the largest volume unit-cell oxide ever studied), the existence of only $(h\ k\ 0)$ peaks, where $h + k = 4n$, as confirmed by synchrotron data, suggests that M8 most likely belongs to the space group $Fd\bar{3}m$ (227) based on statistical analysis of the structural database. Synchrotron methods are the most accurate and probably necessary from now on in this area.

In Chapter 3, I reported the first finding of a Mn-free, Fe-rich M3-type murataite; interestingly, it contains much Fe. While formerly this family of polytypes were classified as titanates, now I have added high iron members; the new M3 phase has much more Al and Fe cations than Ti. The samples in the system of Ca-Ti-Zr-Al-Fe-O and Ca-Mn-Ti-Zr-Al-Fe-O consist of three-fold fluorite-type face-centered cubic superstructures, which now only have 5 cations, Ca, Ti, Zr, Al, and Fe; this simpler M3 will necessarily simplify structural investigations of these complex synthetic versions of the murataite-pyrochlore polysomatic series.

In Chapter 4, the crystal structure of M3-type murataite was characterized with simpler M3 samples. I have tried to analyze the site preference of Zr ion by substituting Hf ion into the Zr site. The technique, as here, was very helpful for structural analysis; this approach should be applied to other complex structures including murataite families, M5, M7 and M8. Interestingly, the site preference of Zr ion was slight different from that reported in other works; mainly occupied at *Ca1* site instead of *Ti* site previously reported.

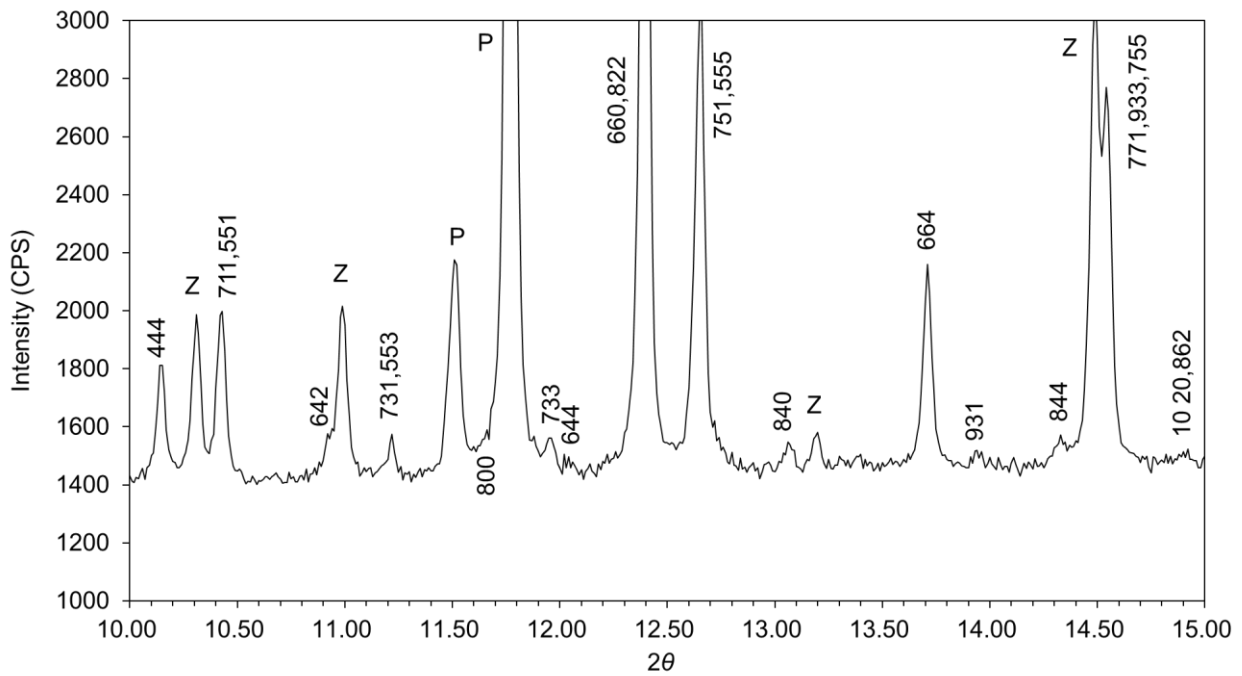
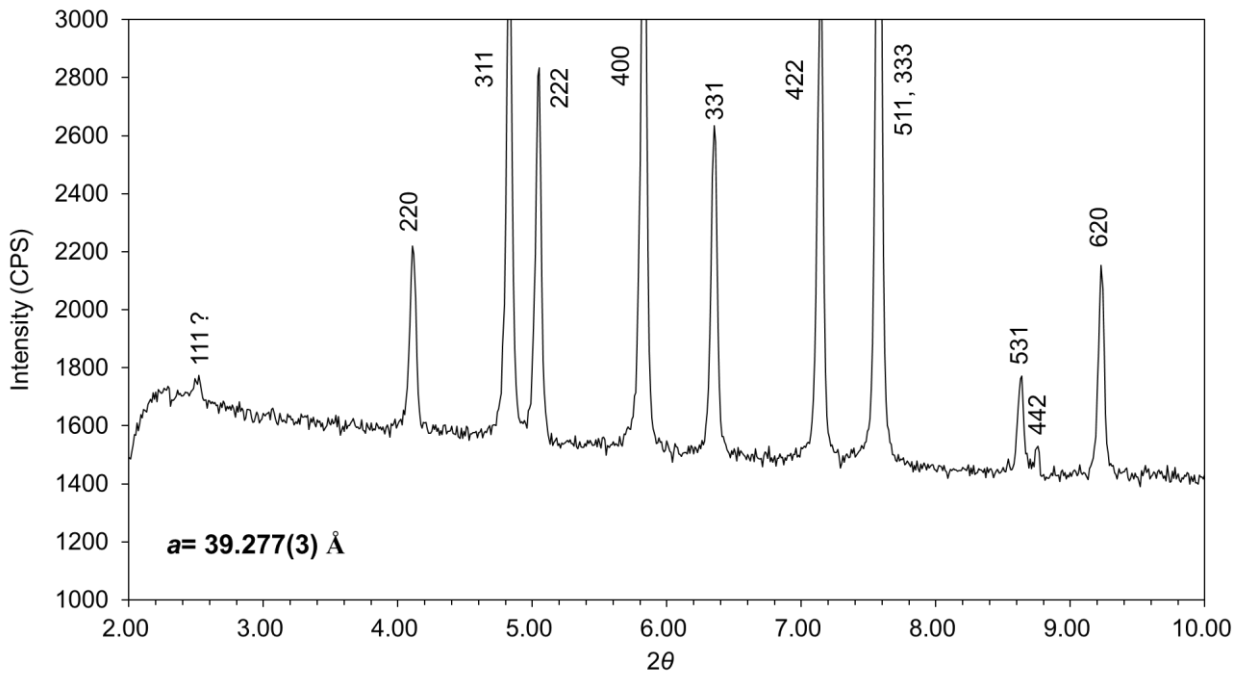
In addition to this, HAADF-STEM observation demonstrated that the dependence of the formation of the huge layered defects on the synthesis conditions of murataite series.

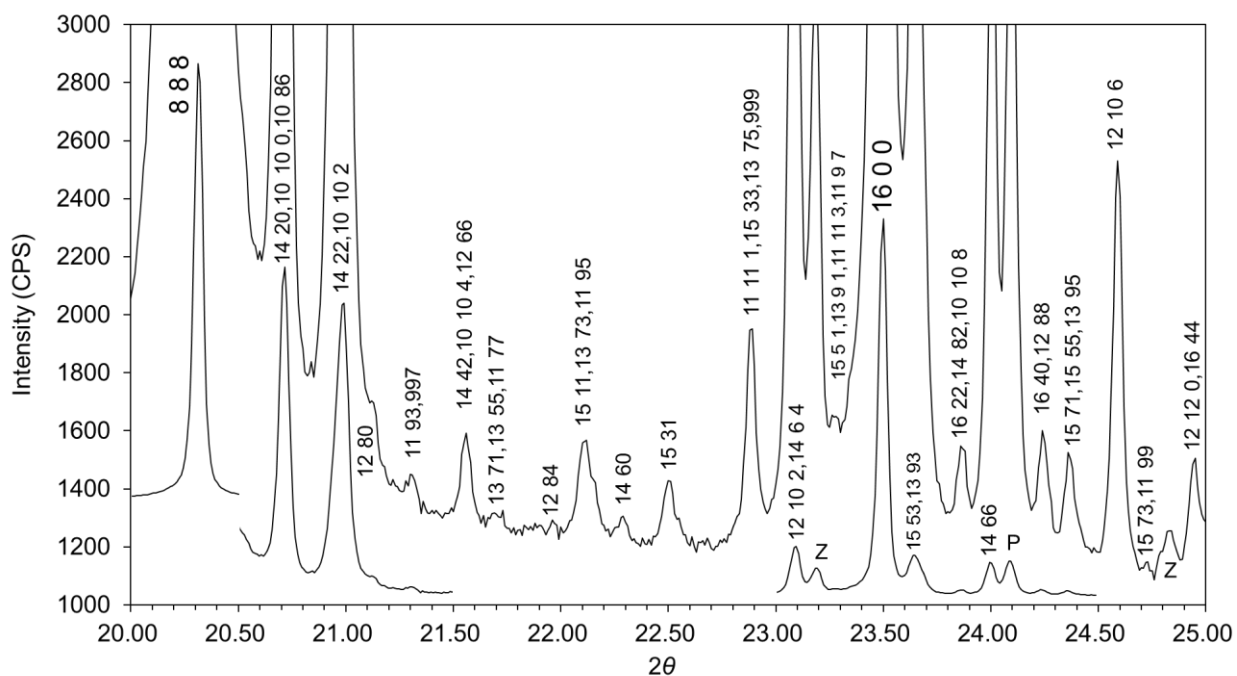
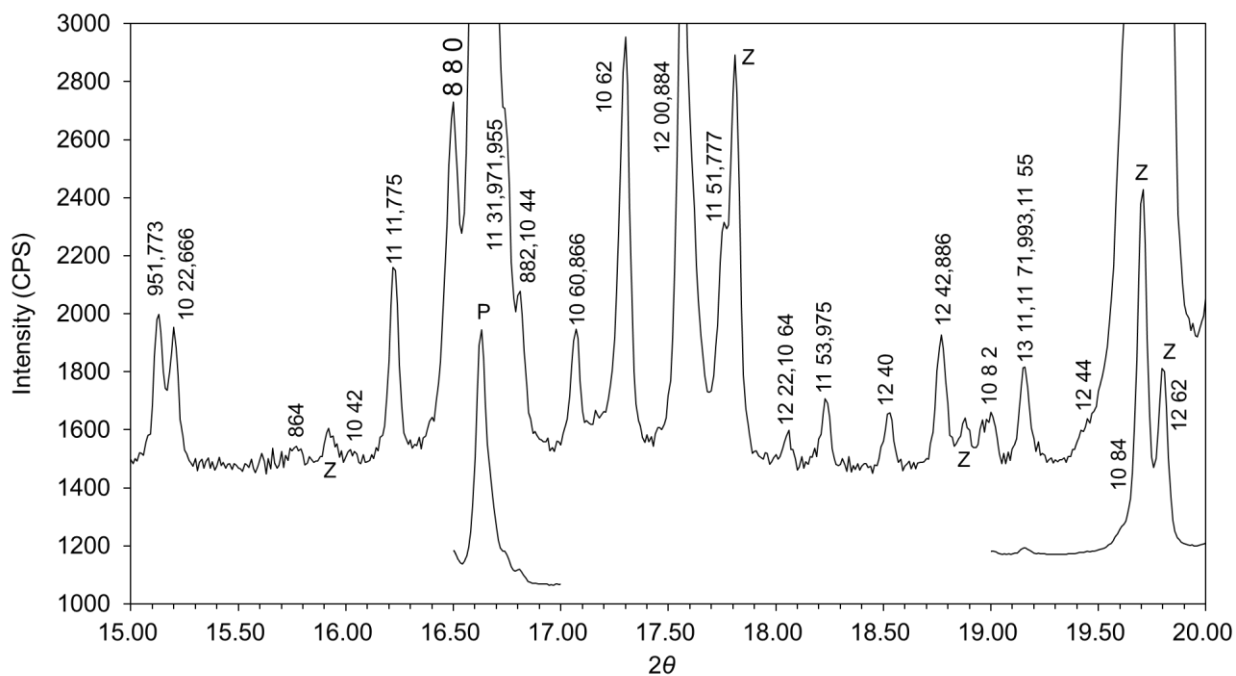
In Chapter 5, I have first studied the electrical properties of murataite series. The electrical conductivities of murataite ceramics increased with elevating temperature, which indicated typical semiconducting behavior. A M3 sample exhibited the higher electrical conductivity than M8 likely due to the higher components of Fe and Mn elements in M3. The dependence of electrical conductivity on oxygen partial pressure revealed that electronic or hole conduction must be superior to ionic conduction in M3.

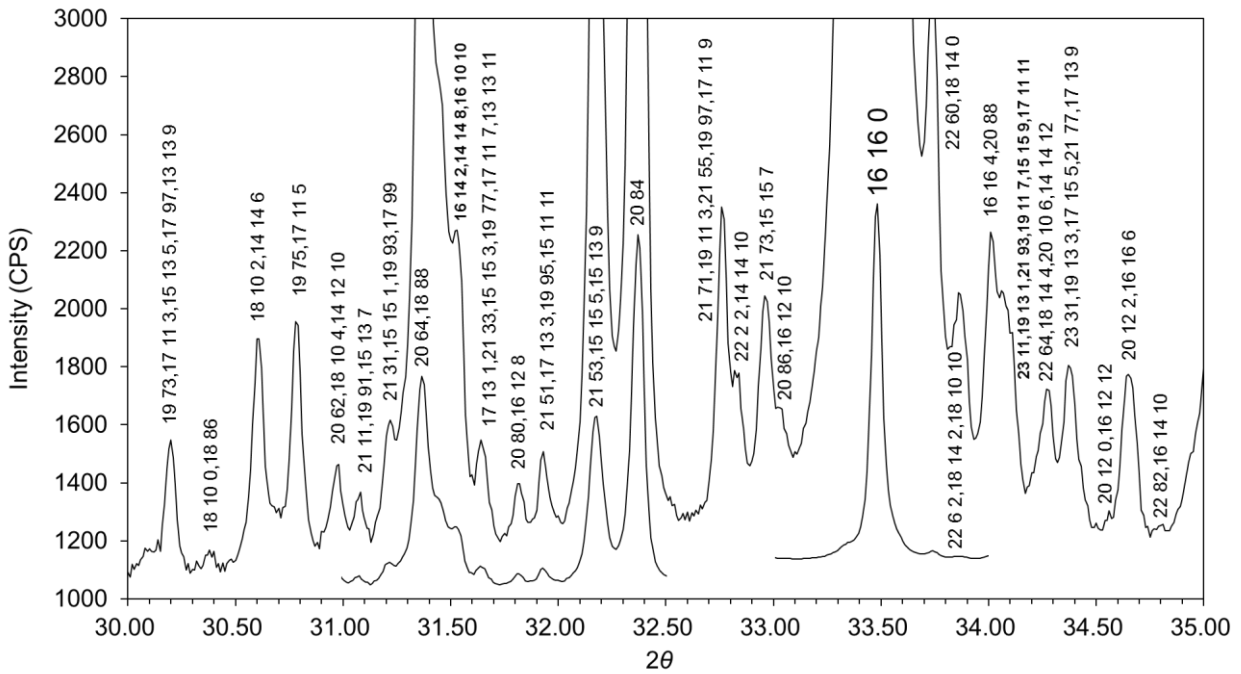
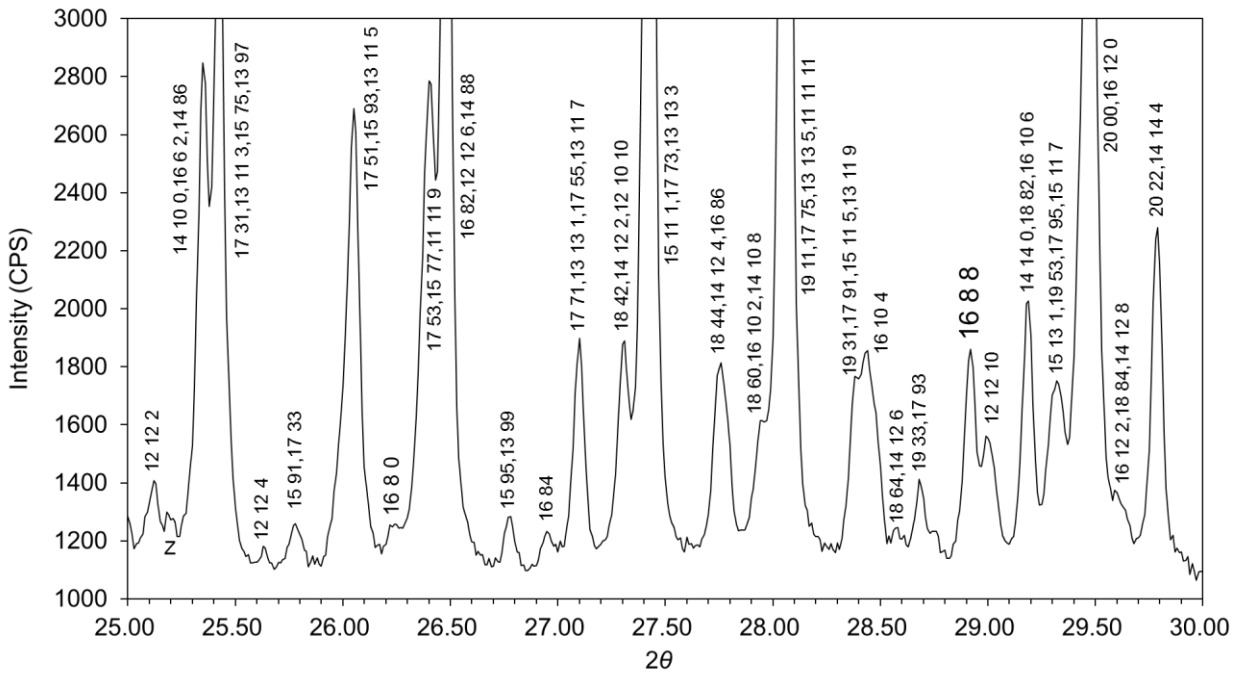
As a whole, some new findings of murataite ceramics were reported here. The author believes that further development of these complex oxide materials could only come from careful studies as described in this thesis. These works are mandatory for the investigation of the murataite series. Finally, the author wishes that the new discovery and approaches proposed in this thesis will necessarily, strongly support the future investigations for these complex synthetic murataite polysomatic series.

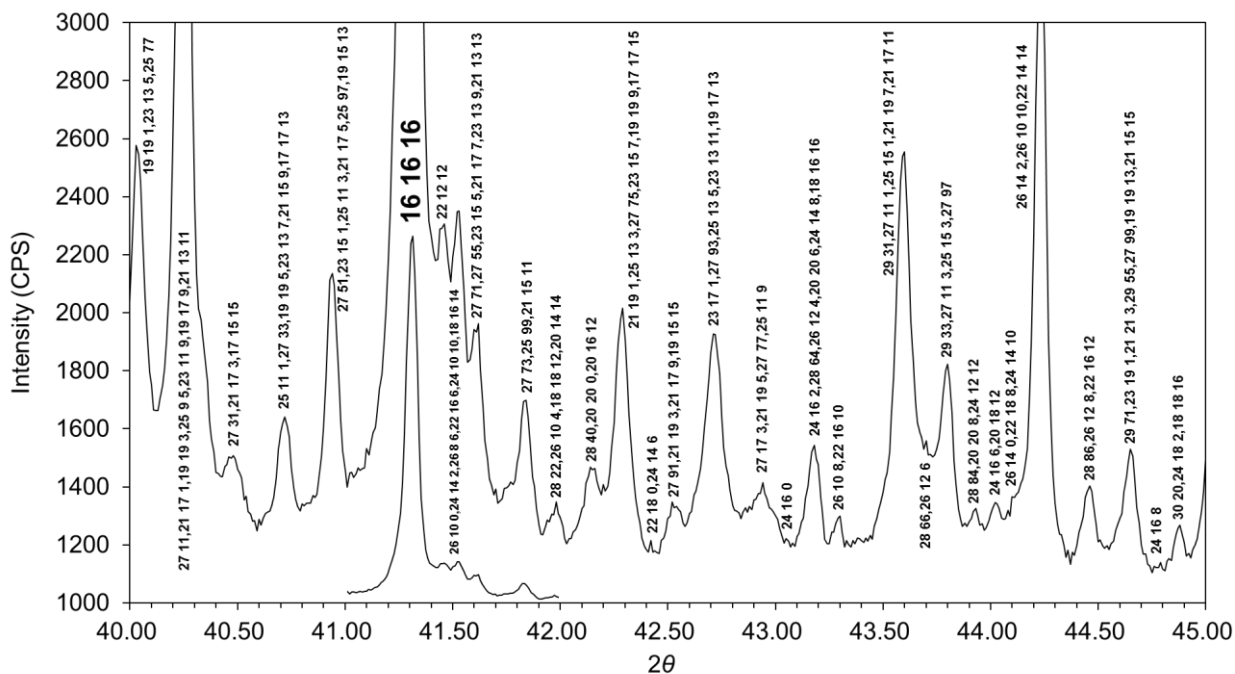
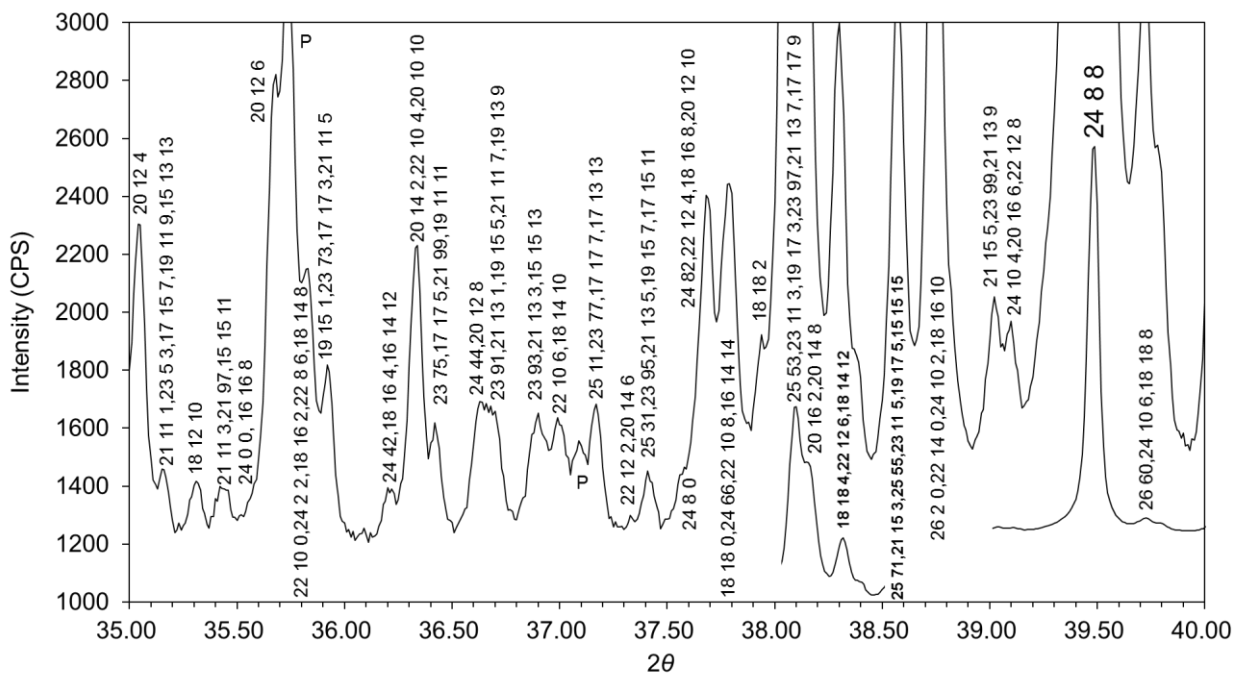
Appendix

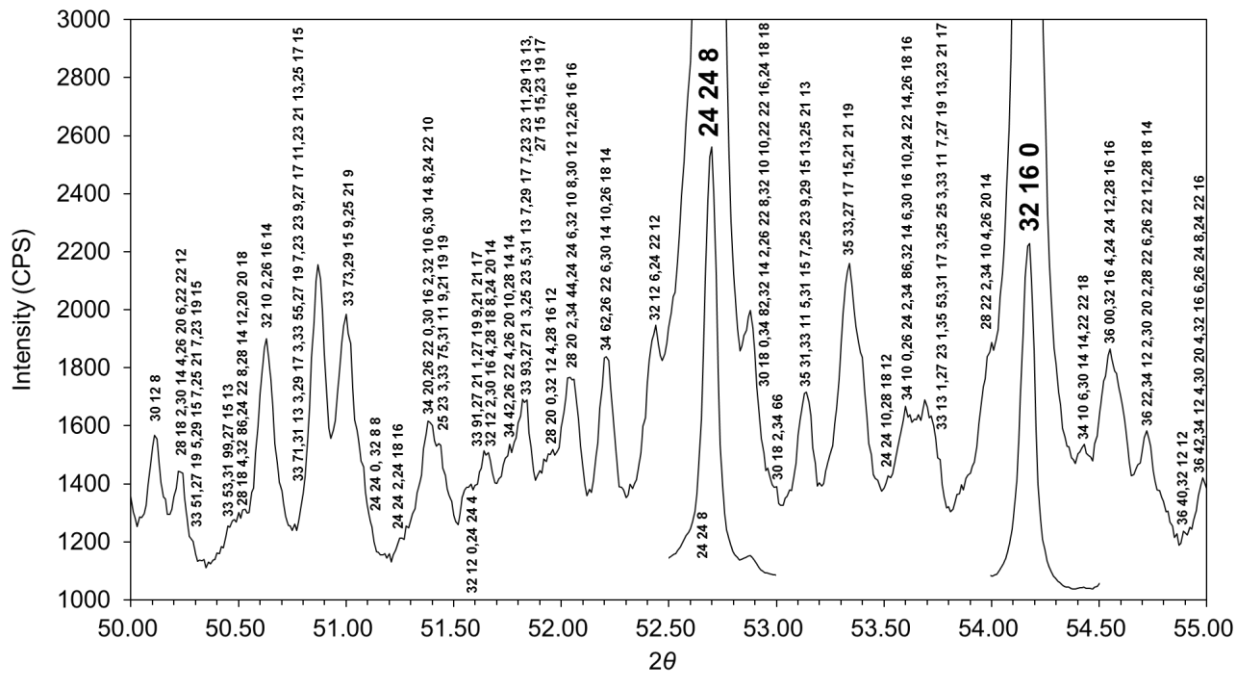
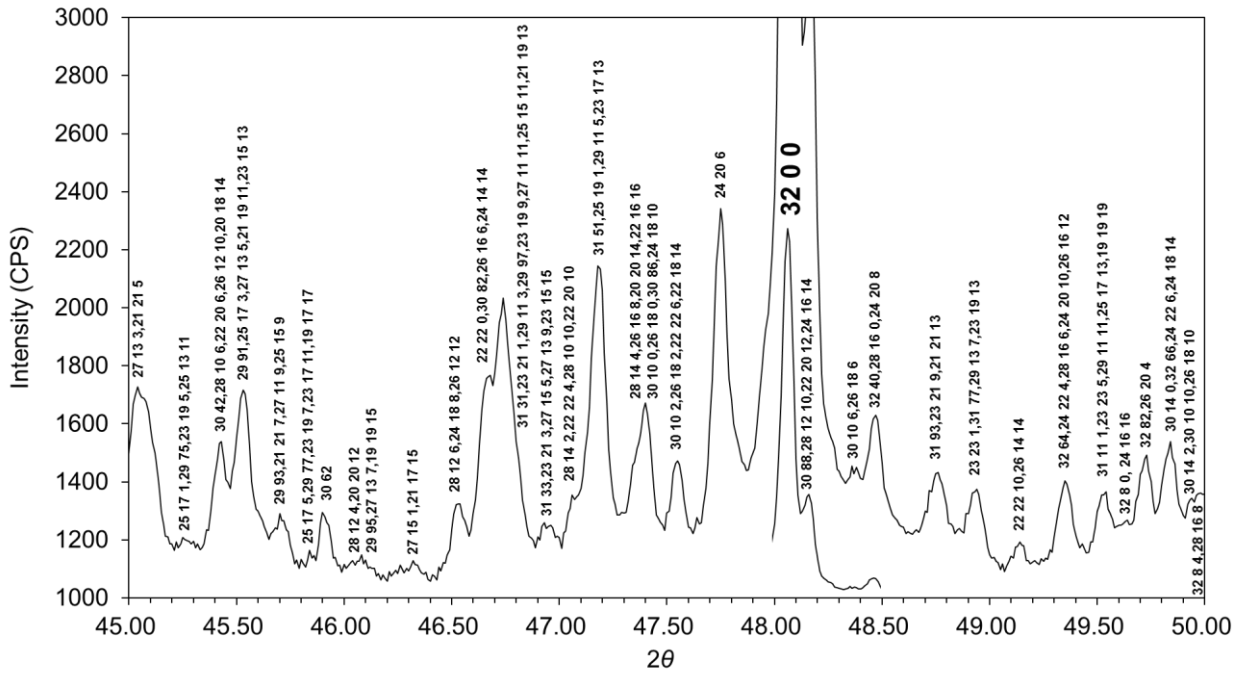
Appendix 1: Complete Synchrotron X-ray Diffraction Pattern of the M8 Murataite Polytype











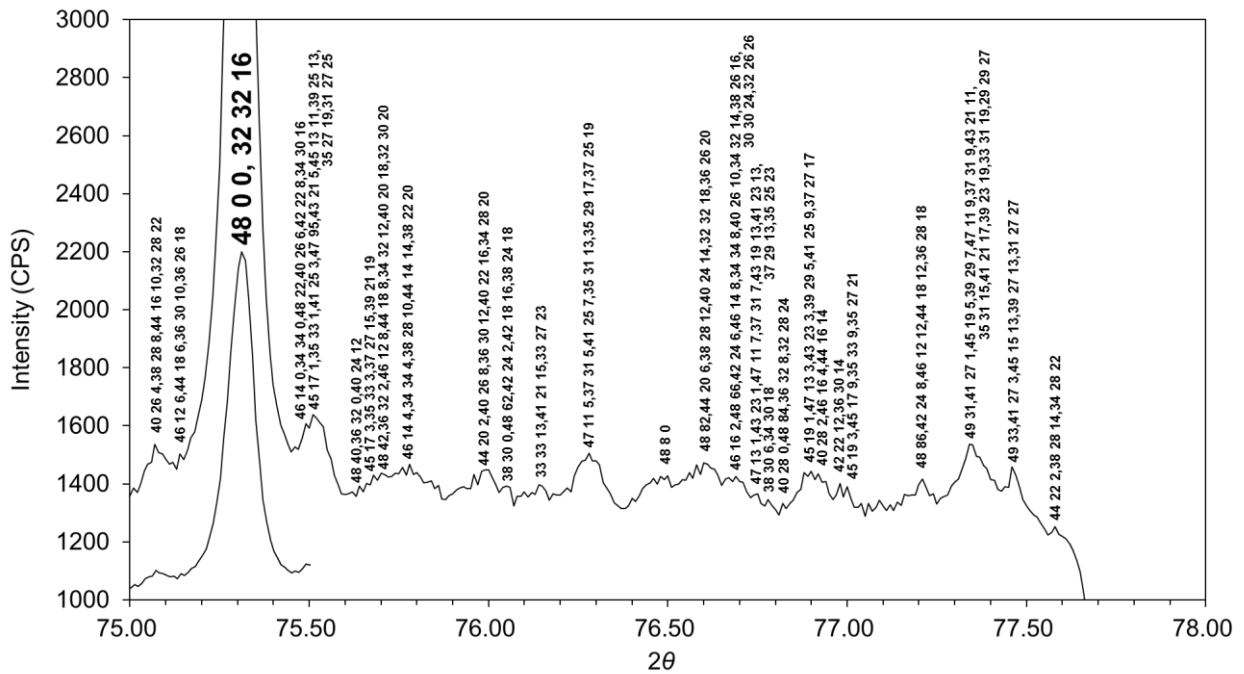
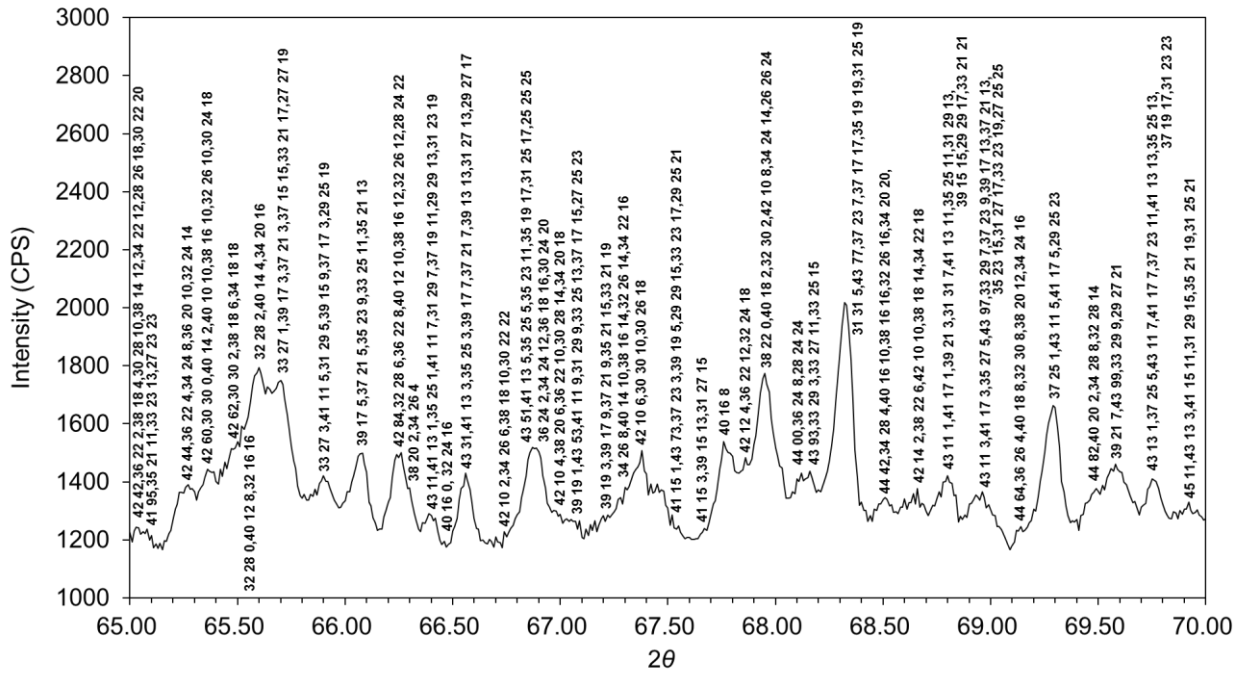


Fig. A1-1 Complete synchrotron X-ray diffraction pattern of the very weak peaks from M8-type murataite at $2\theta = 2-78^\circ$ described in Chapter 2.

Achievements

List of publications

- [1] **R. Maki** and Y. Suzuki, "Microstructure and mechanical properties of MgO-doped Al₂TiO₅ prepared by reactive sintering," *J. Ceram. Soc. Jpn.*, **121** [7] 568-571 (2013).
- [2] **R. S. S. Maki** and Y. Suzuki, "Mechanical strength and electrical conductivity of reactively-sintered pseudobrookite-type Al₂TiO₅-MgTi₂O₅ solid solutions," *J. Ceram. Soc. Jpn.*, **124** [1] 1-6 (2016).
- [3] **R. S. S. Maki**, P. E. D. Morgan, and Y. Suzuki, "X-ray powder diffraction characterization of the large volume unit-cell of the M8 murataite polytype," *Powder Diffr.*, **31** [1] 8-15 (2016). (Fig. A1)
- [4] **R. S. S. Maki**, K. Kobayashi, and Y. Suzuki, "Electrical properties of murataite modules with complex and large-volume fluorite-type superstructures," *Mater. Res. Bull.*, **84** 254-258 (2016).
- [5] **R. S. S. Maki**, P. E. D. Morgan, and Y. Suzuki, "Synthesis and characterization of a simpler Mn-free, Fe-rich M3-type murataite," *J Alloy. Compd.*, **698** [25] 99-102 (2017).
- [6] **R. S. S. Maki** and P. E. D. Morgan, "Synchrotron X-ray diffraction pattern of the M8 murataite polytype," *Powder Diffr.*, (Minor revision).

List of reference publications

- [1] H. Nishijima, **R. Maki**, and Y. Suzuki, "Microstructural control of porous Al₂TiO₅ by using potato starch as pore-forming agent," *J. Ceram. Soc. Jpn.*, **121** [8] 730-733 (2013).
- [2] C. Nethravathi, C. R. Rajamathi, M. Rajamathi, **R. Maki**, T. Mori, D. Golberg, and Y. Bando, "Synthesis and thermoelectric behavior of copper telluride nanosheets," *J. Mater. Chem. A*, [2] 985-990 (2014).
- [3] C. Delacotte, S. Hebert, V. Hardy, Y. Breard, **R. Maki**, T. Mori, and D. Pelloquin, "Impact of densification on microstructure and transport properties of CaFe₅O₇," *Solid State Sciences*, **54** 54-58 (2016).
- [4] H.-W. Son, **R. S. S. Maki**, B.-N. Kim, and Y. Suzuki, "High-strength pseudobrookite-type MgTi₂O₅ by spark plasma sintering," *J. Ceram. Soc. Jpn.*, **124** [8] 838-840 (2016).
- [5] **R. S. S. Maki**, S. Mitani, and T. Mori, "Effect of spark plasma sintering (SPS) on the thermoelectric properties of magnesium ferrite," *Mater. Renew. Sust. Energ.*, (2017). DOI: 10.1007/s40243-016-0086-9
- [6] H. Nishijima, T. Kawashima, **R. S. S. Maki**, and Y. Suzuki, "Microstructure and piezoelectric properties of (Bi_{0.5}Na_{0.5})_{1-x}Ba_xTi_{1-x}(Fe_{0.5}Nb_{0.5})_xO₃ ceramics," *Arab. J. Chem.* (in press).

Proceedings

- [1] T. Kawashima, **R. S. S. Maki**, and Y. Suzuki, "Preparation and microstructure of electrospun BaTiO₃ fibers," *Int. Lett. Chem. Phys. Astro.*, **62** 5-9 (2015). (The 3rd Tsukuba International Conference on Materials Science (TICMS2015))

Prizes

- [1] **R. Maki**, M. Haruta, H. Kurata, and Y. Suzuki, IWP2014 PRIZE, "Synthesis and microstructure of murataite ceramics obtained by reactive sintering," IWP2014 (International Workshop on Science and Patents), Tsukuba, Japan, (Sep., 2014).

- [2] **R. Maki**, T. Kiyomura, M. Haruta, H. Kurata, P. E. D. Morgan, and Y. Suzuki, 2015 Ceramographic Exhibit & Competition Transmission and/or Scanning Transmission Electron Microscopy 1st Place, "Starlit sky over giant unit-cell pyramids," The American Ceramic Society, OH, USA, (Oct., 2015). (Fig. A2)
- [3] **R. S. S. Maki**, P. E. D. Morgan, and Y. Suzuki, The Ceramic Society of Japan The 28th Fall Meeting Best Poster Award, "Synthesis and microstructural characterizations of murataite superstructure for new solid oxide electrolyte," The Ceramic Society of Japan, Toyama, Japan, (Sep., 2015).
(牧 涼介, Peter E. D. Morgan, 鈴木義和, 日本セラミックス協会 2015 年秋季シンポジウム 最優秀ポスター賞, "新規電解質に向けたムラタイト超格子構造の創製と微構造評価," No. 1PL02, 日本セラミックス協会, 富山, 日本, 2015 年 9 月.)
- [4] **R. S. S. Maki**, K. Kobayashi, and Y. Suzuki, The Ceramic Society of Japan Annual Meeting 2016 Distinguished Poster Award, "Synthesis and characterizations of very complex and enormous-volume fluorite-type superstructures," The Ceramic Society of Japan, Tokyo, Japan, (Mar., 2016).
(牧 涼介, 小林清, 鈴木義和, 日本セラミックス協会 2016 年年会 優秀ポスター発表賞, "巨大な単位格子を有する蛍石型超格子構造の創製と特性評価," No. 1P182, 日本セラミックス協会, 東京, 日本, 2016 年 3 月.)

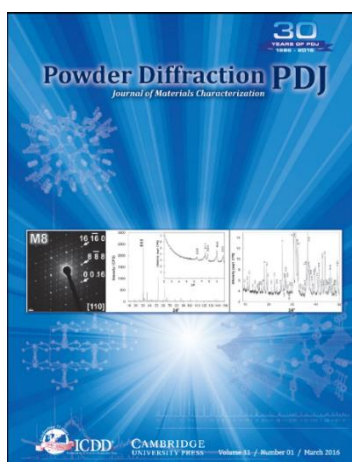


Fig. A1 Technical report selected as the cover page of Powder Diffraction journal Vol. 31 No. 1.

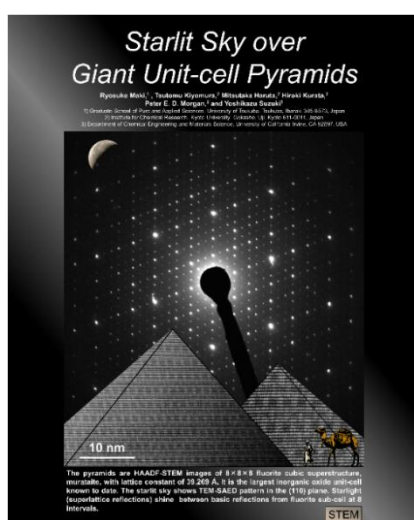


Fig. A2 2015 Ceramographic Exhibit & Competition Transmission and/or Scanning Transmission Electron Microscopy 1st Place "Starlit Sky over Giant Unit-cell Pyramids". This poster was selected as the back cover of the Journal of the American Ceramic Society (JACerS) Vol. 99 No. 2.

Achievements

Research Funds

- [1] **R. Maki** and Y. Suzuki, Sasakawa Scientific Research Grant, The Japan Science Society, No. 26-338, (Apr., 2014–Feb., 2015).
(牧 涼介, 鈴木義和, 財団法人日本科学協会平成 26 年度笹川科学研究助成, “擬ブルッカイト型構造を有するセラミックス材料の微構造制御と高機能化,” 研究番号 26-338, 財団法人日本科学協会, 2014 年 4 月～2015 年 2 月.)
- [2] **R. Maki** and Y. Nakagoshi, Budding Researchers Support Program, “Crystal structural analysis of Al-Ca-Ti-Mn-Fe-Zr oxide with 8×8×8 fluorite-type structure,” Proposal No. 2016A1782, Japan Synchrotron Radiation Research Institute (JASRI), (7-8, Jul., 2016).
(牧 涼介, 中越悠太, 大型放射光施設 SPring-8 大学院生提案型課題 (産業利用分野) [旧名: 萌芽], “8×8×8 蛍石型超格子構造を有する Al-Ca-Ti-Mn-Fe-Zr-O 系酸化物の結晶構造解析,” 課題番号: 2016A1782, 公益財団法人高輝度光科学研究センター(JASRI), 2016 年 7 月 8 日～2016 年 7 月 9 日.)

Support Programs

- [1] **R. Maki**, “Nano Technology Platform Japan” program, Ministry of Education, Culture, Sports, Science and Technology (MEXT), Institute for Chemical Research, Kyoto University, Japan, (6-8, Aug., 2014).
(牧 涼介, 文部科学省ナノテクノロジープラットフォーム平成 26 年度学生研修プログラム, “分析電子顕微鏡による構造解析と化学分析,” 文部科学省, 京都大学 化学研究所, 日本, 2014 年 8 月 6 日～2014 年 8 月 8 日.)
- [2] **R. Maki**, National Nanotechnology Coordinated Infrastructure (NNCI) International Research Experience for Graduates / iREG_NNCI and NIMS in “Nano Technology Platform Japan” program, “Gas microfluidics using MEMS micro-pumps,” Ministry of Education, Culture, Sports, Science and Technology (MEXT) in Japan as part of the cooperation with National Science Foundation (NSF), University of Louisville, Louisville, KY, USA, (1 Jun.- 3 Aug., 2016).
(牧 涼介, 文部科学省ナノテクノロジープラットフォーム平成 28 年度米国 NNCI 施設利用研修プログラム, “Gas Microfluidics using MEMS Micro-pumps,” 文部科学省, University of Louisville, Louisville, Kentucky, USA, 2016 年 6 月 1 日～2016 年 8 月 3 日.)
Symposium participated during the program: **R. Maki**, K. Haught, P. Shuvra, S. McNamara, "Gas microfluidics using MEMS micro-pumps," CUR REU Symposium , KY, USA (Aug. 2016).
Report written during the program: **R. S. S. Maki**, P. Shuvra, S. McNamara, “Nanoscale channels for Knudsen gas pumps,”
- [3] **R. S. S. Maki**, University of Tsukuba Study Abroad Support Programs Travel Support for Overseas Dispatch of Graduate Students, “Materials Science & Technology 2016 (MS&T16),” University of Tsukuba, Salt Place Convention Center, Salt Lake City, UT, USA, (23-28, Oct., 2016).
(牧 涼介, 筑波大学海外留学支援事業 (はばたけ! 筑大生) 平成 28 年度海外学会等参加支援プログラム, “Materials Science & Technology 2016 (MS&T16),” 筑波大学, Salt Place Convention Center, Salt Lake City, UT, USA, 2016 年 10 月 23 日～2016 年 10 月 28 日.)

Conferences/Symposiums/Workshops

International

- [1] **R. Maki**, T. Kozawa, and Y. Suzuki, "Synthesis and electrical properties of pseudobrookite-type ceramics," Junior Euromat 2012 the Federation of European Material Societies, No. F133, Lausanne, Switzerland (July, 2012).
- [2] **R. Maki**, T. Kozawa, and Y. Suzuki, "Reactive sintering and evaluation of MgO-doped Al_2TiO_5 ," IWP2012 (International Workshop on Science and Patents), Tsukuba, Japan (Oct., 2012).
- [3] **R. Maki**, Y. Suzuki, "Reactive sintering and evaluation of MgO-doped Al_2TiO_5 ," 1st International Workshop on Nano and Microstructure Design (IWNMD2012), Tsukuba, Japan (Dec., 2012).
- [4] **R. Maki**, Y. Suzuki, "Effect of MgO-doping on microstructure and properties of Al_2TiO_5 ," Euromat2013 European Congress and Exhibition on Advanced Materials and Processes, Seville, Spain (Sep., 2013).
- [5] **R. Maki**, Y. Suzuki, "Synthesis and microstructure of murataite ceramics obtained by reactive sintering," IWP2014 (International Workshop on Science and Patents), Tsukuba, Japan (Sep., 2014).
- [6] **R. Maki**, Y. Suzuki "Synthesis and evaluation of pseudobrookite-type Al_2TiO_5 - MgTi_2O_5 solid solutions with low thermal expansion," Pittsburgh, USA (Oct., 2014).
- [7] **R. S. S. Maki**, Y. Suzuki, "Synthesis and microstructural characterizations for murataite ceramics with fluorite superstructure," IWP2015 (International Workshop on Science and Patents), Tsukuba, Japan (Sep., 2015).
- [8] **R. S. S. Maki**, P. E. D. Morgan, and Y. Suzuki " X-ray powder diffraction characterization of the giant unit cell of the M8 murataite polytype: $8\times 8\times 8$ fluorite-type superstructure," Materials Science & Technology 2016, Salt Lake City, USA (Oct., 2016).

Domestic

- [1] **R. Maki**, T. Kozawa, and Y. Suzuki, "Synthesis and electrical properties of pseudobrookite-type ceramics," The Ceramic Society of Japan The 25th Fall Meeting, Nagoya, Japan (Sep., 2012).
- [2] **R. Maki** and Y. Suzuki, "Reactive sintering and evaluation of MgO-doped Al_2TiO_5 ," The Ceramic Society of Japan 2013 Annual Meeting, Tokyo, Japan (Mar., 2013).
- [3] **R. Maki** and Y. Suzuki, "Electrical properties of low thermal expansion ceramics in the system Al_2O_3 - TiO_2 - MgO ," The Ceramic Society of Japan The 26th Fall Meeting, Nagano, Japan (Sep., 2013).
- [4] **R. Maki** and Y. Suzuki, "Microstructural control and electrical properties of low thermal expansion ceramics in the system Al_2O_3 - TiO_2 - MgO ," The 33rd electronics division meeting of the Ceramic Society of Japan, Ibaraki, Japan (Oct., 2013).
- [5] **R. Maki** and Y. Suzuki, "Reactive sintering and evaluation of $\text{Al}_{2(1-x)}\text{Mg}_x\text{Ti}_{(1+x)}\text{O}_5$ ceramics with low thermal expansion," The Ceramic Society of Japan 2014 Annual Meeting, Tokyo, Japan (Mar., 2014).
- [6] **R. Maki** and Y. Suzuki, "Reactive sintering and evaluation of Al_2TiO_5 - MgTi_2O_5 solid solutions with low thermal expansion," Japan Society of Powder and Powder Metallurgy Spring Meeting 2014, Tokyo, Japan (Jun., 2014).
- [7] **R. Maki** and Y. Suzuki, "螢石型超格子構造を有するムラタイトセラミックスの作製と評価," SAT

Achievements

Technology Showcase 2015, Ibaraki, Japan (Jan., 2015).

- [8] **R. Maki**, P. E. D. Morgan, and Y. Suzuki, “Synthesis and electrical properties of murataite ceramics with fluorite-type superstructure,” The Ceramic Society of Japan The 28th Fall Meeting, Toyama, Japan (Sep., 2015).
- [9] **R. Maki**, P. E. D. Morgan, and Y. Suzuki, “Synthesis and microstructural characterizations of murataite superstructure for new solid oxide electrolyte,” The Ceramic Society of Japan The 28th Fall Meeting, Toyama, Japan (Sep., 2015).
- [10] **R. S. S. Maki**, K. Kobayashi, and Y. Suzuki, “Synthesis and characterizations of very complex and enormous-volume fluorite-type superstructures,” The Ceramic Society of Japan 2016 Annual Meeting, Tokyo, Japan (Mar., 2016).

Acknowledgements

The author would like to express my deepest appreciation and gratitude to my supervisor Associate Professor Yoshikazu Suzuki in the Development of Materials Science at the Graduate School of Pure and Applied Sciences, University of Tsukuba for his great help, unlimited patience and excellent guidance in coordinating this investigation. The author would like to thank Professors Kazuo Kadowaki and Tokushi Kizuka at the Graduate School of Pure and Applied Sciences and Principal Researcher Dr. Kiyoshi Kobayashi at Ceramics Processing Group, National Institute for Materials Science for reviewing this thesis and their helpful advices.

The author is particularly grateful for in-depth discussion, helpful suggestion, grateful programming work and insightful comments provided by Dr. Peter E. D. Morgan at Department of Chemical Engineering and Materials Science, University of California Irvine, which lead to so favorably and excellent findings throughout this investigation. The author sincerely thanks to Group Leader Tohru S. Suzuki at Ceramics Processing Group, National Institute for Materials Science for the use of SEM-EDS. The author deeply appreciates again Principal Researcher Dr. Kiyoshi Kobayashi for evaluation of electrical properties and his helpful suggestion and kind guidance. The author very much appreciates to Professor Hiroki Kurata, Assistant Professor Mitsutaka Haruta and Specific Researcher Tsutomu Kiyomura at Institute for Chemical Research, Kyoto University for their kind help on TEM/STEM analysis as a part of Nano Technology Platform Japan program.

Acknowledgement is given to Dr. Keiichi Osaka for his help on the synchrotron radiation experiments performed at the BL19B2 of SPring-8 with the approval of the Japan Synchrotron Radiation Research Institute (JASRI) (Proposal No. 2016A1782). The author also thanks to Associate professor Takahiro Kondo at Faculty of Pure and Applied Sciences for his help on the XPS analysis.

The author gratefully acknowledges author's colleagues of Yoshikazu Suzuki Laboratory for their time, friendship and awesome helps.

Lastly, the author dedicates genuine dissertation to my parents, Shigeru Maki and Yukiko Maki, my older brother, Shota Maki, and my grandparents, Shoichi Maki, Harumi Maki, Sadao Arai and Takiko Arai for their hearty supports, encouragements, understandings and caring throughout my life in the period of doctoral course.

Ryosuke Maki

February, 2017
Tsukuba, Japan